UNIVERSITY OF SOUTHAMPTON

Faculty of Physical Science and Engineering
Department of Electronics and Computer Science

Molecular Dynamics in Core-Shell Filled Epoxy Nanocomposites

by

Sunny Chaudhary

MSc

ORCiD: 0000-0003-2664-7083

A thesis for the degree of
Doctor of Philosophy

23 January 2023

University of Southampton

Abstract

Faculty of Physical Science and Engineering
Department of Electronics and Computer Science

Doctor of Philosophy

Molecular Dynamics in Core-Shell Filled Epoxy Nanocomposites

by Sunny Chaudhary

In this study, core-shell and hollow nanoparticle architecture types were synthesis and were utilised as epoxy fillers with the main objective of understanding the molecular dynamics of these nanocomposite. Secondly to understand the effect of different characteristics of these nanoparticles such as the structure, crystallinity, core and shell particle nature on the dielectric properties of the bulk system by comparing them with commercially obtained conventional core-type nanoparticles and amongst themselves. The first step of the study was to select suitable combinations of core and shell and establish a reproducible method for the synthesis of the core-shell and hollow nanoparticle. For this, initially, to understand the effect of the shell crystallinity, commercially available silica (SiO_2), silica-silica (SiO_2-SiO_2) and hollow-silica (h-SiO_2) were selected. Commercially obtained SiO_2 was calcined at 800 °C and crystalline. Alternatively, both SiO_2-SiO_2 and h-SiO_2 were vacuum dried at 60 °C and the resulting shell was amorphous. For the synthesis of SiO_2-SiO_2, commercially obtained SiO_2 was used as the core where as for synthesis of h-SiO_2, poly (acrylic acid-sodium salt) (PAA-Na) was used as template and the shell was deposited via sol-gel method; subsequently, the PAA-Na template was removed to obtain hollow architecture via heat treatment. These nano-powders were characterised by transmission electron microscopy (TEM), Fourier transform infra-red spectroscopy (FTIR), differential scanning calorimetry (DSC) and broadband dielectric spectroscopy (BDS). TEM graphs showed successful synthesis of the nanoparticle where a shell formation was observed in case of SiO_2-SiO_2 nanoparticles and hollow centre in case of h-SiO_2. FTIR measurement revealed a characteristic Si - O - Si absorbance band along with a overlapping absorbance band at higher wavelengths which were attributed to ν_{as}-transverse optic (TO) of crystalline and ν_{as}-longitudinally optic (LO) of amorphous structures in the nanoparticles. ν_{as}-LO absorbance intensity was the least in SiO_2 followed by SiO_2-SiO_2 and h-SiO_2 implying the increase in structural disorder following the same trend.

Afterwards, epoxy nanocomposite were prepared whilst maintaining the stiochiometric ratio between the resin and hardener. To obtain optimal dispersion the nanocomposites were prepared by there different methods, namely, bath sonication, probe sonication and solvent mixing. TEM graphs were obtained to evaluate the dispersion and solvent mixing which demonstrated better dispersion was selected to prepare the nanocomposites. Since we are interested in the surface characteristics it is important to maintain comparability across all samples. Therefore, the fillers were loaded based on their total surface area; three different surface areas were selected. No significant changes in the unreacted epoxide groups were observed. Secondly, with increased disorder of the shell an increasing concentration of hydroxyl groups originating from the surface silanols was observed. DSC measurements showed no significant changes in the glass transition temperature (T_g). Correspondingly, from BDS measurements no significant changes in the alpha (α) and gamma (γ) relaxation were observed. Alongside beta (β) relaxation an additional relaxation was observed in SiO_2-SiO_2 and h-SiO_2 nanocomposite, termed omega (ω) relaxation. The behaviour of β and ω relaxation were similar which implied involvement of similar chemical groups i.e. hydroxyl (-OH). As the concentration of surface silanols increased the ω relaxation became more pro-eminent. SiO_2-SiO_2 nanocomposite has an overlapping β and ω relaxation where it is segregated towards higher frequencies in h-SiO_2 nanocomposite. The activation energy of the β and ω was similar. Thus, the ω relaxation was attributed to the hydrogen bond interaction between the hydroxy ether group of the polymer main chain and the surface silanol groups. Additionally, towards lower frequencies interfacial polarization phenomena was observed. SiO_2 and h-SiO_2 had a single interfacial peak whereas SiO_2-SiO_2 had two interfaical peaks. The second peak was relatively weak and was hypothesised to be originating from the core-shell interface within the nanoparticle.

Furthermore, To confirm the hydrogen bond interactions, dynamic mechanical analysis (DMA) measurements were performed. For this, additionally, four more epoxy nanocomposites filled with Al_2O_3 - SiO_2, TiO_2 - SiO_2, Al_2O_3 and TiO_2 were prepared. Alumina-silica (Al_2O_3 - SiO_2) and titania-silica (TiO_2 - SiO_2) were selected due to the significant contrast between their relative permittivity and to study the effects of the core particle. Both were synthesised following the sol-gel method. Analysis of tan δ for α and β relaxation revealed the presence of hydrogen bonds in core-shell nanoparticles. The absorbance band of the symmetric and asymmetric vibration of the CH_2 and CH_3 group were also affected by the core-shell structures via OH - π interactions. OH - π primarily depended upon the structure of the surface of the nanoparticles. Finally, the hypothesis realted to core-shell interface was tested. BDS analysis of metal oxide nanocomposites at interfacial polarization frequencies via Havriliak - Negami (HN) and Cole - Cole formulation revealed two pro-eminent interfacial relaxations. Low frequency relaxation was attribute to the core-shell interface and higher frequency relaxation was attributed to the conventional particle-polymer interface. Additionally, to maintain consistency between α and β parameters at varying temperatures whilst performing HN analysis a MATLAB plugin software was developed.

Contents

List of Figures

List of Tables

Declaration of Authorship

I declare that this thesis and the work presented in it is my own and has been generated by me as the result of my own original research.

I confirm that:

1. This work was done wholly or mainly while in candidature for a research degree at this University;
2. Where any part of this thesis has previously been submitted for a degree or any other qualification at this University or any other institution, this has been clearly stated;
3. Where I have consulted the published work of others, this is always clearly attributed;
4. Where I have quoted from the work of others, the source is always given. With the exception of such quotations, this thesis is entirely my own work;
5. I have acknowledged all main sources of help;
6. Where the thesis is based on work done by myself jointly with others, I have made clear exactly what was done by others and what I have contributed myself;
7. None of this work has been published before submission

Signed:..... Date:.....

Acknowledgements

The research work was performed within the K-Project 'PolyTherm' at the Polymer Competence Centre Leoben GmbH (PCCL, Austria) within the framework of the COMET-program of the Federal Ministry for Transport, Innovation and Technology and the Federal Ministry for Digital and Economic Affairs with contributions by scientific partners and company partners. Funding is provided by the Austrian Government and the State Government of Styria (Österreichische Forschungsförderungsgesellschaft – Grant Number: 862835).

The author would like to express his gratitude to those who contributed to the successful completion of this PhD and specifically to:

- Dr. Thomas Andritsch for the substantial guidance, friendly chats, for always supporting me over the duration of this PhD and for the confidence he showed in me throughout my PhD study.
- Professor Alun S. Vaughan for his meaningful supervision and his support whenever it was needed.
- The Tony Davies High Voltage Laboratory in the University of Southampton, for giving me the chance to work in their facilities. Special thanks to: Neil Palmer, Alan Welford, Liz Tillotson and Charlie Reed.
- Members of the PolyTherm project Dr. Frank Wiesbrock and Dr. Philipp Marx for the enjoyable collaboration.
- Dr. Michael Feuchter from Montanuniversität Leoben for helping with the DMA measurements and analysis.
- Dr. Orestis Vryonis my closest colleague over the duration of this PhD who always supported me, for enjoyable collaborations and for spending some of his time with me when I really needed it.
- Dr. Istebreq Saeedi for the technical help they provided within the lab during the first few months of my experimental sessions.
- Dr. Simone Vincenzo Suraci for moments we spent together during the summer school, conferences and for interesting collaborations.
- My lab colleague Phichet Ketsamee for the help with XRD imaging and FTIR measurements.

- Members of the materials reading group Hyungjin Yoon and Ian Hosier for their feedback and interesting discussions.
- My closest friend Ms. Firoza Patel for the huge support over the years.
- My parents.

To My Parents...

Definitions and Abbreviations

BDS - Broadband Dielectric Structure
DMA - Dynamic Mechanical Analysis
TEM - Transmission Electron Microscopy
PAA -Na - Poly Acrylic Acid (sodium salt)
CTAB - Hexadecyltrimethylammonium bromide
TEOS - Tetraethyl Orthoilicate
DER - Diglycidyl Ether of Bis-phenol
DSC - Differential Scanning Calorimetry
FTIR - Fourier transform Infra-red.
AUC - Area under the curve
FWHM - full width half maxima
LOIC - Laboratory for Optical computational Instrumentation
AC - Alternating Current
rpm - Revolution per minute

$\Delta\varepsilon$ - Dielectric strength
T_g - Transition temperatures
g - Kirk-wood correction factor
Np - Number of dipoles
μ - Dipoles
K_b - Boltzmann constant
V - Volume
T - Temperature
N_A- Avogadro number
e - Elementary charge
ϵ_r - Dielectric constant
ϵ_o - Permitivity of free space
I - Ionic strength
z - Charge on ion
d - Diameter of nanoparticle (unless specified)
a - Length of cell
ϵ_{op} - Optical permittivity
ϵ_s - Static permittivity
ψ(r)- Potential as a function of r

ρ_i - Charge density
Ea - Activiation energy
R - Universal gas constant
η - Viscosity
γ - Surface energy
g - Gram
mol - Mole
h - Hour
°C - Degree celcius
ml - Millilitre
mPa - MilliPascal
μm - Micrometer
mm - Millimeter
Hz- Hertz
V - Volts
N - Newton
cm - Centimeter
γ -Gamma
π - Pi
α - Alpha
β - Beta
ϵ - Epsilon
K - Kelvin
δ - Delta
ν - Crosslink density
Å- Angstrom
nm - Nanometer
ω - Omega
fmax - Frequency of peak maxima
νas - Asymmetric stretching
νas-TO - Asymmetric stretching in transversal optical
νas-LO - Asymmetric stretching in Longitudinal optic mode

Chapter 1

Introduction

1.1 Background

In medieval times, a special type of sword "Damascus Blades" gained mythical reputation around the world. These were extraordinarily strong yet flexible enough to bend from hilt to tip. These swords made from small cakes of steel from India called 'wootz'. The secret behind their exceptional characteristics was uncovered to be - carbon nanotubes. This is one of the earliest mentioned usage of nanoparticles to enhance the properties of the base material, although unknowingly. Two centuries later, the idea of "Nanometric dielectrics" was first introduced in 1994 (1) by T. J. Lewis, in which the consequences of reducing the phase size in a two-phase dielectric system was considered. Later in 2001, M. F. Fréchette (2) combined the terms "Nanotechnology" and "Dielectrics" to give the term "Nanodielectrics"; an emerging class of improved materials. However, it was not until experimental study performed by J. K. Nelson (3) and reported in "Overview of Nanodielectrics: Insulating Materials of the Future" the field gained the interest of researchers. The observation and data reported provided indication that the performance of nanodielectrics could exceed the limited capabilities of micron-scaled composites for every property whether thermal, mechanical or electrical.

According to the European Commission (4), by 2011, the definition of a nanomaterial is: "A natural, incidental or manufactured material containing particles, in an unbound state or as an aggregate or as an agglomerate and where, for 50% or more of the particles in the number size distribution state, one or more of the external dimensions is in the size range 1 to 100 nm." In 2010 (5), the term "Nanodielectric" was defined as: "A multicomponent dielectric possessing nanostructures, the presence of which leads to changes in one of several of its dielectric properties", in the International Conference on Solid Dielectrics. It refers to a composite material consisting of a polymeric matrix and a filler with at least one of its dimensions in the nanometric scale (<100 nm) or else, a polymer nanocomposite specifically used for high voltage applications.

Nowadays "nanodielectrics", is a popular term and has been extensively researched over the years (6). This subsequent research and experimentation on the use of nano-composites in electrical insulation has provided overwhelming indication of their position impact. For example, nanocomposites have been found to show lower permittivity and loss tangent when compared with equivalent microcomposites; thereby suggesting reduced interfacial polarization effects within nanocomposites (7). Although, the mechanism behind these phenomena have been explained and studied extensively a generalised understanding is still lacking. Phenomena like agglomeration, effect of water absorption, understanding of the molecular dynamics and interfacial effects are some of the challenges in the field which need further investigation. Understanding these parameters will provide profound control over the fabrication of polymer nanocomposites with desired and tailored characteristics.

1.1.1 Core-shell nanoparticles

Researchers have found that heterogeneous, composite or sandwich semiconductors particles show better efficiency then then just corresponding single particle. These particles can potentially even develop new properties. In the 1990's researchers synthesised concentric multilayer semiconductor nanoparticles in view to enhance their properties (8; 9; 10). Nanoparticles which develop a concentric multilayer of semiconductor nanoparticles of different nature are called Core/Shell nanoparticles. Core/Shell nanoparticles are attracting immense attention due to their application in variety of different field like electronics, biomedical, optics and catalysis. There are highly functional materials with modified properties (11). These properties can be changed by changing their core material or the ratio between the core and the shell. The properties such as reactivity decrease, thermal stability and dispersibility of the core can be enhanced with the help of the shell. Fig. 1.1 illustrates different possible structures for core-shell nanoparticles.

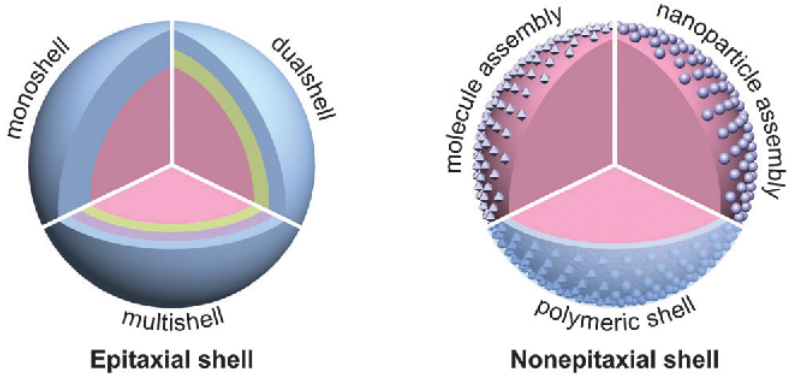

FIGURE 1.1: Schematic illustration of some different architecture types of core-shell nanoparticles (12).

1.2 Research motivation

Numerous models have been suggested to describe the main characteristics of the interfacial interactions, interphase formation, such as the intensity, the double layer, the interphase volume, and the multicore model. However, they only access specific properties. No single model explains all the attributes of nanocomposite systems. Also unlike the interfacial region, interphase has been comparatively given less importance and been sparsely investigated. In the limited research done on the interphase it mostly focuses on the polymer interphase which lies outside the nanoparticle. This research sets out to investigate the role of the particle characteristics such its architecture, surface structure and crystallinity in determining the properties of the particle-polymer interphase and on the dielectric properties of nanocomposite by means of different combinations of core-shell and hollow nanoparticles. The hypothesis in (13) is, that the interaction zone between the particle and the host can be treated as two separate zone i.e. the particle interphase and the polymer interphase. According to Lewis, the interaction zone has properties different than any of the bulk phase i.e. particle or polymer (1). The change in properties is claimed to be instantaneous rather than gradual whilst moving from particle interface to the polymer interface. The exact location of this change is unknown. However, it is claimed to be present with in the interaction zone between the two bulk phases. This interaction zone is referred to as the polymer interphase. Tanaka's multi-core model assumes the presence of an electric double layer where the nanoparticles itself can be negatively or positively charge which gives rise to a diffuse layer in the polymer interphase. The location of these charges is in a region closer to the nanoparticle which is considered the particle interphase. By changing the characteristic or structure of the particle surface in a controlled manner, it is plausible to quantify the effects and gain understanding of the physical or chemical reasons for the observed behaviour and try to correlate the two.

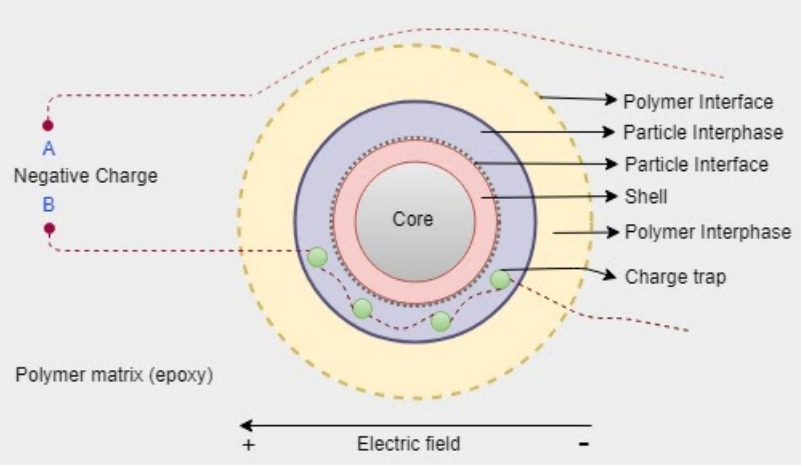

FIGURE 1.2: Possible ways of particle interface interaction with the charge movement.
A: Dielectric - energy barrier constraining charge movement.
B: Conductive - facilitating charge movement (13)

Furthermore, molecular dynamics of a polymeric system are very complex. The origin of various relaxation and changes observed due to addition of nanoparticles has been widely studied (14). However, the explanations along with the supporting data are controversial and various from author to author for the same observed phenomena. This gap has been highlighted and discussed extensively in the literature review. Further, the effect of core-shell nanoparticles on the bulk system have been studied in terms of mechanical, thermal and electrical properties (15). However, in most studies they have been treated as conventional nanoparticles, considering only the polymer-shell interphase. These particles introduce an additional interphase between the core and shell the effect of which on the molecular dynamics of the system or on the surface characteristics of the nanoparticle has not been studied and focused upon. Little research has been done on the effects of the core nanoparticle on the bulk properties. In comparison to their mechanical, thermal and optical properties the electrical properties of core-shell nanocomposites has not been extensively studied. Core-shell nanoparticles also offer the control over various parameters such as the polymer-shell interphase and surface characteristics of the nanoparticles. These parameters can be studied step by step whilst maintaining comparability across different nanocomposites to potentially isolate and study the origin of the effects on the bulk by varying a singular parameter. This will help gain better understanding of the molecular dynamics and different relaxation mechanisms to help develop nanocomposites with tailored properties.

1.3 Research aims and objective

The main aim of this PhD project was to study the molecular dynamics of epoxy nanocomposites filled with differently architecture nanoparticles i.e. core-shell and hollow core. More specifically to:

- Understand the effect of crystallinity and corresponding surface structure of the shell on the conventionally know relaxations
- Investigate the role of the core nanoparticle in determining the dielectric properties of the nanocomposite.
- Discern the impact of the core-shell interface on the particle-polymer interactions.
- Study any non-conventional relaxation behaviour and discern its origin.

This was sought to be accomplished with the usage of nanometric particles that are specifically selected to introduce controlled variations. For example, increasingly disordered surface structure of the nanoparticle.

1.4 Research questions and novelty

Upon discussion in the literature it will become apparent that most studies treat differently architectured nanoparticles as conventional core only type nanoparticles and unless surface modified majority of the discussion is based on the shape, size, relative permittivity and concentration of the nanoparticles. The effect of the additional internal interface is rarely addressed. Further, the extent of the effect of the particle on the interphasial properties in not yet fully understood. Furthermore, molecular dynamic in nanocomposites are complex and there exist multiple explanation for an observed behaviour where some even present contrary views.

Therefore, following set of question will be investigated:

1. Does the structure (tetrahedral or octahedral) or degree of disorder in the structure of nanoparticle surface affect the relaxation behaviour?
2. How does the absence of a core particle affect the dielectric behaviour of particle-polymer interphase?
3. What are the characteristics and origins of the interactions between the polymer and nanoparticles?
4. Which out of core or the shell have dominant effect on the dielectric properties on the nanocomposite?
5. Could the interphase within the nanoparticle have significant contribution towards particle-polymer interphase?

As such, Chapter 4 will be dedicated to give answers to questions 1 and 2 where as Chapter 5 will address questions 3 and 4. Where as both Chapter 4 and 5 will from both address question number 5.

1.5 Report structure

An introduction regarding epoxy nanocomposites and core-shell nanoparticles is presented in Chapter 1. Followed by the general purpose and main research objectives of this study. Furthermore, questions related to the gap in the literature were raised, which will establish the guidelines for the following experimental Chapters.

Chapter 2 is divided into seven section. The first and second section (2.1 and 2.2) introduces the epoxy resin, their chemical structure and the curing process when cured in presence of an amine hardener. Section 2.3 highlights the electrical and thermal properties of the epoxy nanocomposites, comments on the explanations of the mechanisms for the observed

electrical and thermal behaviour. Finally, shows the contradictions that exist in literature realted a common observation but has varying explanations. Section 2.4 highlights the characteristics of conventionally known molecular dynamics in epoxy nanocomposites whilst critically analysis them. 2.5 and 2.6 highlights the role of interfaces in nanocomposites and different generally accepted models developed to explain the different observations, respectively. Finally, section 2.7 presents the various categories of core-shell nanoparticles, synthesis routes, the advantages and disadvantages of these routes based on which the method used in the current study was selected.

Chapter 3 presents the materials utilised, the sample preparation method, nanoparticle synthesis method and the method to determine the size of the nanoparticles.

The results of material characterization are presented in Chapters 4 and 5. Where the main topic of Chapter 4 is accessing the role of the shell in determining the properties of the particle-polymer interphase. Simultaneously, also determine the effect of shell surface disorder and crystallinity on the particle-polymer interaction and consequently its effect on the bulk dielectric properties. Chapter 5 comments initially presents the DMA analysis which is used to further confirm the observation in Chapter 4. Secondly, highlights the importance of the core particle, its impact on the interfacial polarization and comments on the potential type of interactions occurring in the interphase.

Chapter 2

Literature Review

2.1 Epoxy Resin and Epoxies

Epoxies were discovered in the 1930's by two scientists, Dr Pierrer Castan and Dr Sylvan Greenlee. They were initially used for dental fixtures. Now after nine decades more than 50 different substances known as epoxy resin are available. Epoxy also known as polyepoxides are a class of reactive prepolymers and polymers which contain epoxide groups. When epoxy resin is processed with other chemical to produce epoxy plastics they are more commonly known as epoxies. They generally produced with the help of epichlorohydrin and Bisphenol A.

Epoxy resin may react (cross-link) with themselves by catalytic homopolymerisation or with another chemical called 'hardener' or 'curatives'. Most commonly used hardeners are polyamines, amino amides, or phenolic compounds. The reaction they undergo to react and produce epoxies is called curing process which creates a thermoset polymer with strong mechanical properties. Cured epoxy resins can have varying molecular chain lengths depending upon their molecular weight which further determines their possible use. Their extensive application is found in construction sector due to their hardness, stability and durability, sued for flooring, coating, piping etc. They are also used in automotive and aerospace industries to avoid corrosion. Further, they have good insulating properties which makes them good insulator to be used in common electronics (16). Epoxy has been used as an insulator for many decades, highly researched in the 1970's (17). Their low cost and low weight with high adaptability, good mechanical properties and resistance to chemicals make them very suitable candidate for insulation (18). Then the concept of "nanodielectrics" was first introduced by Lewis in 1994 (1). Over the last decade, research on epoxy based nanocomposite has gained more interest. Many investigations have been reported with improved mechanical properties and electrical properties (19; 20; 21; 22).

Use of nanofiller in epoxy to produce epoxy nanocomposite have shown enhanced dielectric properties. In an investigating by Singha (19) using different loading ratio of TiO2 and ZnO,

it was reported that the permittivity of epoxy nanocomposite at lower loading ratios of 0.1% reduced and showed advantageous behaviour. Permittivity was compared with micro size fillers as well where nanofiller showed comparatively better performance and lower tan δ values. In another investigation by Iyer (23) polymer nanocomposites with micro, nano and micro plus nano fillers were evaluated. The dielectric response showed lower permittivity then the unfilled epoxy system. However, not only the presence of nanofiller entirely effect the performance of the system. Good mixing methods as studied by Reading (24) along the effect of water in the nanocomposite (25), amount of silane coupling agent investigated in (26) and degree of agglomeration at high loading ratio (27) also have significant contribution towards the degradation or enhancement of the nanocomposite system.

2.2 The Curing Process

Fig. 2.1 illustrates the chemical structure of bisphenol A diglycidyl ether (DGEBA). It is an organic compound which is colourless and highly viscous. The chemical structure of DGEBA consists of two terminal epoxide groups. These epoxide groups play the most important role in the curing reaction. They react with the amine group of a hardener molecule for the crosslinking reaction. Jeffamine D230, an amine hardener, is a curing agent which reacts with carboxylic acids, isocyanates and forms slat readily with surfactants. It has a low viscosity and is colourless to pale yellow liquid. Fig. 2.2 represents the chemical structure of the amine hardener where the value of x typically is 2.5.

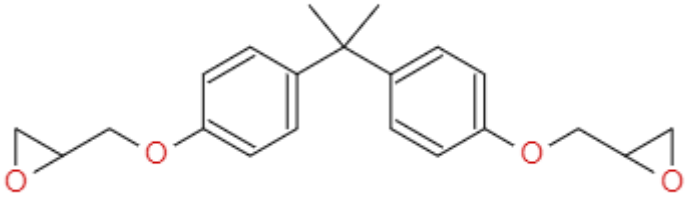

FIGURE 2.1: Chemical structure of DGEBA epoxy resin.

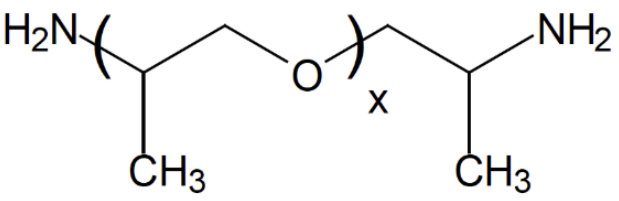

FIGURE 2.2: Chemical structure of Jeffamine D230 polyetheramine hardener.

The active hydrogen atom of the amine hardener (NH_2) reacts with the oxygen of the epoxy ring which opens the ring and an intermediate product with hydroxyl group is produced. These hydroxyl groups could react with another epoxy ring which could result in a highly cross-linked system.

The amine nucleophile has high electron density due to the presence of lone electron pair on the nitrogen. However, the carbon on the epoxy ring has low electron density. Since, the oxygen has two electron pairs it withdraws the electron from carbon making it electrophilic. The diamine's electrons are attracted to this electrophilic carbon next to the epoxide oxygen and reacts with it, resulting in a negative charge on the oxygen and a positive charge on the nitrogen as shown in Fig. 2.3 (a).

The extra pair of electrons on the oxygen attracts a hydrogen from the nitrogen which forms an alcohol and an amine group.This amine group is also a nucleophile again and can further react with another epoxy group (Fig. 2.3 b, c). Finally, when the amine group has reacted completely due to the lack of an active hydrogen it is no longer reactive and forms a tertiary amine (Fig. 2.3 d). Similar reaction occurs with the other amine on the other end of the diamine.

Due to the nature of reaction every epoxy-amine system produces hydroxyl groups. At higher temperatures during the process of curing and post-curing these hydroxyl groups may react with another epoxy group to produce ether [1]. This reaction is know as etherification reaction, illustrated in Fig. 2.3 (e). Combination of the these two types of reactions results in formation of a highly crosslinked network (Fig. 2.3 f).

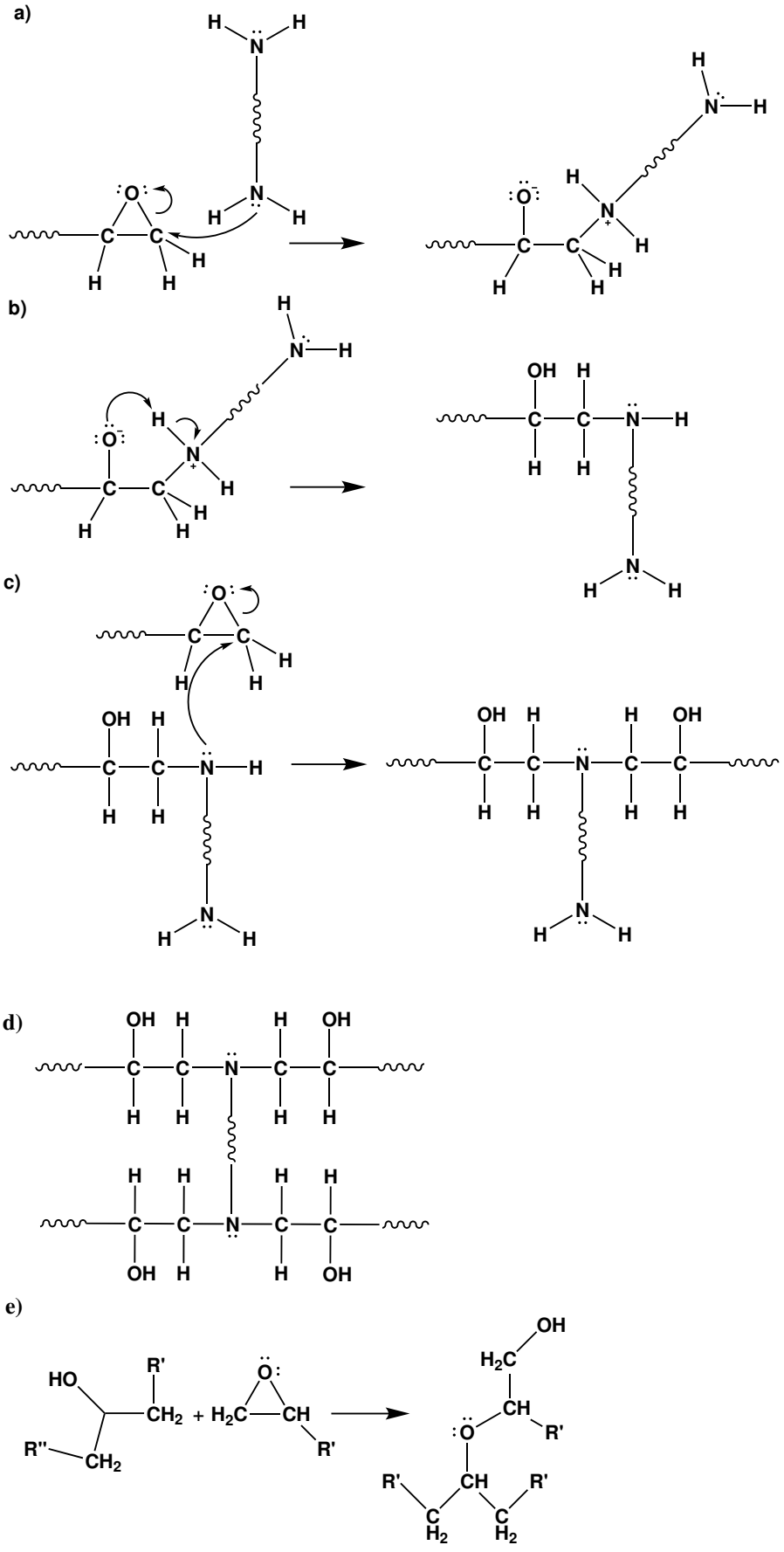
a)
b)
c)
d)
e)
HO
R'
R''
CH2 + H2C
CH
OH
H2C
R'

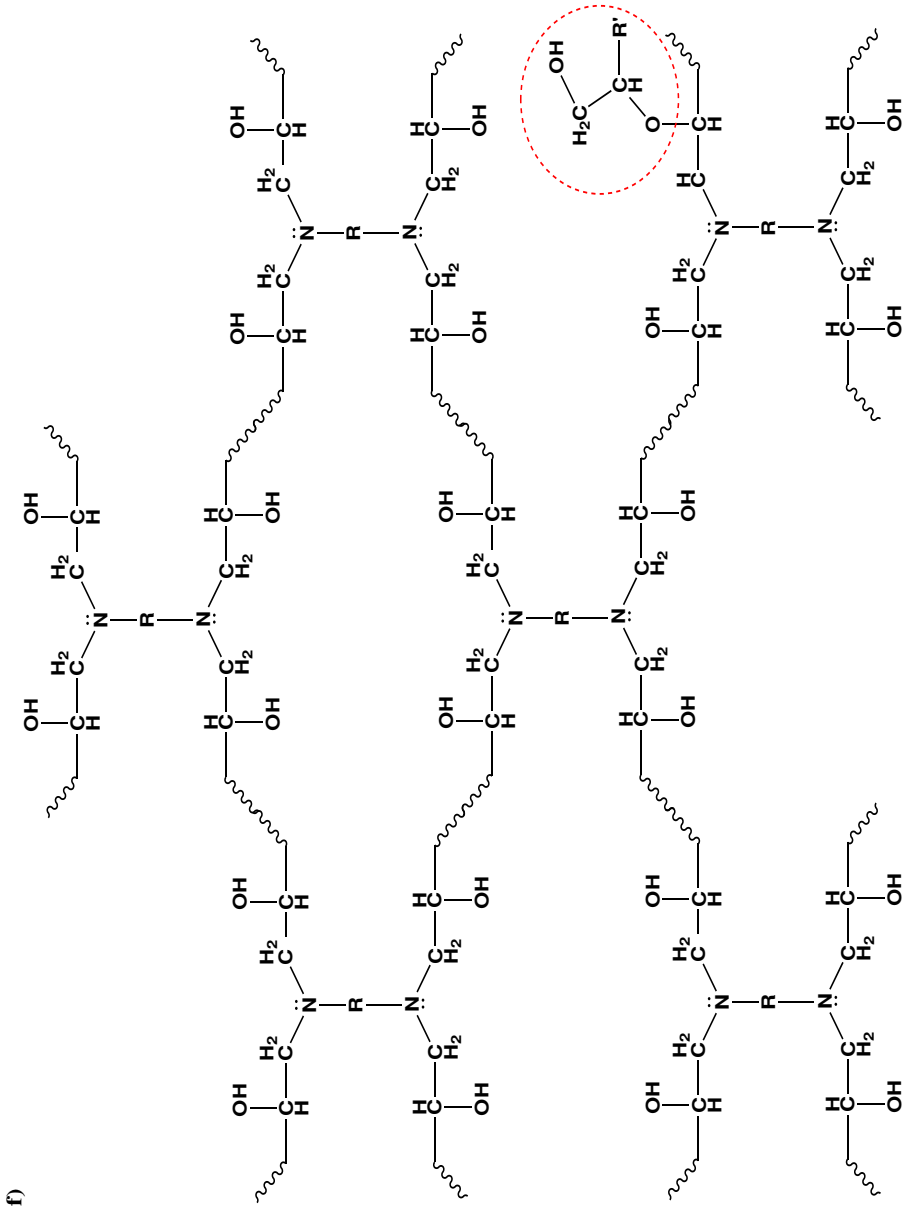

FIGURE 2.3: **a)** Amine group of hardener reacting with epoxide group of epoxy **b)** Primary amine reaction with epoxide group **c)** Secondary amine reaction with epoxide group **d)** Crosslinked structure after complete reaction of one hardener molecule with four epoxy monomers **e)** Etherification reaction **f)** Illustration of the highly crosslinked structure formed after the completion of curing process. The red circle represents the etherification reaction with the hydroxly groups.

2.3 Epoxy Nanocomposites

According to ASTM E2456 - 06 (28), nanoparticles are defined as a sub classification of ultrafine particle with lengths in two or three dimensions greater than 0.001 micrometre (1 nm) and smaller than about 0.1 micrometer (100 nm) which may or may not exhibit a size-related intensive property. They could have several varied size, forms and shape. Physical forms include cubes, spheres, flakes, plates and fibres. The idea of incorporating nanofillers inside epoxy has gained immense interest over the last decade as a result of enhanced electrical, chemical, mechanical and thermal properties offered by these nanocomposites. Novel multifunctional epoxy nanocomposites having a combination of better structural performance and even smart features such as strain monitoring, sensing and actuation capabilities have also been developed. Core-shell nanopartciles have been filled in epoxy matrix and used in variety of different applications such as improving the fracture toughness, enzyme immobilization (29), enhancing the dielectric properties, improving thermal conductivity and also in degradation resistance of the polymer composite.

In a study by S. Liu et al. (30) the mechanical properties of epoxy filled with nanosilica-rubber core-shell nanoparticles were investigated. The author reported an overall improvement in the Young's modulus, tensile strength, impact strength and fracture toughness of the nanocomposite. However, as a trade off small decrease in the T_g was also reported. These improvements were explained as a result of crazing, micro cracking and particle de-bonding from the matrix. The reduction in T_g was attributed to the low T_g of the shell, which is formed due to the grafted chains of P(CL-mLA)-COOH where CL refers to caprolactone and mLA to mesi - lactide groups in the chain. It is to be noted that introduction of core-shell structures can lead to micro cracking and particle de-bonding. Although in this study it is useful and leads to improvement of different mechanical properties. However, from high voltage perspective it would lead to degraded electrical properties as micro cracks or holes in the system could lead to partial discharge eventually decreasing the breakdown strength of the system. The reason for particle de-bonding leading to these deformation is assumed to be a result of phase separation between the nanoparticle and the epoxy matrix, which is based on separate studies done by other researchers. Similar results were reported along with same explanation of the underlying principles in a separate study by Giannakopoulos (31).

Core-shell nanoparticle filled polymer nanocomposite with high dielectric constant are newly developed and promising candidates as dielectrics in embedded passive-component technology. As an example, owing to these polymer nanocomposites capacitors can be embedded into the printed circuit board without having to occupy any surface area on the board itself. Many different strategies have been developed to achieve this such as to disperse ceramic powder with high dielectric constant in the polymer matrix. However, this also makes the polymer lose its flexibility and deteriorates their adaptability. To overcome this and form a continuous conductive path, percolative capacitors by using conductive

fillers have been fabricates. Nevertheless, it was observed that this leads to an increase in the dielectric losses. Further, core-shell nanoparticles were fabricated with a conductive core and dielectric shell. These nanofillers have been since reported as the ideal candidates since they not only provide barrier between conductive fillers but also the ability to tune the dielectric properties.

In a study by Shen et al. (32) dielectric properties of polymer nanocomposite filled with Ag/C (Silver/Carbonaceous) core-shell with different shell thickness was investigated. The unfilled epoxy matrix having a real permittivity of 3.7 was used for the study. It has been reported that due to the difference in the thickness of the shell, the electric constant enhancement is different. Near the percolation threshold the nanoparticles form a connected path between both the electrodes, each junction between nanoparticle acting as a capacitor; thus, forming a series connection. Using this hypothesis, it was then concluded (using Eq. 2.1) that the diameter of the core, thickness of the shell and permittivity of the shell are these parameters which can be tune to obtain desirable outcomes. It was also reported that cores with higher conductivity can deteriorate the dielectric properties of the nanocomposites.

$$\varepsilon \simeq \varepsilon_s(1 + \frac{d}{t}) \tag{2.1}$$

Similarly, in a separate study by Wang et al. (33) dielectric properties and thermal conductivity of epoxy composites using quantum sized decorated core-shell structured alumina polydopamine was investigated. It was stated by the author that the improvement in the thermal and dielectric properties of the system comes with a dilemma where employing high dielectric constant core-shell nanoparticles improves the thermal conductivity but at the cost of degrading the dielectric breakdown strength. this is one of the reason due to which the application in field of high voltage is limited. To overcome this, having a system with high thermal conductivity, good dielectric properties and acceptable breakdown strength the authors synthesised quantum size silver decorated alumina polydopamine core-shell structures where the presence of silver(Ag)nanoparticles at the chain ends of polydopamine forming a shell increased the breakdown strength along with thermal conductivity. It was explained that due to better compatibility between the filler and polymer matrix as a result of PDA (polydoapmine) layers resulted in decreased voids and other defects. The dielectric permittivity also improved as a result of interface compatibility and the Coulomb-blockade effect of the quantum sized Ag. Meanwhile,the incorporation of the strawberry-like core-shell particles shows enhanced thermo-mechanical such as T_g, thermostability and storage modulus. However, this is in slight contrast to the results mentioned in the improvement of toughness in (30) where the phase separation between the nanoparticle and the polymer matrix led to micro cracks in the system leading to higher storage modulus.

As seen in the results above core-shell nanoaprticles have been studied for different applications and in most case explanation of the underlying phenomena for the reported observations has been discussed. However, in a core-shell structure along with the interface between the polymer and nanoparticle shell (s-p interface) there is another interface which

present between the core and shell (c-s interface). This interface is not taken into account whilst discussing dielectric properties. It has been reported widely that any interface within a system should have some impact on the bulk properties. Even in the various hypothesised models interfaces and inter-phases are given utmost importance. The impact of the core is also an important parameter in most of the cases only one type of core with different shell structures is studied. However, since it has been highlighted that the diameter of the core is an important parameter. The type of core, chemical structure and the bonding structure with the shell could also be important parameters. The electric double layer model is one of the models widely accepted, in accordance to the model the charge on the surface of the nanoparticle leading to the formation of the electric double layer could be effected by the chemical structure of the nanoparticle itself. Another important parameter is whether the entire volume of the nanoparticle leads to the observed effects or is it only the surface characteristics, surface modification and compatibility of the nanoparticle surface with the polymer matrix. It is also important to study how the morphology of the system changes with different nanoaprticles. Changing the core and hence the internal bonding structure of the nanoparticle could potentially lead to morphological changes in the bulk system. These are some of the gaps in the literature and have not been widely investigated. They need to be studied and understood in order to design polymer nanocomposites with desired and applicable tailored properties.

2.3.1 Electrical Properties

2.3.1.1 Breakdown Properties

The effect of addition of nano and micro sized fillers on the breakdown strength of epoxy nanocomposites has been widely investigated. Although the findings are promising; however, not all fillers improve the breakdown strength. Most importantly, the understanding of the underlying principles and mechanisms is not as deeply understood. In an investigation by Tsekmes et al. (34) to understand the effect of nanofillers on the AC breakdown strength for a varied weight percentage of boron nitride filled epoxy system showed reduced breakdown strength. The reported results were claimed to be reproducible; however, no explanation has been provided for the phenomenon related to reduced breakdown strength. In a separate study by Donnay et al. (35) investigating the AC breakdown strength of boron nitride (BN) filled epoxy system contrary results were reported. The main conclusion drawn by the authors was that the addition of BN in epoxy matrix increases the breakdown strength approximately by 10%, regardless of the filler content with in the examined filling range i.e. 10%, 15% and 20%. In both the cases the epoxy was anhydride cured. However, the mixing method used was not the same.

Reading et al. (24) in an interesting approach reported that the mixing method affects not only the dispersion of the nanofillers in the nanocomposite but also the properties of neat epoxy. The author emphasised that different mixing methods result in different properties,

indicating that a good mixing methods results in enhanced performance regardless of the presence of nanofillers.

The authors in (36), investigated the effect 5 wt.% micro and nano Al_2O_3 fillers on the epoxy nanocomposite. It was reported that micro sized nanofillers reduced the breakdown strength by 56% whereas an increase of 5% was reported in case of nanofiller filled system. The reason for this observation stated that micro size fillers introduce defects into the polymeric network and claimed that this surface phenomenon is avoided in case of nanofillers as they do not have defects. However, the statement is not accurate. As the size of the particle reduces the surface area ratio of the filler increases, this increases the possibility of introduction of defects in the system. Various published work has also reported the presence and role of nanoparticle surface defects on various properties of the nanocomposite (37; 38). Further, in the work only the effect of size of the nanoparticle has been considered during the analysis. Since, both the particle types were treated differently where only the nanoparticles were modified to have better dispersion. The effect of different interfaces, arising as a result of different preparation method, which plays an important role as has also been reported and emphasised in different hypothesised models has not been considered.

2.3.1.2 Dielectric Properties

Permittivity is an important characteristic in case of dielectric materials. Hence, a vast amount of literature has been published on epoxy nanocomposites and their dielectric response in order to understand the underlying mechanisms for different relaxation process and molecular dynamics.

In a study by Singha et al. (19) the dielectric properties of epoxy resin filled with TiO_2, ZnO and Al_2O_3 with both micro and nano filler were investigated. It was reported that the real part of complex permittivity of TiO_2 is significantly higher than ZnO, even higher than unfilled epoxy for frequency range below 10^3 Hz at 10 wt.% filler ratio. This increase was explained as a result of the high permittivity of TiO_2 nanopartciles becoming dominant as the filler concentration increased. Further, in a separate study by Fothergill et al. (39) a similar system of epoxy nano and micro-composite filled with TiO_2 for 10 wt.% results were contradictory. Although, the real part of complex permittivity for microcomposite was higher than unfilled epoxy. However, in contrast to the results by Singha, the real part of permittivity was lower than the unfilled epoxy for epoxy nanocomposite system. This phenomena was explained to be as a result of nanoparticles restricting end-chain or side-chain movement. It is also reported to be consistent with the change in epoxy morphology as a result of change in composition associated with an increased proportion of hardener closer to the surface of the nanoparticle. The increase in real permittivity for microcomposite is argued to be a result of Maxwell-Wagner interfacial polarization. For nanocomposite system at lower frequency, a quasi-DC (QDC) behaviour is reported which is

also correlated with the intensity model and the formation of the Gouy-Chapman-Stern layer.

Different published literature emphasis and provides explanation of the sometimes similar observations based on different factors such as filler size and shape; chemical structure and synthesis method; interfacial effects; concentration and surface modification (40; 41; 42; 39; 19). Whilst all these explanations agree with different models and provide logical insight on the observed data; however, are contradictory at times. These results also emphasis that the dielectric behaviour of epoxy nanocomposites could very well be a result of combination of these factors. Hence, a step by step analysis of different parameters individually and then in combinations is required to have better understanding of their role and correlations between them.

2.3.2 Thermal Properties

Generally, in the literature increase or decrease in T_g of a filled epoxy network is explained based on two mechanisms namely, free volume and interfacial constrains. Other mechanisms such as absorption of the resin on to the nanoparticle surface due to its large surface area and lack of uniform dispersion are also hypothesised but no hard proof has been reported (43). The free volume effect is based on the introduction of free volume into the nanocomposite system as a result of nanoparticle addition, which increases as the loading ratio increases. This results in the molecular chains of the polymer having less constrained environment; thus, lowering the T_g as the chains are comparatively free to move unlike in unfilled nanocomposite system. Whereas, the interfacial constrain is a complex phenomena that occurs at the surface of the nanoparticle. It constrains the chain entropy which moves the T_g to higher values.

In a study by Kosmidou et al. (44), it was observed that at lower loading ratio in case of a TiO_2 filled epoxy nanocomposite the T_g value moved to higher temperature. This was explained as a result of interfacial interaction. Since, at lower concentration the nanoparticles are argued to be well dispersed and are considered to be have better interaction with the polymer chains. However, at higher concentration the authors hypothesised that the free volume dominates over the interfacial effect due to agglomerate formation; thereby reducing the amount of interaction of the polymeric chains with the nanoparticle surface.

In another work by Sun et al. (45), epoxy resin system filled with nano and micro SiO_2, Ag and Al_2O_3 were investigated. It was reported that nanofilled epoxy composite system showed lower T_g values than the epoxy microcomposite system. This was then explained as a combination of the both the two dominant effects occurring simultaneously i.e. introduction of free volume as well as the significant increase in surface area altering the surface kinetics. This is in contradiction to explanation by reported by Kosmidou, where the

interaction zone starts to overlap causing a reduction in the interaction with the polymer chains.

It has also been reported (46) that the curing and the post curing conditions i.e. the sample fabrication conditions also play a vital role in determining the amount of cross-linking in the polymeric system which in turn is related to the T_g. Higher degree of cross-linking shifts the T_g to higher temperature values.

T_g can be used to study the dielectric α-relaxation, monitor the viscosity and reactions of the material during curing process, which is one of the main factors that explains the behaviour of the final material. However, several combined factors affect the behaviour of T_g in filled epoxy system. Although, the evidence and explanations of the mechanisms might be valid certain contradiction exists. Since, determining the impact of these factors individually may not be possible but by controlling different parameters methodically and studying for correlation between different parameters could help better understand the underlying mechanisms altering the molecular dynamics.

2.4 Molecular Dynamics in Polymeric Model System

Polymeric systems are rather very complex[1]. One important factor causing this complexity is the chain conformation. An isolated macromolecule can have a large number of atoms covalently bonded leading to larger number conformations in space and time. Many other factors such as chain flexibility, the mean-square end-to-end vector of the chain and the mean-square dipole moment which affect the bulk properties of the polymer system are a direct result of these large number of conformations. Further more, these conformations have temperature dependence. For an amorphous system like epoxy at lower temperature the system behaves as a glassy solid where as at the glass transition temperature the system has visco-elastic properties. At still higher temperature the chains have increased mobility and the system becomes more rubbery or in some case flows like liquid where the shear modulus drops down to zero. However, some properties become independent of the molecular weight when the value is sufficiently high. For example, effects related to chain ends such as entanglements are different for short and long chains become less important in case of longer chains. Due to molecular fluctuations the mean quadratic value of the end-to-end vector also fluctuates over time. The dielectric properties of a polymeric chain depends on the polarization **P** which is the dipole density in a unit volume **V**.

$$P = \frac{1}{V} \sum_{chain} \sum_{monomer\,unit} \mu_i \tag{2.2}$$

where μ is the dipole of the repeating unit. For different length of chains there are different possibilities of orientation. It could be either the molecular dipoles fixed parallel to the backbone or attached perpendicular to the backbone or a more flexible side chain where the

[1] As scope of this study in most cases only molecular dynamics of amorphous systems are studied.

side group has the possibility of rotation. Although, there is no correlation between the dipole moment and the chain contour, the fluctuation of the dipole moment are mostly due to conformation transitions related to segmental mobility of the chains (47).

The current understanding of segmental motion is based on an idea by Helfand et al. (48), Skolnik and Yaris (49). It states when a conformational change occurs is disturbs the bonds and their angles. Hence, the possibility of the neighbouring chain to under go conformation is enhanced. This leads to conformational changes to diffuse along the chains. However, only the possibility of other surrounding chains to undergo changes is enhanced but not every transition will lead to a transition in the neighbouring chain. Hence, the change or the transition over time gets damped.

It is widely known due to extensive research that amorphous polymers exhibit a secondary -β and principle -α relaxation. β relaxation is located at higher frequency and lower temperature than α relaxation. In case of some polymers a further relaxation can also be observed namely the α' or normal mode relaxation. It is usually observed at lower frequencies than α relaxation. α relaxation is usually observed at higher temperature which is also related to the glass transition temperature. Figure 2.4 shows the plot of dielectric loss νs logarithmic frequency at varying temperature for poly(propylene glycol) showing two peaks. The peak at lower frequency represents the α' and one at higher frequency represents the α.

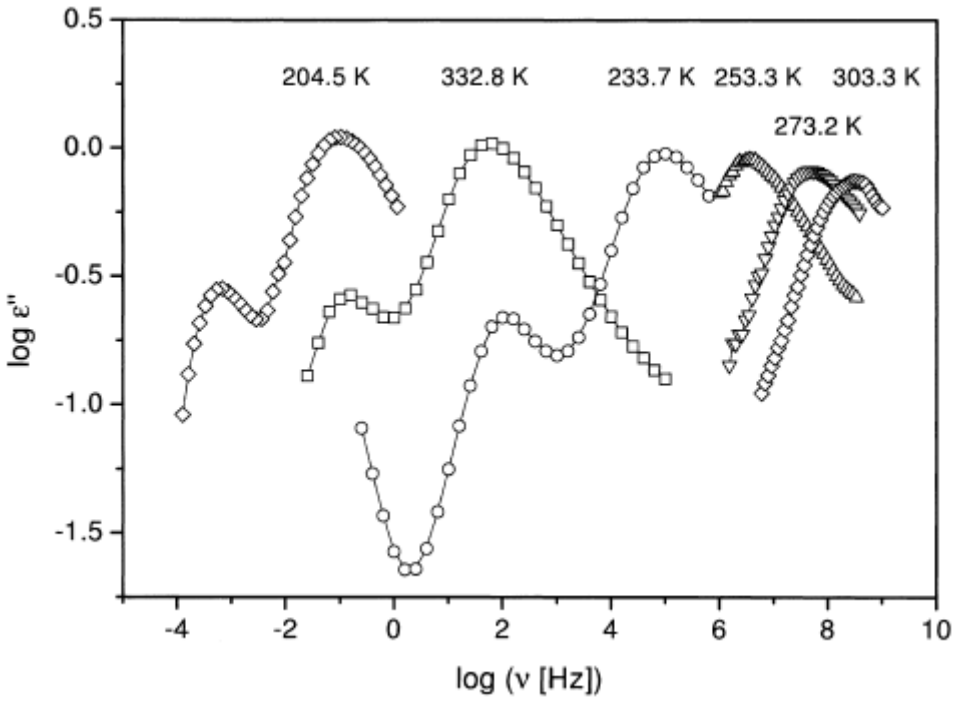

FIGURE 2.4: Dielectric loss ε'' for poly(propylene glycol) (M = 2000 g mol^{-1}) νs logarithm of frequency [Hz] at varying temperature [B1].

2.4.1 Alpha - (α) relaxation

Most of the published work agrees that for polymers the glass transition temperature T_g corresponds to segmental motion. Conformational changes such as gauche-trans transitions lead to rotational fluctuations of the dipole around the backbone chain in the side chain which is perpendicularly attached to the back bone. α relaxation is generally discussed in terms of its relaxation rate, dielectric strength and the shape of the relaxation function in accordance to different models hypothesised for this phenomena.

a) Relaxation rate: The relaxation rate is know to be temperature dependent. Usually this dependence can be described by using the Vogel/Fulcher/Tammann/Hesse (VFT) equation,

$$log\, v_{p\alpha} = log\, v_{\infty\alpha} - \frac{A}{T - T_0} \tag{2.3}$$

where $log\, v_{\infty\alpha}$ and A are constants and T_0 is the ideal glass transition temperature or Vogel temperature, usually found to be 30 - 70 K below the T_g.

The activation energy can also be calculated from Eq. 2.4. However, the activation energy near the glass transition temperature is much greater than the binding energy of C - C σ-bond. In a separate study by Yonggang et al. (50) and Williams et. al (51) a similar relation between the relaxation rate and temperature is discussed, given by,

$$log \frac{v_{p\alpha(T)}}{v_{p\alpha}(T_{ref})} = -\frac{C_1(T - T_{ref})}{C_2 + T - T_{ref}} \tag{2.4}$$

where T_{ref} is the reference temperature and $V_{p\alpha}(T_{ref})$ is the relaxation rate at the given temperature. C_1 and $C_2 = T_{ref} - T_0$ are WLF-parameters. With the help of these both laws the T_g of a polymer system can be approximated and in most cases shows good agreement (52).

b) Dielectric strength and shape of the relaxation function: The dielectric strength of the α relaxation $\triangle\varepsilon_\alpha$ decreases with increase in temperature. However, close to T_g the increase of $\triangle\varepsilon_\alpha$ with decreasing temperature is also a know effect (53). This temperature dependence is further emphasised when $T\triangle\varepsilon_\alpha$ is plotted vs T for several polymers, where it decreases with increasing temperature.

Many different models such as Debye, Cole/Cole, Cole/Davidson, Havriliak/Negami and Dissado/Hill have been proposed and hypothesised to understand the relaxation function. It is considered that the broad asymmetric α relaxation peak is an intrinsic feature of glass-forming systems. The width of the peak depends upon different factors namely, temperature, structure of chain and cross-linking density. The peak becomes narrower as the temperature increases and broadens significantly with cross-linking. The α relaxation usually leads to a dominant loss peak at $v_p \simeq v_t = 1/(2\pi\langle\tau_\alpha\rangle)$, where $\langle\tau_\alpha\rangle$ is the average relaxation time. Fig. 2.5 show different relaxation peaks highlighting the dominance

(amplitude) of the α relaxation over other relaxation processes. With increasing temperature this peak shifts to higher frequencies.

When mobile charge carriers are present in the system, conductivity contribution can lead to divergence of $\varepsilon''(\upsilon)$ at low frequencies since, $\varepsilon'' \simeq \sigma'/\upsilon$. Although the amplitude of conductivity contribution can completely dominate and suppress other features of the spectra. This is also seen in nanocomposite polymer system due to the interfacial effects where sometimes α relaxation peak is partially suppressed by conductivity contribution, as can be seen in Fig. 2.6.

In a study by Hassan et al. (54) the polymer chain dynamics of epoxy based composites were investigated. The linear segment observed at lower frequency is reported to be accounted in terms of dc conduction. In this experiment dc conduction is assumed to be a result of charge hopping and is argued that charge hopping pathways become longer at lower frequencies. As the half period of oscillation $(2f)^{-1}$ increases, the charge carriers can perform more hops before the field is reversed. All the linear segments at temperatures above T_g have slopes ≃ -1.0, which is usually a characteristic of dc conduction. The vertical elevation of these slopes with increasing temperature represents the increase in dc conductivity according to Eq. 2.5.

$$\sigma_{dc} = 2\pi\varepsilon_0 f\varepsilon'' \tag{2.5}$$

This behaviour is argued to be caused by chain segmental mobility due to its rubbery state combined with charge motions. At lower frequencies the ions have enough time to accumulate at the electrode interface. Based on this it is reported that these ions can accumulate on both the electrodes and can give rise to greater charge per unit area than those produced from simple dipole orientation mechanisms. Hence, the real permittivity ε' can be much higher than the actual bulk permittivity.

In a study by Andrews and Hammack (56) to account for the "local viscosity" effect a explanation for the α transition and associated peak was provided in terms of intermolecular cohesive bonding. The authors stated that if the mechanism of energy loss and dissipation into heat was to be explained it was first important to explain the storage of energy elastically and subsequently transformed into a thermal form. It was argued that below the T_g the bonding holds certain form of elastic energy, as the temperature increases the rigid structure distorts elastically and once the transition temperature is reached the bonds could no longer hold the elastic energy. It molecular terms the loss peak is explained as an combined effect of increase in population of mobile carriers and progressive decrease in local viscosity with increase in temperature. It was also stated that the polymer can have multiple form of cohesive bonding which could result in multiple loss peaks as observed in some cases.

In another study by Shito and Sato (57), the authors reported that the higher values of the glass transition temperature of the resin series can also be attributed to the existence of double bonds or ring structures in their chain backbones.

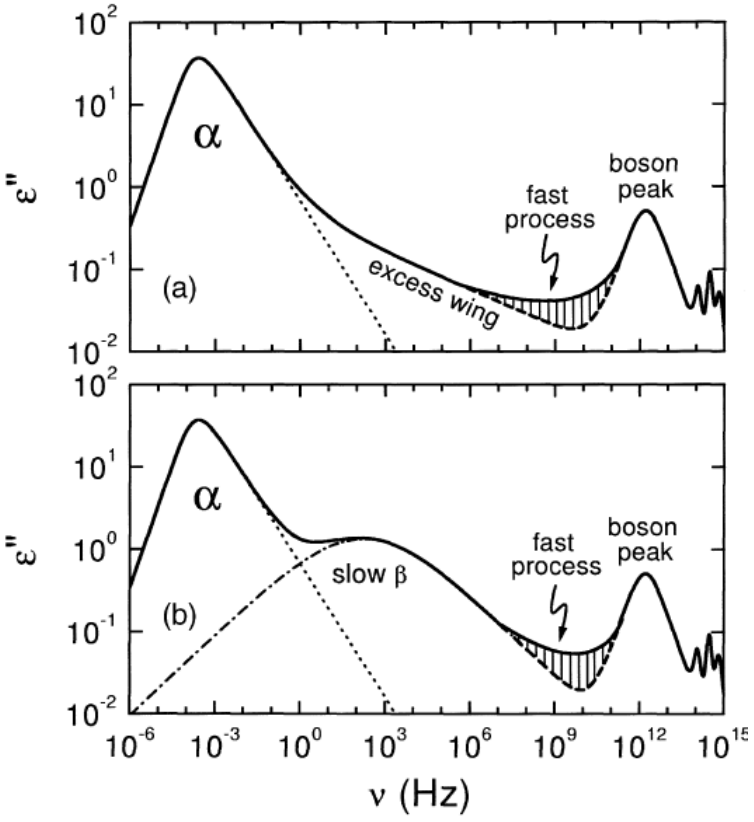

FIGURE 2.5: Illustration of frequency dependent dielectric loss with two cases **a)** fast β relaxation with excess wing and possible boson peak **b)** slow β relaxation process (53).

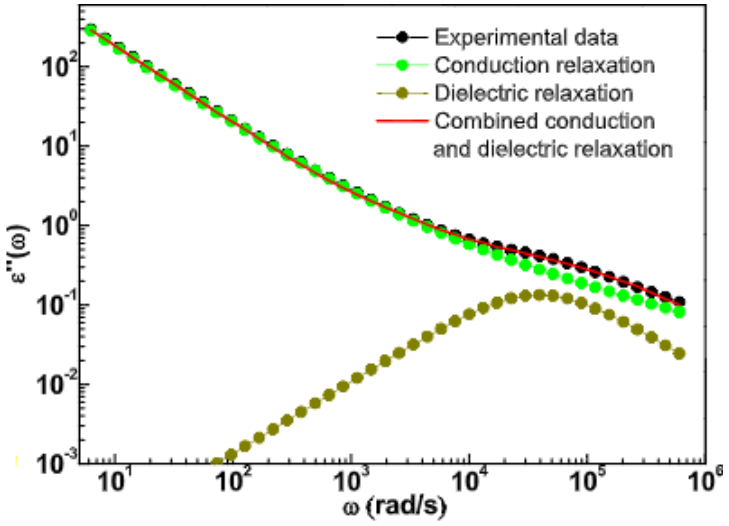

FIGURE 2.6: The imaginary part of dielectric constant at 463 K with the fit curve for α-Fe_2O_3 (55).

2.4.2 Beta - (β) relaxation

Heijboer et al. (53) in 1976 first studied the molecular origin of relaxation in polymers. The author developed a model to highlight the molecular mechanisms which could be responsible for these relaxation processes. Since then, authors agree that the dielectric β

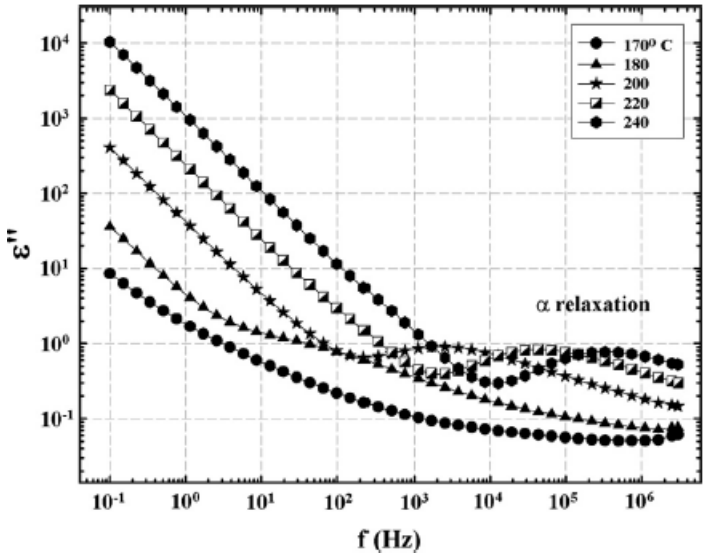

FIGURE 2.7: ε'' vs. f at different temperatures for epoxy networks formed using 33 BisA crosslinker showing the glass transition (a process) peak (54).

relaxation in amorphous polymers arises from localised rotational fluctuations of the side groups on the main chain. A reduction of the T_g because of the increase in the length of the side chain is also observed (58). In another idea outlined by Goldstein and Johari (59), the authors argued that β relaxation is a characteristic feature of amorphous state materials.

a) Relaxation rate: The temperature dependence of the β relaxation can be general explained by the Arrhenius law,

$$\upsilon_{p\beta} = \upsilon_{\infty\beta}\, exp\left[\frac{-E_A}{k_b T}\right] \tag{2.6}$$

where $\upsilon_{\infty\beta}$ is the pre-exponential factor. The activation energy E_A depends on the internal rotational barriers and environment of the fluctuating unit. Usually the values of E_A lies between the range 20 to 50 kJ mol^{-1}.

b)Dielectric strength and shape of the relaxation function: The dielectric strength of the β relaxation in comparison to α relaxation depends on the bond between the side chain and the main chain. Usually when the side chain is rigidly attached to the main chain $\triangle\varepsilon_\beta << \triangle\varepsilon_\alpha$. In case of polymers containing flexible side chain or group $\triangle\varepsilon_\beta \leq \triangle\varepsilon_\alpha$. The reason for this behaviour is unknown. However, NMR measurements provide little evidence that the behaviour could be a result of coupled main chain and side chain motion (60). The Onsager/Kirkwood/Frőhlich theory predicts that the relaxation could be understood using Eq. 2.7,

$$\triangle\varepsilon \simeq F_{Onsager}\, g\, \frac{\mu^2}{k_b T}\, \frac{N_p}{V} \tag{2.7}$$

given either number of dipoles N_p or the angular extension of the fluctuations increase with temperature. In the equation μ is the dipole moment, k_b is the Boltzmann constant, V is the volume of the system and g is the correction factor which changes with temperature.

However, it is considered that changes in g would not be significant below T_g since reorientation of the larger molecular dipoles below T_g does not seem possible.

The relaxation curve is usually symmetric and the relaxation function is measured based on the half height width of the loss peak which is usually broad. The width of the peak reduces with increasing temperature. The shape of the peak is considered to be a function of both the activation energy and the pre-exponential factor which is related to the molecular environment of the fluctuating dipole. A a general conclusion β relaxation could be either intra- and/or inter- molecular in nature.

Several studies have been done by many authors to understand the origin and mechanism leading to β relaxation. These different conclusions and explanations are covered here onwards.

- **Andrews and Hammack (56):** The authors cited an example where the β relaxation in a polymer was assumed to be resulting from the rotational motion of the ester side groups. Which is then correlated with the fact that this motion occurs in a constrained environment having local friction leading to the observed energy loss (β peak). However, in accordance to their cohesive bonding theory, the authors argued that the loss peak was a consequence of the loosening of the dipole-dipole association bonding between the ester side groups of the polymer, rather than activation of certain type of motion as a given temperature.

- **Dammont and Kwei (61):** The authors compared two analogous system to analyse the segmental motions of the highly cross-linked network as a result of diepoxide polymerization. For this purpose two systems of two structurally similar monomers, i.e., 2,2,3,3,4,4-hexofluoropentane diglycidyl ether-1,5 (6FP) and 1,4-butane digycidyl ether (Bu), and 2,2-bis(4-glycidyl phenyl ether)hexafluoropropane (GFBPA) and 2,2-bis(4-glycidyl phenyl ether)propane (BPA), were polymerized with the aid of two diamine curing agents, namely, ethylenediamine, H_2N-CH_2-CH_2-NH_2 and m-xylylenediamine, m-H_2N-CH_2- CBH_4-CH_2-NH_2, (mXD) for each monomer. Two main transitions were observed one related to the T_g and other relaxation which all the polymer sample system had in common. This relaxation was attribute as the β relaxation and hypothesised due to the commonly present hydroxy ether group. From this they also concluded that as the cross-linking increases with temperature the β relaxation becomes more prominent; since, the concentration of hydroxy ether group would also increase with curing.

- **Ding et al. (62):** The authors studied the dynamics of epoxy composite containing polycyclic aromatic hydrocarbon. The aromatic hydrocarbon used as filler was anthracene. It was reported that at low temperatures a relaxation process was identified as the β relaxation. It was recognised as comprehensive motions of hydroxyl ether and cross-links. No significant effect of additives on the activation energy of the β relaxation was observed, indicating that the local motions of hydroxyl groups as the

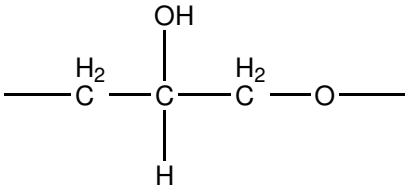

FIGURE 2.8: Hydroxy ether group

origin of the relaxation process. It is also stated that these processes were not affected by the molecular changes i.e. the attachment of anthracene and attractive π-π interactions between the anthracene and the bisphenol group of the epoxy.

- **Edward Cuddihy and Jovan Moacanin (63):** The authors studied five different type of polymer system with a common epoxy matrix namely Epon 828 with five different curatives namely, diethyemetriamine (DETA), DMP-30, metaphenylenediamine (MPDA), hexahydrophthalic anhydride and pyromellitic dianhydride. Two different cross-linked structure were formed. The structure A (Fig. 2.9) with primary and secondary amines like DETA and MPDA. Structure B with tertiary amines such as DMP-30 with diether and carbonyl groups. These structures were then evaluated based on different possibilities for rotational fluctuations. Upon examination is was reported that even though highly restricted the ether linkage of bis-phenol A can rotate. Further, it was stated that to have free mobility the diether linkage in the backbone chain must be stretched or should be in extended configuration. Any coiling could present enough steric interference to prevent movement.

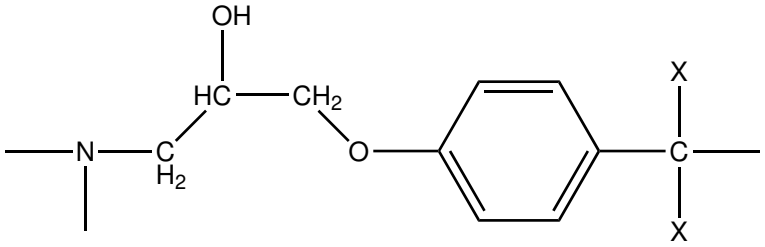

FIGURE 2.9: The structure of crosslinked strucutre "A" in investigation by Edward Cuddihy and Jovan Moacanin (63)

Rotation modes A, C and D (Fig. 2.10) are associated with segments which can occur in the backbone of the cured epoxy resin. Whilst the p-dioxane ring in rotation mode B can only be introduced into the backbone by epoxy-epoxy reactions catalysed by tertiary amines. DETA cured epoxy resin showed the highest amplitude of β relaxation due to three possible modes of rotation namely, the common mode A present in all system, mode C where the central secondary amine can rotate and finally the diether bridges which could be formed due to the presence of tertiary amines. It was reported that the amplitude of the relaxation mainly depends on the contribution and combination of these different rotational modes. However, the highest contribution comes from rotation mode A which was shown to be present in all the systems.Finally, it was concluded that the magnitude of the β-transition is a measure of total impact

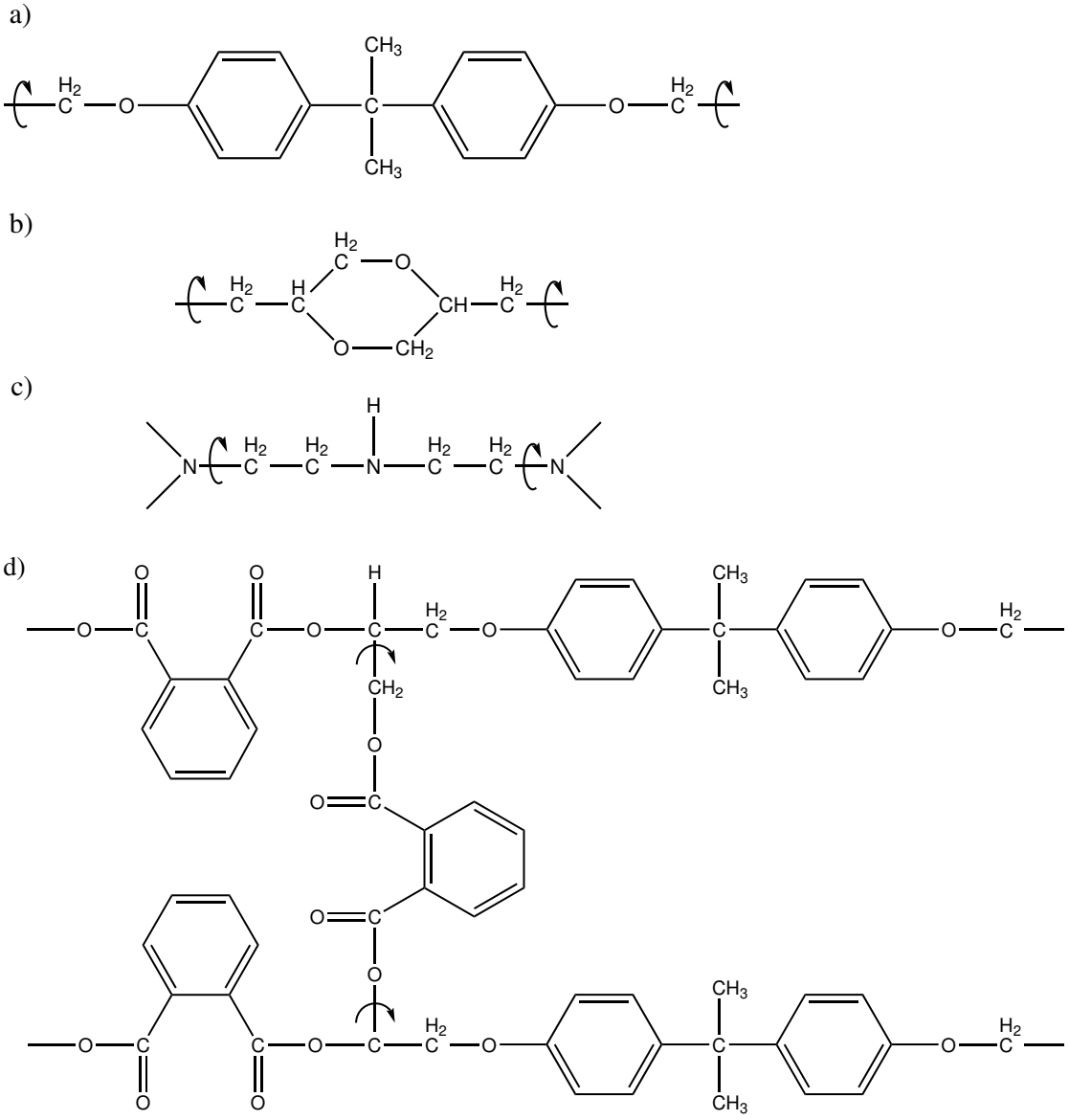

FIGURE 2.10: Different rotation modes **a)** Dimethylene ether linkage of bisphenol-A **b)** Epoxy-Epoxy reaction in presence of tertiary amine **c)** Rotation allowed in centrally positioned secondary amine in DETA **d)** Diether bridges from anhydride curatives.

potential while the actual impact value may be influenced by factors each such as thermal treatment, amorphous phase changes, stretching, cross-linking, or crystallinity.

- **Heux at al. (64):** The authors used three different system with same epoxy but cured with three different amine curatives namely, hexamethylene diamine (HMDA), hexylamine (HA) and dimethyl hexamethylene diamine (DMHMDA). The main objective was to understand the role of un-reacted epoxy and amine groups. Further, also to understand the respective roles of aromatic and aliphatic units in β relaxation process. The HMDA primary diamine cured system was reported to be the most densely cross-linked out of all the samples. It was reported that the height of the

maximum of β transition increases as the test frequency increases. It was concluded that this could not be a result of a single process and indicates the existence of several different processes. In case of a high frequency test, the low activation energy tends to overlap with the high activation energy processes and is regarded as the apparent activation energy. It is a combination of energies from all the different processes occurring simultaneously; thus, the β peak also becomes narrower and its maxima increases with frequency. Low values of activation energy is interpreted in terms of localised motion, whereas higher values corresponds to cooperative motions. Therefore, the low energy at the onset of the β relaxation indicates that low-temperature motions are localised. As the temperature increases along with localised motions cooperative motions also occurs and becomes significantly higher as the cross-linking increases. Thus, it was argued that the width and height of the β transition are decreasing functions of cross-link density. It was also reported that the cooperative process itself is a combination of several different processes. This conclusions was based on the observation that in the epoxy system cured with DMHMDA compared to others showed high mechanical losses. The DMHMDA acts as mesh extender where as the HA (primary amine) reacts as a side chain. The presence of DMHMDA between two epoxy groups allows spatial motions and increases cooperativity along the chain. It differs from the cross-linking cooperativity as the chain constraints are much weaker. The author states that the involvement of CHOH-CH_2-O (glyceryl unit) in β relaxation is well studied [VH] and the results presented are consistent. Based on this and the NMR study which revels the parallel behaviour of CHOH-CH_2-O and CH_2-N groups; it was concluded that cross-linking points are also involved in the β relaxation process. Measurements comparing the hydroxypropylether and phenyl rings of bisphenol A were also studied. It was reported that the steric hindrance for these rings to be able to flip is high and a direct coupling with the mechanical losses can not be established. However, a correlation between the oxygen next to the phenyl rings which is part of hydroxypropylether group was observed where a slight increase, possible due to the motion of the oxygen atom, in the bond angle between the two phenyl rings could reduce the steric hinderance causing the rings to flip. Thus, indicating an indirect coupling with the mechanical losses. In a similar study by Van Hoorn (65) the β relaxation was attributed to the phneyl ring rotations.

- **Soulintzis et al. (66), Shito and Sato (57), Jilani (67) :** The authors while studying the dielectric relaxation process in various types of epoxy resin composites reported that the β relaxation is a result of wriggling of the hydroxyl and/or carbonyl side groups and the orientation or reorientation of other polar side groups.

These variety of arguments and links to different specific processes over the molecular origin of the β-relaxation indicates the complication in the explanation of the phenomena. β-relaxation may involves two sets of mechanisms: the hydroxyl moieties in addition to their motion mode, which may be influenced by the chemical structure around them. The range of motion is depicted in Table 2.1.

Type of Motion	Reference
Crankshaft motion of six carbon atoms	Ochi et al. (68)
Crankshaft motion of hydroxyether	Dammont and Kwei
Ring rotation	Van Hoorn
Oscillation or wagging of phenyl groups	Sinnotto
Wriggling of hydroxyl and/or carbonyl side groups	Soulintiz et al.
Intermolecular bond loosening	Andrews and Hammack
Concentration of hydroxly groups	Ochi et al. (69; 70; 71)

TABLE 2.1: Different possible origins for β relaxation

2.4.3 Gamma - (γ) relaxation

To provide physical interpretation of relaxation processes in polymers usually a peak is assigned at a particular motion of the main chain, side chain or a group of the side chain or assign a understood mechanism to the process. However, understanding the mechanisms are far more complex. A mechanism or motion of the chains which might be true for one polymer might not be true for others. For example, secondary relaxation process such as β and γ are observed not only in amorphous regions but also in polymers which have no internal degree of freedom, owing to a special mode of segmental motion. These observed relaxations generally indicate dipolar motions in regions of dissimilar cross-linking density where the polymer chain, epoxy group or hydroxy-ether and unreacted molecular segment are loosely packed. Hence, these relaxations can be interpreted in terms of both a) the changing number and nature of the existing dipolar segments as the reaction progress and the changing internal arrangement and topology of the chains as the average chain length increase and the network densifies.

Various studies have been done to identify the nature and origin of the γ relaxation. In a study by Mangion and Johari (72), the authors argued that the γ peak is partly due to local motion of dipoles which remain unreacted including the unreacted epoxy groups, free amino-diphenyl or primary amine groups. It was also stated that the β and γ relaxations are connected. As the reaction proceeded the number of unreacted groups reduced and the cross-linking increased. Thus, as the polymer cures the γ peak reduces and the β peak starts to become more prominent.

Charlesworth (73) studied the effect of methylene sequence length on the secondary relaxation using samples cured with diamine containing 2 to 12 methylene units and samples cured with 2 to 4 methylene units in the central portion of the diepoxide monomer. The author reported that at least four methylene units are needed in the diamine component before the γ relaxation process is observable, whereas only two consecutive methylene units in the center of the diepoxide molecule produce the relaxation. Further, it was also stated that γ relaxation show behaviour consistent with crankshaft type rotation mechanism of the methylene groups.

Hassan et al. (54) reported that dielectric and nuclear magnetic resonance (NMR) studies of a diglycidyl ether of bisphenol A (DGEBA) based system revealed well resolved γ relaxation peaks. In accordance to NMR measurements it was reported that this transition was a result of phenyl rings flipping in the DGEBA main chain which implies adjacent flexible ether linkage. The author also cited another study according to which cahin sections between the cross-links are the only flexible group in a glass polymer and the conformation of the chains in a epoxy-aliphatic amine network depends upon rotation of five skeletal bonds.

In a study by Ochi et al. (68; 69; 70) two different systems were considered one with curing procedure involving only primary and secondary amines; and the other containing tertiary amines. Epoxide resins cured with aliphatic diamines in the absence of a catalyst contain significant amount of ether groups. Both the systems were denoted as amine cured and ether linked respectively. In the amine cured system hydroxyether group is generated as a result of reaction between epoxide and amino group. However, in ether linked system the curing reaction involves self polymerization of the resin, no hydroxyether groups are formed. γ relaxation was observed in resin cured with aliphatic diamines having four or more methylene units and no relaxation was observed in case of diamine having two carbon atoms or cured with tertiary amines. Hence, the authors concluded that the γ relaxation was caused by the motion of poly-methylene sequences of at least four carbon atoms.

Pognay in a publised work (74) specifically studied γ relaxation. He reported the observations and provided explanation for the effect of water , curing condition and chemical structure on the relaxation. A continuous increase in the area under the peak mainly due to its broadening at high temperature is reported until the curing temperature is reached after which the peak remains constant. Further, as the amount of curing agent increase the area under the peak increase but only until reaching the stoichiometric amount. Similarly, the temperature of the relaxation also increase upon increasing the concentration of curing agent but again only till the stoichiometric ratio is reached. Hence, concluding the area under the γ peak is proportional to the degree of cure. No effect of water was observed on the peak. Finally, given these observation the author stated that the most obvious origin of the γ relaxation is a result of reaction between the epoxy and the amine molecules. Therefore, coclusively reporting that the crank shaft motion of the -CH_2-CH(OH)-CH_2-O- group is responsible for γ relaxation. Further, also reporting that for polymers containing benzene ring in their main chain since the crankshaft motion is not possible the γ relaxation could be a result of wriggling motion of the groups containing the benzene rings.

2.5 The Role of Interfaces

It has been reported and hypothesised that the introduction of nanoparticles leads to formation of a layer consisting of immobilized polymer around each particle (76). As a result, the local chain conformation and chain kinetics are change (3). The depth and the

Type of Motion	Reference
Unreacted epoxide	Hirai and Kline (75)
Local motion of unreacted components	Johari and Mangion
Crankshaft motion of glyceryl units	Pogany
Rotation of methylene sequence	Soulintiz et al. (66)
Rotation of methylene sequence with atleast four carbon atoms	Ochi
Rearrangement of small parts of the polymer chain	Panglre et al.
Flipping of phenyl rings	Hassan

TABLE 2.2: Different possible origins for γ relaxation

density of trap sites is affected leading to either reduction or increase of carrier mobility and energy (77). This incorporation of nanoparticles in a polymer matrix has been shown to enhance the mechanical, thermal and electrical performance (19; 78). These improvements are attributed to the behaviour and characteristics of the interfacial interaction zone (79). According to Tanaka (80), an interface which is one tenth in thickness to the diameter of the nanoparticle its volume fraction contribution could be up to ≃ 50%. For a system consisting of spherical nanoparticles of diameter d, interfacial thickness t, the interfacial volume fraction f (assuming 2 t/d < 1) can be expressed as (80):

$$f = 3\frac{2t}{d}[1 - \frac{2t}{d} + \frac{1}{3}(\frac{2t}{d})^2)] \tag{2.8}$$

Having significantly high volume percentage demonstrates the important role of interfaces. Due to the small size of nanoparticles they have enormous surface area which gives the interaction zone two main characteristics:

a)The mobility, it depends on the chemical bonds formed between the nanoparticle and the host. Presence of nanoparticles and compounding conditions affect the movement of the polymer chain.

b) Formation of the double layer at the interface which may affect the local conductivity (81).

The mobility of the polymer chain is affected by different factors such as the length of the polymer chain (76), the surface morphology [26], nature of polymer - particle interaction (attractive or repulsive) (82) and the bond formation between the particle and polymer (83). A study conducted by Tsagaropoulos (76) investigates the effect of filling silica nanoparticle on the mobility of polymer chain. It is reported that for a 10 wt.% the chain movement is severely constrained and immobilized above 20 wt.% particle concentration. It has been investigated that high filler loading ratio alter the free volume of the system. As a consequence the possibility of the overlapping of interaction zone is higher. These overlaps may contribute to charge dissipation which could enhance the dielectric breakdown strength and voltage endurance characteristics (84). It is also emphasized that the interaction zone is "quasi-conductive" which overlaps partially (85). Scattering mechanisms

can also influence the space charge distribution upon introduction of second phase in a polymer system which causes the charge carriers to have an increased path length leading to higher breakdown strengths (86). For inhomogeneous materials, Maxwell Wagner polarization could also potentially arise due to charge carriers getting blocked at the interfacial layers (87). As the filler size approaches the chain conformation length the compatibility with the host increases which could suppress Maxwell Wagner polarization (39).

Further, the interfacial characteristics are significantly affect by aggregation. Homogeneous dispersion of nanoparticle is hard to achieve, the particles often tend to aggregate. Degree of aggregation is affected by different factors such as experimental conditions, particle shape, size and surface free energy of the particles (88). As the size decreases or the loading ratio increases the possibility of aggregation increases rapidly (88; 89). These aggregations have undesirable effect, they enhance the local electric field increasing the conductivity in a particular region leading to lowered breakdown strength (90), they act as stress points and due to their rough surface they induce voids through which destructive process can start leading to loss of mechanical stability (89). Aggregation can be prevented by surface treatment of nanoparticle to enhance the compatibility between the polymer host and the particles. It not only provides better dispersion but also increases the specific surface area of nanoparticles, improves mechanical stability as well as electrical properties (90). However, certain degree of aggregation is favourable in case of thermal conductivity as the overlapping of interfaces of the nanoparticles provide conduction path for the heat to be initially dissipated to surface of the nanocomposite and finally into the environment (91). The role of interfaces is widely based on explanations which are prominently based on interfacial characteristics. In a study conducted by Raetzke (92) shows that higher nanocomposite interphase content has higher resistance to tracking and erosion. Silane coupling agents used for stronger interfacial bonding between silica nanoparticles and epoxy resin showed a reduction in the mobility of charge carriers enhancing the resistance to partial discharge. It is also suggested that this enhancement could be a result of nanoparticles filling the space (free volume) thus decreasing the volume of epoxy resin (93). In a separate study it is pointed out that nanoparticle provide low trapping efficiency as the compatibility of particle-polymer interface increases (94). Most of the investigations conducted involve varying the filler concentration. However, in (95) an optimum value of filler concentration is reported with a conclusion that electrical behaviour is not only determined by the percentage of filler.

Based on the described mechanisms and observed experimental data it is widely agreed that interface/interphase plays an important role. Hence, numerous model has been hypothesised and theorised describing the physical, chemical and electrical characteristics in accordance to the interfacial interaction zone. Different models also refer to the interaction zone as either interface (surface area) or interphase (region with finite volume).

2.6 The Models

2.6.1 Tsagraopoulos's Nanocomposite Model

The Tsagraopoulos model assumes a structure with two layers around the nanoparticle, an inner tightly bound layer with extremely restricted polymer motion and an intermediate layer loosely bound examining a non-ionic polymer system. The inner layer is within the distance range of 1-20 Å from the nanoparticle and is considered to be physically adsorbed on the particle. As a consequence of the confinement the chain kinematics are slowed down. At distance above 20 Å the layer is considered to me moderately bound (76). The model specifically accesses the morphology of the polymer-particle system based on these layers. A third layer is also considered after 90 Å which is defined as the unrestricted bulk polymer. Physical interpretation can be assumed as increased concentration of nanoparticle leading to a decrease in the interparticle distance. Since the model assumes two regions with different mobility of the polymer chains around the particle, in principle it deals with nanocomposite systems showing two glass transition temperatures. Where the second glass transition temperature is explained as a result of loosely bound layer.

Investigation for the effect of increased filler percentage was performed using silica nanoparticles of 7 nm diameter. A critical amount of silica nanoparticles were filled into the polymer matrix, 10 wt.% was evaluated to be the critical weight percentage since at or above 10 wt.% two tan δ peaks were observed. The first peak observed was found at the T_g of the unfilled polymer, the position remains unchanged with varying weight percentage of the nanoparticle whereas the size reduced as the filler concentration was increased. The second peak observed was attributed to the glass transition of the polymer chains with mobility restrictions. To further provide evidence to the observed peaks, the filler concentration was further increased gradually and changes were observed until 50 wt.%. As the filler percentage increased the inter-particle distance decreased, eventually transforming the loosely bound layer to a tightly bound layer where the polymer chains were completely immobilised. Since the volume fraction of the loosely bound layer decreased it resulted in decrease of area of the second tan δ peak. At lower concentration the interaction between the particle and the loosely bound layer was reported to be stronger, as the concentration increases these interactions become weaker. Consequently as the immobilised layer does not restrict chain movement as effectively as the nanoparticle the T_g decreases. Reported data supported the claim, 10 wt.% having a T_g of 160 °C as compared to 110 °C for 20 wt.%. The reduction of the loosely bound layer causes the nanoparticles to act as barrier to flow of current between the electrodes.

The Nuclear Magnetic Resonance (NMR) data reported as part of the study conducted by Arrighi (96) provides justification to the model. In a separate study the data showed the detection of a Polydimethylsiloxane (PDMS) layer with different mobility above the glass transition temperature for a system filled with hydrophobic Aerosil (97) . Whilst investigating polymer blends of polypropylene (PP) and ethylene propylene rubber (EPR) a

second relaxation peak was observed explanation of which was provided based on the Tsagraopoulos' model (98). It is pointed out in a study conducted by Starr and Schroeder (99) that shifts in T_g is observed upon changing the interaction between the polymer and nanoparticles. The magnitude of shift is dependent upon the polymer to nanoparticle ratio. The results reported as part of the study investigating the epoxy nanocomposite for different filler concentration conducted by Wang (20) for dielectric response the results are explained basis on the Tsagraopoulos' model. The permittivity of the nanocomposite reduced as the concentration of nanoparticles increased due to the restriction on the mobility of the polymer chains. The observation regarding the two peaks in the tan δ plot initially reported as evidence for support to the model were also observed by others confirming the reproducibility of the data. A second thermal peak above the glass transition temperature for samples with 20 wt.% fumed silica were noted by Pitsa (100). Further, support to the model can be found in (101), where the author reported broadening of the tan δ peak to higher temperature as well as decrease in the magnitude of the peak, attributing to changes in the interaction between polyacrylnitrile (PAN) and antimony-doped tin oxide (ATO). Suggesting that the motion of the PAN closer to the ATO nanoparticle would be constrained from those further away.

Although the model is somewhat widely accepted it nevertheless has its weaknesses. In a publication by Bansal (102), the author emphasis that regions alone with different mobility cannot explain the glass transition temperature results reported. As claimed, such interaction effects are also observable in case of fictionalised nanoparticles, where for restricted geometries smallest inter-particle spacing would have dominant effect and glass transition would require interaction of surface regions resulting in altered mobility.

In conclusion regardless of certain weaknesses the Tsagraopoulos's model can be accepted as a nanocomposite model to specifically explaining and access the glass transition temperature. In summary suggesting that the two tan δ peaks observed in certain nanocomposite materials can be attributed to two layers, one which is tightly bound (restricted mobility) with a peak position at higher temperatures and the other peak (glass transition) due to the bulk polymer region as the loosely bound layer.

2.6.2 Tanaka's Multi-Core Nanocomposite Model

Tanaka's model (Fig. 2.11) consists of more than two layers therefore termed as 'multi-core' model. It has bonded layer around the nanoparticle which is the innermost layer which corresponds to a transition layer tightly bounded to both the inorganic and organic components by coupling agents such as silane. It has a thickness of $\simeq$1nm. The second layer is the bound layer, it is the interphase region consisting of polymer chains bound to the first layer and surface of the inorganic nanoparticle with an approximate thickness of 2 to 9 nm. Third layer is the loosely bounded which has weak coupling and interaction with the second layer. Finally, an electric double layer superimposed on all the other three layers mentioned. The bounded layer is bonded via ionic, covalent, hydrogen and van der Waals force. The

thickness of the second layers depend on the strength of the polymer-particle interaction, stronger the interaction the larger the polymer fraction. The glass transition temperature is directly correlated or explained based on the mobility of polymer chains and crystallinity of the second layer. The loose layer has completely different chain mobility, crystallinity, free volume and polymer chain conformation and is tens of nm thick. The final electric double layer is considered to form long distance dipole which is used to explain the conduction and dipole properties of the polymer nanocomposites (80).

Tanaka's model assumes that the nanoparticles are either positively or negatively charge. The charge is present on the nanoparticle due to the presence of mobile charge carriers. It is considered that such charge carriers are distributed through the interfacial region. Due to this charges of the opposite polarity are diffused outward from the surface to the Debye shielding length in accordance to the Gouy-Chapman diffuse layer and the charge decays exponentially based on the Born approximation. The model is used to explain the partial discharge and discharge treeing paths in polymeric nanocomposite materials. It is assumed that the introduction of positively or negatively charge nanoparticles tend to make the entire system negative or positively charged.

Most of the support to the model is based on the simulation results. In various studies it has been indicated that the treeing path propagates through the polymer and not through the nanoparticle (100; 103). In a study by Pista (100), is it shown via simulation that the presence of nanoparticles act as barrier to the propagation of the treeing. In accordance to the model it shows that the presence of charge with same polarity stops tree growth. Enhancement of the dielectric properties is explained on the basis of scattering mechanism due to the nanoparticles and the presence of homo-charge (104). Many authors have observed that the presence of nano-filler shows enhanced resistance to partial discharge and electrical treeing based on the data obtained from epoxy-alumina and epoxy-silica nanocomposite (105). Authors have also shown with photographic evidence that tree channels extend between nanoparticles expanding perpendicularly when they come in contact with the nanoparticle. It implies that as the tree grows thicker it starts interacting with the nanoparticle, which further suggest that trees are modified by the applied field, in turn modifying the nanocomposite morphology (106). It has been discussed extensively that the third layer of the model has dominant effect over the other two layers whilst considering the overall electrical properties of the nanocomposite (107). The model has also been used to explain charge percolation and presence of water shell around the nanoparticle. It is hypothesised that there are two layers of water. The inner layer is bound to the nanoparticle and the second layer is concentrated to be conductive. When these layers overlap with other layers it provides a channel for the charge carriers to move through the interaction zone (25; 108; 109).

However, the model fails to explain the crossover phenomena, where the tree propagation was observed to be different between the unfilled epoxy and epoxy nanocomposite material

under different voltages (110; 111; 112). It can also be argued that in Tanaka's model homo-charge are not assumed to be charge of same polarity, instead it assumes electric double layer for each nanoparticle reasoning that it is a result of triboelectricity (113).

Important terminology used and their definition:

a) Debye Shielding Length: Named after Peter Debye is used to measure the net electrostatic effect of the charge carrier and the distance till which the effect endure. The length in case of polymer nanocomposite is given by,

$$\kappa^{-1} = \sqrt[2]{\frac{\varepsilon_r \varepsilon_0 k_B T}{2 \times 10^3 N_A e^2 I}} \tag{2.9}$$

Where I is the ionic strength, ε_r is the dielectric constant, ε_0 is the permittivity of free space, k_B is the Boltzmann constant, N_A is the Avogadro number and e is the elementary charge (114).

b) Gouy-Chapman Diffuse Layer: According to Gouy the interfacial potential at the charged surface can attributed to the number of ions attached to the surface. These ions are not held at the surface they rather tend to diffuse into the phase with lesser density until a counter potential is set-up. It is assumed to follow the Boltzmann distribution and the thickness of the diffuse layer is given by,

$$\lambda_{double} = \sqrt[2]{\frac{\varepsilon_r k_B T}{r\pi e^2 \sum n_i z_i^2}} \tag{2.10}$$

Where ε_r is the dielectric constant, k_B is the Boltzmann constant, T is temperature, and e is the elementary charge, n_i is the concentration of ions in the given volume and z is the charge on the ion.

c) Born Approximation: Named after Max Born, the approximation consists of taking incident field at a particular location as the effective field instead of the total field in a well dispersed nanocomposite system. Originally taken and modified from scattering theory.

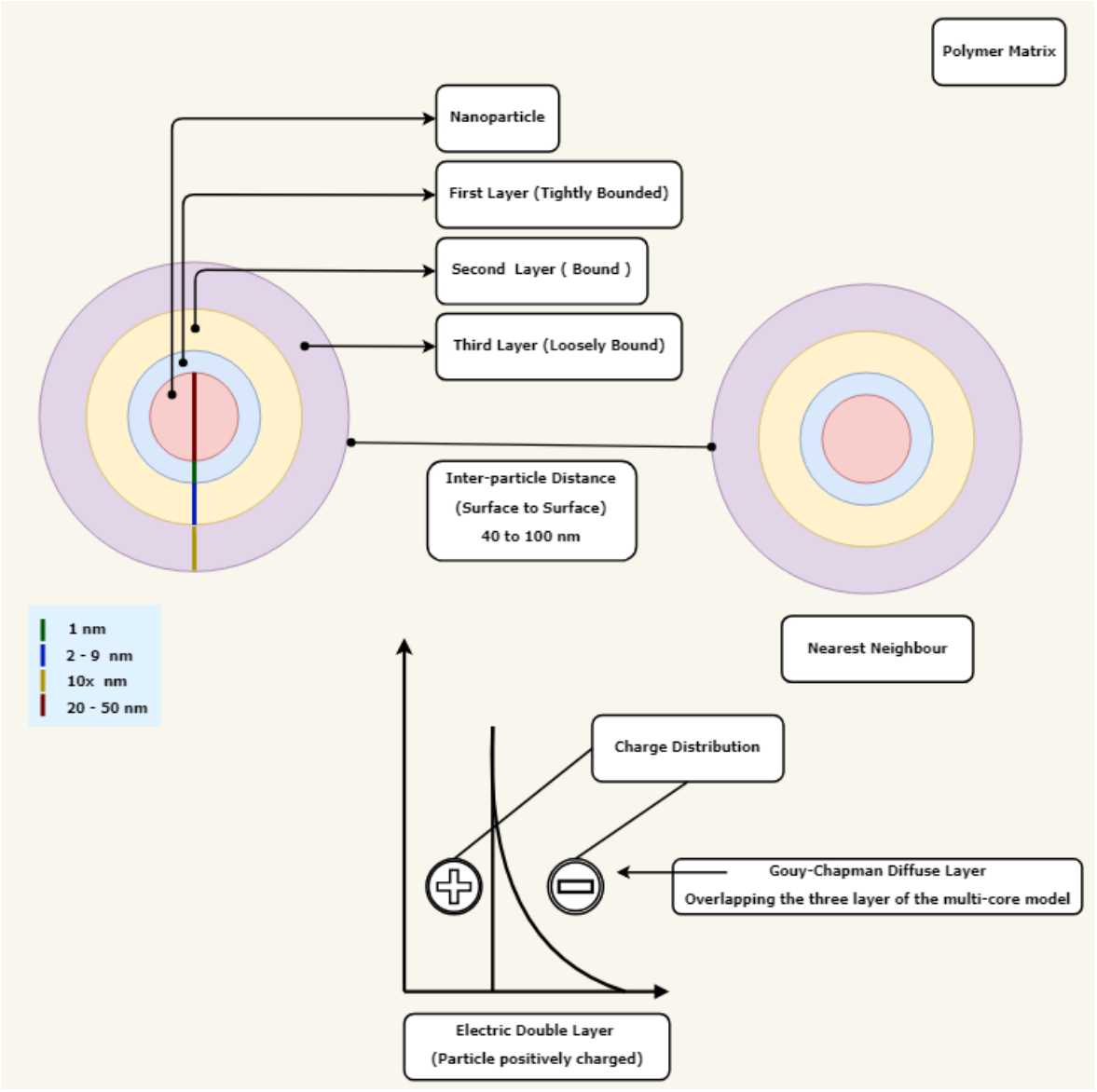

FIGURE 2.11: Tanaka's Multi-Core Model for nanoparticle - polymer interfaces (80).

2.6.3 Andritsch's Polymer Chain Alignment Model

The model is based on the data obtained from experiments with epoxy resin filled with nanoparticles (SiO_2 and Al_2O_3) which were modified with silane coupling agent (115). It assumes that the properties exhibited by the nanocomposite strongly depend on the processes prior to and during the polymerization process. It is reasoned that during the process of polymerization for an ideal case the polymer chain would align perpendicularly to the surface of the particle as a result of the inter-molecular forces between the chains. This leads to formation of an inter-penetrating layer whose properties are unlike the bulk phase i.e. neither the host nor the particle. It is further predicted that due to the alignment of these chains the region around them would also be affected. To explain the changes in the morphological structure a design analogous to crystallography is presented using a unit cell. The unit cell is considered to be of nano metric dimensions. A body centred cubic unit cell based on investigation via transmission electron microscopy (TEM) is selected to fit the distribution of nanoparticles. The dimensions of the cubic cell are dependent on the filler grade per volume and size of the filler. Based on these assumption the distance to the nearest neighbour is shown to be calculated as follows,

$$D_{nearest\_neighbour} = \frac{\sqrt[2]{3}}{2}(a-d) \tag{2.11}$$

Where $D_{nearest\_neighbour}$ is the distance to the nearest neighbour, a is the length of the cell which depends on the fill-grade per volume and d which is the diameter of the nanoparticle.

Experimentally with measurements from TEM, the best agreement was found with SiO_2 nanofiller. To compensate for the fact that TEM graphs are two dimensional, a correction factor of 30% was calculated for three dimensional analysis using approximation. In case of Al_2O_3 due to wider particle size and agglomerations the difference between ideal calculation and calculation from observed data was more than 40%. An excess of silane coupling agent was used to increase the probability of reaction with the surface of the nanoparticle. Which leads to a silane coupled layer to be of thickness in range of Å to some nanometre. Due to the intermolecular forces the chains align parallel to the surface of the nanoparticle which leads to formation of a rigid structure. As the distance between the nanoparticles increase the rigidity reduces and the system becomes more amorphous. The model considers two layers, an inner layer where the chains are perpendicularly aligned and the outer layer which is the bulk polymer matrix which. Outer layer includes the extend chains from the inner layer (not necessarily perpendicularly aligned outside of the inner layer). As the loading ratio increases the distance between the nanoparticle reduces and the outer layers will start overlapping. Further, at very high particle density the inner layer will start overlapping as well.

As effects of the chain alignment it is demonstrated that at lower loading ratio the nanoparticles change the material morphology. However, the effects do not scale as the loading ratio increases. Conduction mechanism is explained based on the attraction of charge carriers on the surface of the nanoparticle. According to this phenomena the

electrons can travel between the chains to approach the particle which makes the particle negatively charged attracting holes to the surface travelling along the polymer chain result in a recombination. In relation to the influence on the materials it is argued that the particle size and the amount of hydroxyl groups on the surface of the nanoparticle determine the reaction of the polymer chains. Near to the particle the intermolecular forces are stronger leading to alignment. However, at distance greater than one molecule the forces decrease. Along with the effect on crosslinking, the rigidity of the system also decreases.

Effects on the electrical properties reported show that the breakdown strength reduces significantly as the loading ratio increases. The reduction is attributed to the presence of agglomeration where the overlapping of the silane and polymer layer act as weak spot enhancing the local field which adds up to the applied field strength resulting in an earlier breakdown. It is also argued that the addition of nanoparticle in the polymeric host leads to enhanced resistance to electrical treeing and partial discharges. Due to the presence of the aligned chains with covalent bonding, higher energy is required to break the bonds along with the energy consumed in deflection of the tree by a nanoparticle. The author argues that due to the high interface volume and due to the alignment of the chains the permittivity of the system reduces. However, as the loading ratio increase the bulk permittivity increases as the high permittivity of the nanoparticle dominates over the effect of the aligned chains. In accordance to the space charge measurements the model suggests that although nanoparticles act as recombination centres, the agglomerations act as charge traps which leads to large interfacial polarization resulting in charge accumulation.

2.6.4 Lewis Intensity Model

In 1994, Lewis highlighted the importance of interfaces, considering them as areas of altered electro-chemical-mechanical behaviour, in nanocomposites (1). The proposed model (Fig. 2.12) considers an interface between two uniform material phases A and B. Each atom and molecule of the system interacts with its surrounding via a combination of short and long range forces. Each phase has its own mean bulk properties. As the boundary of the other phase is approached these forces will become increasingly modified and upon crossing the boundary will become characteristics of that phase. The regions where these properties are completely different from the bulk phase is defined as the interface ab. In general these can be any property (α) physical, chemical, electrochemical potential, electric field or the dielectric permittivity. The thickness of this interface (d) is ill-defined since the local intensity of these properties approach the bulk phase mean property values asymptotically. The interface is considered to be of one dimension implying that conditions in other dimensions are uniform. The thickness d depends on the range of forces existing, short range forces can lead to an effective thickness of less than 1 nm but to a maximum of 10 nm. The model is proposed based on a well-accepted thesis that, "interfaces" play a major role in controlling the electron and ion transport through macroscopic "dielectric systems". Secondly, on the fact that concepts in electro-chemistry are constructed based on the selective electron transfer across interfaces of nanometric thickness (116; 117; 118).

Interfacial areas or "patches" are considered to be heterogeneous with particular ab properties. As the size of the particle reduces the effect of interfacial properties ab will become dominant (119). It is argued that if the interface is determined by short-range forces, then the interface volume exceeds 50% of the particle volume for particle small than 5 nm, at such small size the interfacial properties will start to change as the bulk phase properties of the particle. It is highly asserted that interfacial properties should be a major design condition.

2.6.4.1 The Model and Interfacial Forces

Based on the intensity (I) of property α which depends upon the localised atomic and molecular forces, the interfacial forces are defined and categorised. Repulsive short-range forces exist in the adjacent surrounding of the atom which are result of quantum mechanical interactions and are responsible for bonding, charge transfer and steric interactions. Another highly directional short-range force is the hydrogen bond. Long range forces are all electrostatic in nature giving rise to ionic (columbic forces) and dipole (permanent and induced) interactions. Other moderately ranged dipole related polarization are usually attractive in nature and are knows as van der Waals forces.

Unipolar charges and their distribution plays an important role in the dielectric phenomenon. The distribution of charge is affected by the geometry of its surface. Considering A (nanoparticle) to be spherical an approximation was initially develop which was further extended into electrical layers of ab interface. The repose of a nanoparticle sphere of radius a with a ionic charge ze where e is the electronic charge and z is the valency was found using the Born approximation (120). The energy associated with electrostatic polarization was calculated using,

$$\frac{z^2e^2}{8\pi\varepsilon_0 a}\left(\frac{1}{\varepsilon_o p}-\frac{1}{\varepsilon_s}\right) \tag{2.12}$$

Where ε_0 is the free space permittivity, $\varepsilon_o p$ is the optical permittivity and ε_s is the static permittivity.

The model was the then further developed considering a quasi-planar interface ab. The interface ab is described in terms of charged layers which determine the dielectric characteristics. A formation of three layers was assumed. On the nanoparticle side (A) of the interface a double layer associated with surface states associated to the charged impurities, trapped carriers and mobile charge carriers is formed. Next layer considered is the Stern-layer or the Outer Helmholtz Plane (OHP), which may have high charge density. The side A of this layer consists of ions and dipoles and side B (polymer side) is the induced or attracted charge due to the excess charge on the side A. The third layer extends into the phase B (bulk polymer) which is the Gouy-Chapman layer. It forms a diffused charge layer as a consequence of the field resulting from the charge on B side of the Stern-layer. The thickness of the diffused layer is inversely proportional to the conductivity of the bulk phase

B (polymer). Diffused layer plays and important role in determining the dispersion of nanoparticle (A). Further, it also helps in determining the dielectric and conductive properties of the system.

The potential distribution function following continuum mean field approximation for the diffused layer is given by,

$$\nabla^2\psi(r) = -e\varepsilon^{-1}\sum_i z_i n_i(\infty)e^{\frac{-z_i\psi(r)}{kT}} \tag{2.13}$$

Where $\psi(r)$ is the potential which is a function of distance r from the Stern-layer, ε is the effective permittivity, z_i is the ion valency, n_i is the ion concentration in phase B (polymer), k is the Boltzmann constant and T is the temperature.

The charge density of the diffused layer is given by,

$$\rho_i(r) = \rho_i(\infty)e^{\frac{-z_i\psi(r)}{kT}} \tag{2.14}$$

Where ρ_i is the charge density as a function of distance from the Stern-layer.

Finally, the charge density can be related to the surface density by,

$$\sum_i[\rho_i(0) - \rho_i(\infty)] = \frac{+\sigma^2}{2\varepsilon kT} \tag{2.15}$$

Where $+\sigma$ is the net positive surface charge density at the Stern-layer.

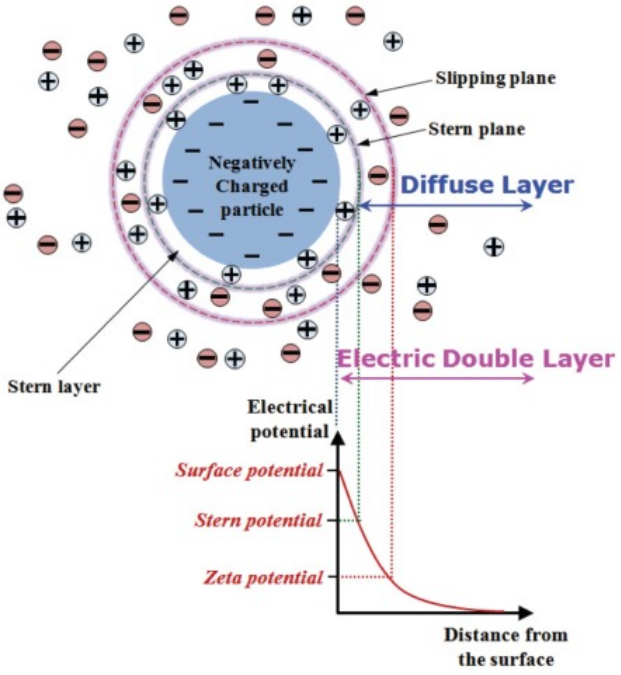

FIGURE 2.12: Distribution of electrical potential $\psi(r)$ in Stern and Gouy-Chapman layers with plot of Ion concentration $\rho_i(r)$ in the diffused layer (121).

Since the diffused layer consists of mobile charge carriers and ions it has lateral properties. Depending upon the potential distribution it will drive lateral current across the interface. The interfacial conditions assumed to develop the model are based on long range columbic interactions between the charge nanoparticles (A). The model also assumes that electron-hole recombination occurs at the particle surface. This property is used to explain the behaviour of the polymer-nanoparticle system under electrical stress. The recombination terminates the movement of the electrons between the electrodes which reduces the space charge (122). It is also assumed as the loading ratio increases the diffused layer from different particle will overlap providing a conduction path (116; 117; 118). Hence, the bulk charge accumulation is reduce which improves the breakdown strength of the system (81; 123).

2.6.5 Raetzke's Volume Interphase Model

Most of the hypothesized model explain the enhancement of the electrical, thermal and mechanical properties of nanocomposite systems as the effect of the interfaces. Unlike these models, the Raetzke's model (124) argues that the area formed around each nanoparticle due to their interaction with the polymer matrix should be considered as an interphase with certain thickness. In this region the polymer chains are chemically or physically bonded to the particle surface leading to a morphological different structure compared to the remaining bulk amorphous matrix. The interphase fraction is estimated based on simplified dimensions, d the diameter of the nanoparticle, I thickness of the interphase and V_p the filler concentration. For these estimation the model makes following assumptions,

a) Particles are spherical and have constant interphase thickness.

b) All particles have same diameter and

c) Homogeneous dispersion of particles.

The calculation of parameters is based on body centred cubic geometrical structure, having distance a between any two adjacent neighbouring nanoparticle on the vertices of the cube. Different parameters such as the particle shape, size, concentration, thickness of interphase and dispersion can affect the overall behaviour of the system. According to the calculations performed it is estimated that with a particle diameter of 10 nm and filler fraction of 10 vol.% the interphase fraction can contribute up to 70% volume. With such high volume fraction the interphase can have dominant effect on the nanocomposite properties.

The author argues that the interaction zone should be considered as a region with a certain thickness (1-10 nm) depending upon the bonding with the particle surface rather than only two dimensional region. The chemical bonds formed between the surface of the nanoparticle and the polymer depend upon the presence of surface groups and polymer

side chains. Therefore, surface treatment of the nanoparticle surface can have remarkable effect on the interphase. The author also argues that the non-polar groups can become polar due to such treatment. The model assumes three layers similar to Tanaka's multi-core model but does not take into account the electric double layer superimposing the other three layer. The three layers are namely, transition layer, bound layer and loosely bound layer (80).

The model derives the thickness of the interphase based on Tanaka's multi-core model using bond distance and atomic diameters of range 0.1-0.3 nm (80). The tightly bound layer is estimated to be within the thickness range of 1-1.5 nm. It is assumed as the sum of the topmost layer of the particle including the bonded atom layer of 0.4 nm thickness. The second layer thickness depends on the conformation thickness of the polymer chains, hydrogen bond and dipole-dipole bonds. The stronger the bonds thicker the second layer is considered. The approximated thickness has a range of 1.5-8 nm which assumes the polymer chains having a diameter of 0.3-1 nm and bond distance of 0.5-0.8 nm. The third layer which consists of the loosely bound polymer chains is assumed to have a thickness in the range of 1-3 nm. Based on all the above assumptions the entire thickness of the interphase is approximated within 3-12 nm.

Based on the approximated thickness of the interphase the model then validates it based on different range of inequalities,

$$\frac{2}{\sqrt[2]{3}}(d+2i) \leq a \tag{2.16}$$

$$(d+2i) \leq a \leq \frac{2}{\sqrt[2]{3}}(d+2i) \tag{2.17}$$

$$\frac{2\sqrt[2]{2}}{\sqrt[2]{3}}(d+2i) < a < (d+2i) \tag{2.18}$$

$$a < \frac{2\sqrt[2]{2}}{\sqrt[2]{3}}(d+2i) \tag{2.19}$$

Effect on interphase fraction for different range of validity,

- The interphase fraction increases linearly with the filler concentration.
- The interphase fraction still increase linearly with filler concentration but the steepness of rise is decreasing.
- The interphase fraction is decreasing as the filler concentration increases.
- If the entire polymer consists of interphase, the interphase fraction is decreasing with increasing concentration.

The result were then confirmed experimentally. High voltage arcing resistance was measured as function of increased filler concentration. The investigated materials were silicon rubber

filled with nano fumed silica, and micro fumed silica with particle diameter of 30 nm and 250 nm respectively. As the filler concentration increased the resistance also increased. The effect of improved resistance however was less pronounced in case of micro filler. Since the interphase fraction for nano fumed silica is much larger then micro fumed silica the model shows good experimental validation.

2.6.6 Other Models

A three dimensional electrostatic model was proposed to describe the field distribution of a spherical nanoparticle whilst considering homogeneous dispersion based on the multi-core mode. The impact of thickness of the layers, concentration and permittivity of the nanoparticles was also explained based on this model (125).

Another model describing the multi region based on the treated and untreated nanocomposite was also proposed. The assumed two region were the transitional region and the bonded region. The bonded region composed of the polymer chains bounded to the nanoparticle due to the presence of ionic, covalent, hydrogen and van der Waals bounding. The changes in this region were explain as a result of the changes in the Fermi levels of the nanoparticle due to different kinds of bonding and formation of a Stern-layer. The transitional region consisted of the polymer chains bound to the bounded region chemically. This region was considered to be crystalline in nature. The cohesive energy density of the polymer which determines the intermolecular forces and flexibility of the polymer chains were defined to be the characteristics of this region. Thickness of the transitional region is assumed to be greater than the bounded region. The thickness also influence the breakdown strength of the system. Where increase in the thickness was directly proportional to the increase in the breakdown strength. It is further explained that as the concentration of nanoparticles increased these region start to overlap which makes the influence of the nanoparticle dominant on the entire nanocomposite system (126).

A water-shell model to explain the effect of water absorption on epoxy nanocomposite in a humid environment has also proposed (25). The model is based on Lewis's and Tanaka's model, it assumes the formation of a water shell around the nanoparticle. The first layer is tightly bounded to the nanoparticle and the second layer which is highly conductive in nature consists of water which is loosely bound to the first layer by van der Waals forces. The concentration of the water present in the bulk polymer system is examined to be lower than around the nanoparticle. It is predicted in accordance to the model that epoxy nanocomposite are more prone to degradation in humid environment due to absorption of water (127). The accumulation the water as a shell degrades the interfaces and upon percolation provide a path for conduction which leads to electrical breakdown. To explain the percolation of water shell another model was developed. According to this model the probability of percolation was considered to be a function of water content and nanoparticle geometry (128).

Another dual layer model based on Tsagaropoulos's model to explain the glass transition temperature and enhancement of degradation resistance related to partial discharge was proposed. According to the model, between the loading ratios of 0.1-0.5 wt.% the mobility of polymer chains in the bound layer increased which decreased the glass transition temperature. As the loading ratio increases the volume of the tightly bound layer increases which increases the glass transition temperature. It is assumed that mobile polymer regions are comparatively more resistant to electrical degradation (19; 129).

Note: All the discussed models are illustrated together in Fig. 2.13 for comparison.

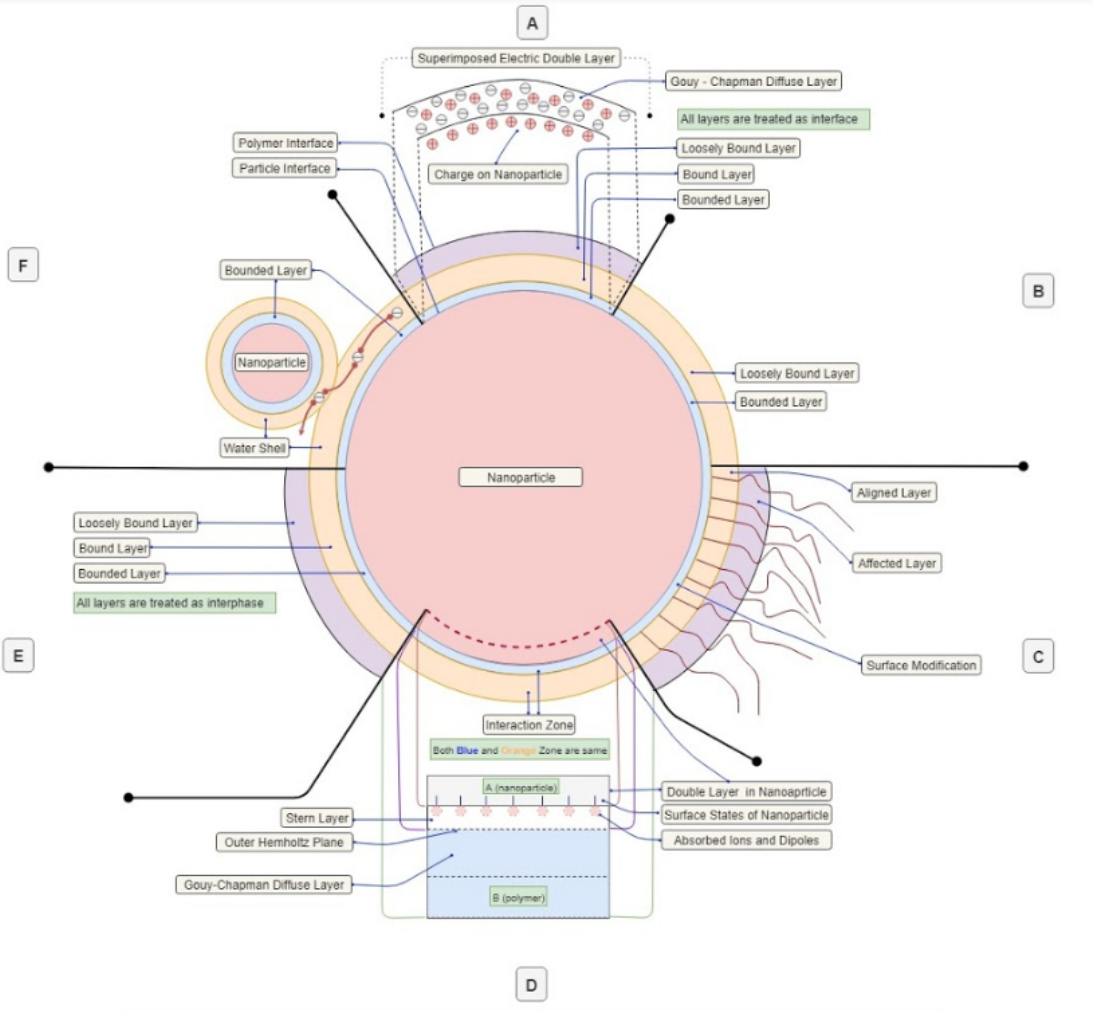

FIGURE 2.13: **a)** Tanaka's multi - core model **b)** Tsagraopoulos's dual layer model **c)** Andritsch's polymer chain alingment model **d)** Lewis's intensity model **e)** Raetzke's volume interphase model **f)** Water - shell model

2.7 Core - Shell Nanoparticles

2.7.1 Classification

Conventionally nanoparticles are made up of only one material where as in case of core - shell nanoparticles as the name suggests they are made up of two or more types materials. They can be classified based on their core (inner material) and the shell (outer material). They can consist of wide range of combinations such as:

- Inorganic/Inorganic
- Organic/Inorganic
- Inorganic/Organic and
- Organic/Organic
- Core/Multi-Shell
- Moveable Core or Hollow Shell

The choice of both the material is strongly dependent on the application. They can vary in their shape as well, however, the most commonly seen shape is concentric or spherical (11).

Inorganic/Inorganic and Inorganic/Organic type can be further divided into different types depending upon application as follows,

- Inorganic/Inorganic Core - Shell Nanoparticle
  - Based on presence or absence of silica
    - Including Silica (Au/SiO_2)
    - Excluding Silica (Ni/Au)
  - Semiconductor Core - Shell Nanoparticle
    - Semiconductor/Non-Semiconductor (Fe_2O_3/TiO_2)
    - Non-Semiconductor/Semiconductor
    - Semiconductor/Semiconductor
      - Shell material with high band gap (Type I) (CdSe/CdS)
      - Shell material with lower band gap (Reverse Type I) (ZnS/CdSe)
      - Core, Shell band gap staggered (Type II) (PbTe/CdTe)
    - Core/Multi-Shell Semiconductor ($InAs_{1-x}$/InP/ZnSe)
  - Lanthanide Nanoparticle (Lanthanide Group - Rare Earth Ions) (LaF_3/TiO_2)
- Inorganic/Organic Core - Shell Nanoparticle

- Magnetic/Organic (α - Fe_2O_3/Dextran (polymeric shell))
- Nonmagnetic/Organic
  - Metal/Organic (Au/PANI (polyaniline))
  - Metal Oxide/Organic (SiO_2/PMMA (poly(methyl methacrylate)))
  - Metal Salt/Organic ($CaCO_3$/PANI)

2.7.2 Synthesis

Core - shell nanoparticle synthesis can mainly be divided into two approaches: *a*) Top-down and *b*) Bottom-up. The former uses microfabrication techniques to cut and shape where externally controlled tools are employed. Most commonly used techniques are lithographic such as electron or ion beam, optical near field etc. The bottom-up approach utilizes the chemical properties of the molecules. There are many bottom-up approaches namely chemical synthesis, chemical vapour deposition, laser induced assembly, colloidal aggregation, film deposition and growth (130; 131; 132). Bottom-up approach is advantageous when synthesising smaller sized particles. It also provided much more control over the size of the particle. However, to maintain a precise constant thickness of shell around the core nanoparticle top-down approach is preferred. None of the method is considered superior, each has their own advantageous and disadvantageous.

2.7.2.1 Inorganic Nanoparticle Synthesis

1. Metallic Nanoparticle

1a. Reduction by Sodium Borohydride and Hydrazine

Sodium borohydride was discovered by Schlesinger in 1942 (133). Due to its low equivalent weight of 4.73 g mol^{-1} where each mol provides eight electrons to the reaction and high reducing power of -1.24 V can reduce metallic salts in any medium at any pH. Under a pH condition of < 9.42, in the chemical reaction the metallic salt is reduced to metallic ion and hydrogen gas. The overall reaction involves reduction and hydrolysis of borohydride (134).

$$BH_4^- + xM^{2+} + 3H_2O = H_3BO_3 + xM + (4-x)H_2 + (2x-1)H^+ \tag{2.20}$$

Similarly hydrazine is a comparatively weaker reducing agent but is often used having a reducing power of -1.23 in basic medium. Reaction involving Nickel salt by hydrazine at pH > 11 can be written as (135),

$$2Ni^{2+} + N_2H_2 + 5OH^- = 2Ni + N_2 + 4H_2O \tag{2.21}$$

1b. Transmetalation

Metallic nanoparticle can also be synthesised by redox - Transmetalation reaction. Initially, the core is prepared by a reduction process. In absence of any reducing agent another metal salt is added. When the reduced core and metal salt come in contact with each other the salt gets deposited on the surface due to which some portions of the reduced core gets oxidised and a diffused shell is formed around the core nanoparticle. No reducing agent is require, immediate shell formation, self-nucleation and homogeneous growth are namely the advantageous of this method (136).

$$\textbf{Core Reduction:} Ni^{2+} + 2e^{-} = Ni \tag{2.22}$$

$$\textbf{Shell Formation:} 3Ni + 2AuCl_4^{-} = 3Ni^{2+} + 2Au + 8Cl^{-} \tag{2.23}$$

1c. Thermal Decomposition

Organometallic compounds can be thermally decomposed to metals at high temperature in presence of a surfactant. Surfactant molecules acts stabilizing agents. After the metal has been reduced the surfactant can be removed by washing cycles. To reduce the temperature required for the process precursors such as in case of decomposition of $Co_2(CO)$, [bis (salicylidene) cobalt (II)] - oleylamine is used (137). The reduced metal is highly reactive with oxygen and forms a metal oxide shell also instantaneously no additional step is required besides exposure to oxygen.

2. Metal Oxide Nanoparticles

2a. Sol - Gel Method (Stöber Method)

Sol - Gel method can be tracked back to 1880's, it was later modified by Werner Stöber in 1968 (138). The method mainly involves three different approaches,

- Gelation of colloidal powder
- Hydrolysis of metal slats precursors followed by hypercritical drying and
- Hydrolysis of metal salt followed by ageing and drying under ambient temperature.

These approaches can be further divided into six steps (139):

1. Mechanical mixing of the colloidal nanoparticle powder under suitable pH conditions or hydrolysis for metal salts and subsequently condensation.
2. Casting into mould.
3. Gelation, to allow condensed species to get absorbed on the surface of the nanoparticle.
4. Drying the liquid in vacuum.

5. Dehydration and chemical stabilization, during this process metal hydroxide bonds are removed and an ultra-porous solid remains.

6. Densification by heating at high temperatures to increase the density by reducing the internal porosity.

From step four onwards shrinkage and densification occurs due to *a*) Capillary contraction *b*) Condensation *c*) Structural relaxation and *d*) Stirring. For synthesis of silica shell tetraethyl orthosilicate (TEOS) is used.

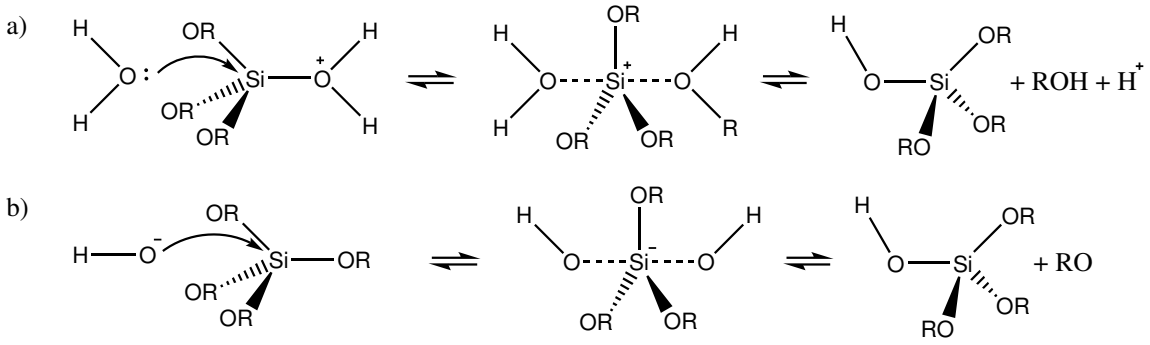

FIGURE 2.14: Hydrolysis of TEOS *a*) Acidic media and *b*) Basic media

2b. Coprecipitation Method

In this method two or more water-soluble metal salts react with each other to form one insoluble metal salt with precipitates at the bottom of the solution. The solubility of salts is an important parameter in such reactions, when the concentration of the products cross the solubility value of the compound the salt begins to precipitate. It follows three step process (140),

- Nucleation
- Growth and
- Agglomeration

The reaction can also be of two types namely a) Redox and b) Acid-Base precipitation. The rate of reaction is faster with lower activation energy. This related to the nucleation process where small particle are formed. When they cross the critical radius they start to grow and a new solid - liquid interface is generated. If the solubility is low the nucleation reaction is faster and growth can be controlled by controlling the rate of reaction or controlling the diffusion rate of molecules (141). Finally, due to Oswald ripening due to reduction in surface area as the particles agglomerate the particle proceed towards the desired size.

$$Fe(HO)_2 + Fe(OH)_3 = Fe_3O_4 + 4H_2O \tag{2.24}$$

2.7.2.2 Organic Nanoparticle Synthesis

Generally organic polymer cores are synthesised using emulsion polymerization followed by in - situ coating of the shell. To enhance the coating surfactants are used to modify the surface (142). The polymerization depends on the phase behaviour, it can be divided to four different groups,

- Bulk Polymerization
- Solution Polymerization
- Suspension Polymerization and
- Emulsion Polymerization

Each technique has its own disadvantages and advantages for example in case of bulk polymerization the molecular weight and viscosity keeps increasing as the reaction proceeds and the problem of removing solvent in case of solution polymerization (143). The industrially most commonly used process is emulsion polymerization where monomers are dispersed in water containing surfactants forming and emulsion. It forms a very stable suspension unlike other methods and the rate of heat transfer is very high. The only disadvantage is the presence of surfactant, removal of which completely is a difficult process. All these process might follow either one of the following polymerization mechanism,

- Addition Polymerization

  This kind of mechanism keeps the features of the chain. Polymerization occurs through addition of large number of monomer molecules in a chain reaction in a very short time (144). Initially, the reaction begins with the presence of an initiator which can be a cation or an anion. After which the chain reaction follows. Depending upon the initiator it can be divided into three further parts,

  - Free Radical Polymerization
  - Anion Polymerization and
  - Cation Polymerization

- Step Polymerization

  In this method polymerization occurs in steps. Therefore, it is a much slower process but provides more control over the growth of the polymer chains (143). Initially, the reaction starts with the reaction of functional groups of the monomer. Out of the many condensation, addition, ring opening, amidation and ester interchange reaction any can be used for step polymerization. However, most commonly used is the condensation reaction, it involves removal of water as by-product of the reaction.

$$xHO-R-OH+xHOCO-R'-COOH=HO[-R-OCO-R'-COO-]_xH+(2x-1)H_2O \tag{2.25}$$

2.7.3 Effect of Different Factors on Synthesis

2.7.3.1 Effect of Temperature

Temperature effects the kinetics of the different reaction taking place during the process of nanoparticle synthesis. Temperature is not an important parameter in case of sol-gel or reduction reactions. However, a low temperature is generally preferred, this is mainly to maintain the unsaturated shell formation. High temperature are commonly only used in case of thermal decomposition reactions and for the purpose of calcination to increase the density of the nanoparticles. Temperature although plays an important role during nucleation depending upon the type of reaction endo-thermic or exo-thermic. A high temperature along with endo-thermic reaction increases the rate of reaction. In an endo-thermic reaction the diffusion rate of molecules becomes faster as the temperature increase and opposite is true for exo-thermic reactions. According to Lifshitz - Slyozov - Wagner model (145) the critical volume grows linearly with time and particles decrease in number over time (146; 147). The kinematics can be shown by combination of three different equations *a*) Arrhenius equation for activation energy *b*) Growth Rate Constant and *c*) Stokes-Einstein equation for diffusivity.

$$k_c = Ae^{\frac{-E_a}{RT}} \tag{2.26}$$

$$k_c = \frac{8\gamma DV_M^2 C}{9RT} \tag{2.27}$$

$$D = \frac{k_B T}{6\pi\eta a} \tag{2.28}$$

Where A is constant, k_c is the growth rate, E_a is the activation energy, R is the universal gas constant, T is the temperature (K), γ is the surface energy of the particles (J m^{-2}, V_m is the volume of particles, C is the concentration of particle in the bulk, η is the viscosity of the media (kg m^{-1}s^{-1}) and a is the hydrodynamic radius (nm).

2.7.3.2 Effect of Surface Modifier Concentration

Surface modifiers play and important role in determining the size and morphology of the shell. Ionic surface modifiers can help form a uniform charge on the particle surface which then can reduce the degree of agglomeration (148; 149). The absorption density depends on the concentration of the modifier. The density increases with increase in concentration. Surface modification enhances the possibility of shell formation around the core. Hence, they are important for particle distribution (ionic modifier) and generally for size control.

2.7.3.3 Effect of pH

Effect of pH depends on the type of reaction and mechanisms involved. Reduction and precipitation reaction are the ones which are heavily affected by the pH of the media. For example, in case of redox reaction material with higher reducing power is used to oxidise the compound with lower reducing potential or power. pH is important in controlling the pace of the reaction. Although surface modifiers are the cause of charged surface of nanoparticle but in case of hydrophilic nanoparticles the surface charge is a result of the pH of the media [105]. In case of sol - gel synthesis, for acidic medium alkoxide group is initially protonated and then a lone pair of oxygen becomes attached to the metal. Whereas in case of a basic medium, hydroxyl group attaches to the metal first and one alkoxide group is released by substitution reaction. Hydrolysis is important for sol - gel method where TEOS is used. The rate of hydrolysis is determined by the pH. A neutral pH has the least rate of hydrolysis.

2.7.3.4 Effect of Solvent and Water

Metal alkoxides are soluble in alcohol but not in water. Hence, generally a combination ratio of water and alcohol is used during the synthesis. Generally the solvent is chosen based on the polymer and alkoxide ligand. In case of epoxy acetone is an ideal choice. For the process of hydrolysis water plays an important role. Since for a complete reaction for one mole of alkoxide four moles of water is required. To maintain an optimum reaction rate a proper ratio between alkoxide and water is required. Generally hydrolysis, condensation and aggregation occurs simultaneously and it is difficult to control them individually. Therefore, having optimum stoichiometric ratio between solvent, water, metal alkoxide from the beginning is important.

Chapter 3

Materials and Processing

3.1 Materials

Diglycidyl ether of bisphenol A epoxy resin DER 332 was obtained from Sigma Aldrich (epoxide equivalent molar mass 172-176 g mol^{-1}) and the amine hardener, Jeffamine D-230 was obtained from Huntsman (Hydrogen equivalent mass of 60 g mol^{-1}). A theoretically ideal stoichiometry was maintained throughout the process, namely 1000:344 parts (resin: hardener), to maintain complete reaction between the epoxide group and the amine group of the hardener. Silica (SiO_2) nanoparticles with a specific surface area of 590-690 m^2 g^{-1} equating to a of size 5-20 nm along with alumina (Al_2O_3) nanoparticles of size less than 50 nm and specific surface area greater than 40 m^2 g^{-1} were also obtained from Sigma Aldrich. Titanium oxide (TiO_2) rutile nanoparticles of size 10-30 nm were obtained from SkySpring Nanomaterial, Inc. Quoted data is taken from the datasheets provided by the relevant suppliers. The chemicals used to produce SiO_2 shells upon the above Al_2O_3 and TiO_2 nanoparticle cores and hollow silica (h-SiO_2), namely tetraethyl orthosilicate (≥ 90%) (TEOS), aluminium isopropoxide (99.99%) poly (vinyl-pyrrolidone), hexadecyltrimethyl-ammonium bromide (CTAB), ammonium oxide and poly (acrylic acid sodium salt) (PAA) M.W. ≃ 5100), were obtained from Sigma Aldrich.

3.2 Sample Preparation

3.2.1 Nanoparticle Synthesis

3.2.1.1 Core-Shell Nanoparticle Synthesis

Core/shell nanoparticles (i.e. TiO_2/SiO_2, Al_2O_3/SiO_2 and SiO_2SiO_2) were synthesised using the Stöber method (138). Initially, 3 g of hexadecyltrimethylammonium bromide (CTAB) was dissolved in 300 ml of deionised water and stirred to form a homogeneous solution. Separately, 2.5 g of TiO_2 was dispersed in 200 ml of deionised water and continuously stirred

for 6 h via. a magnetic stirrer. The resulting TiO_2 dispersion was probe sonicated (UP 200S) for 1 h to break up agglomerates. These two components were then mixed together and stirred for 24 h at 20 °C to ensure complete CTAB film formation on the surface of the nanoparticles. Heraeus ™ Megafuse ™ 8 was then used to remove unabsorbed CTAB by three centrifugation washing cycles with deionised water at 8000 rpm for 10 min. The resulting surface modified TiO_2 nanoparticle were then dispersed in a mixture of 100 ml deionised water and 400 ml ethanol. Further, 5 ml of aqueous ammonia was added and stirred for 2 min, after which, 5 ml of TEOS was added to the solution. This mixture was stirred for 16 h at 20 °C, followed by one centrifugation washing cycle with ethanol and two with deionised water. Finally, the product was vacuum dried at 60 °C for 12 h to obtain core/shell TiO_2/SiO_2 nanoparticles (150). Overall the same process was followed for Al_2O_3/SiO_2 nanoparticle, but polyvinylpyrrolidone (PVP) was used as the surface active agent instead of CTAB.

Mechanism: The Stöber process is a well known example of polymerization of an alkoxide (138). The process involves hydrolysis of tetraethyl orthosilicate (TEOS), as shown in the chemical reaction in Eq 4.1 where R represents the ethyl group.

$$Si(OR)_4 + H_2O \rightarrow HO - Si(OR)_3 + R - OH \tag{3.1}$$

Further, complete hydrolysis results in the formation of silica (SiO_2), Eq 4.2.

$$Si(OR)_4 + 2\,H_2O \rightarrow SiO_2 + 4\,R - OH \tag{3.2}$$

However, the process is chemically is not very straightforward and involves various intermediate polymerization steps. These steps are illustrated in Fig. 2.14. Initially, the hydrolysis of TEOS results in attaching a hydroxyl group to the TEOS monomer followed by condensation. This intermediate reaction results in formation of two partially hydrolysed monomers linked with a siloxane [Si-O-Si] bond. Intermediate species such as [$(OR)_2$-Si-$(OH)_2$] or [$(OR)_3$-Si-(OH)] are formed during partial hydrolysis. Eq 4.3 and 4.4 show the chemical reaction leading to formation of these species.

$$(OR)_3 - Si - OH + HO - Si - (OR)_3 \rightarrow [(OR)_3Si - O - Si(OR)_3] + H - O - H \tag{3.3}$$

$$(OR)_3 - Si - OR + HO - Si - (OR)_3 \rightarrow [(OR)_3Si - O - Si(OR)_3] + R - OH \tag{3.4}$$

As the process of polymerization continues forming a larger macromolecule. When the hydrolysis is completed it results in formation of fully hydrolysed monomer $Si(OH)_4$ which is tetrafunctional. This upon condensation and removal of a water molecule it results in formation of SiO_2. In presence of another externally added metal oxide such as TiO_2, Al_2O_3 and SiO_2 nanoparticles along with a nucleating agent such as ammonia or ammonium hydroxide instead of precipitating at the bottom of the container, start depositing on the surface of these externally added metal oxides forming a shell. However, during this process it is likely that the hydrolysed monomer $Si(OH)_4$, also knows as silicic acid, gets deposited

on the metal oxide surface before condensing and forming SiO_2. Silicic acid due to high negative charge density on oxygen atom is usually very weak and can only exist in aqueous environment via a constant process of hydrolysis and condensation, maintaining a stable equilibrium. After washing the sample and letting it dry at room temperature the water content reduces and the equilibrium can no longer be maintained leading to self condensation. However, it is important to treat the sample under high heat for complete condensation and to remove an residual surfactant. This also increases the density of the shell and avoids pore formation in the SiO_2 network due to residual unbounded silicic acid.

3.2.1.2 Hollow Silica Nanoparticle Synthesis

The hollow silica (h-SiO_2) nanoparticles were synthesized according to the literature (151; 152). Specifically, 0.09 g of PAA-Na powder (molecular weight $\simeq$ 5100 g mol^{-1}) and 25% ammonia solution were mixed using a magnetic stirrer until completely dissolved. 30 ml of ethanol was then added to the solution and stirred for 2 h. Further, 0.15 ml of TEOS was added followed by stirring for a total reaction time of 16 h. The suspensions were then washed with ethanol and deionized water, centrifuged and dried at 60 °C for 12 h to obtain h-SiO_2 nanoparticles.

3.2.2 Size of Nanoparticles

The size of nanoparticles was calculated by using ImageJ. ImageJ is a Java based image processing program developed at National Institutes of Health and the Laboratory for Optical and Computational Instrumentation (LOIC) at University of Wisconsin. It has built-in image acquisition, processing and analysis tools along with additional supporting plugins. TEM images can be extensively processed for variety of different parameters such as particle size, shape, depth, degree of dispersion etc.

The procedure to analyse particle size was as follows, illustrated with an example of Al_2O_3 nanoparticles:

1. The images were initially imported into the software and converted to 8-bit images for processing from 32-bit.
2. Excessive space was removed and a global scale for all the images was set (Fig 3.1).
3. Band pass filter was used to filter the images to get well defined boundaries of the nanoparticle.
4. The images were further sharpened to get more accurate boundaries.
5. The level of brightness and contrast was then adjusted. Noise level was reduced and any shadow formation was removed (Fig 3.2).

6. The threshold of the nanoparticles was then set by defining the overlapping and contact boundary conditions (Fig 3.3).

7. Finally, after clearly recognisable particle boundaries were set, particle analysis is performed which generates a summary of requested parameters (Fig 3.4).

Ten different images were used to obtain the particle size information for each nanoparticle type and their respective histograms were plotted. Following this, a Gaussian fit function was used alongside the histogram to calculate the average and the range of particle size.

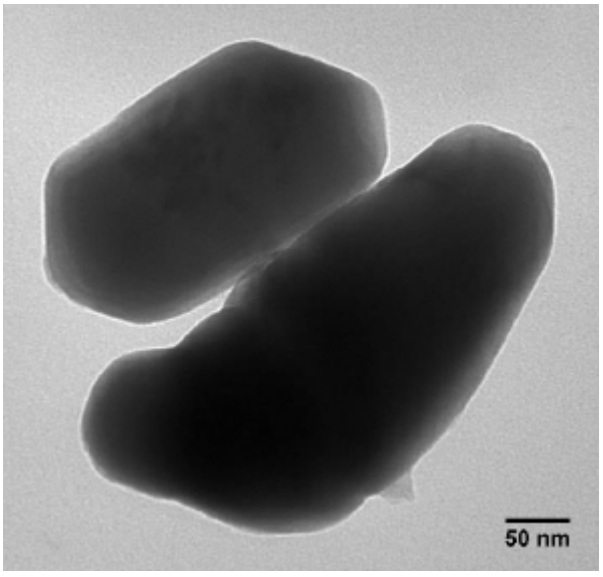

FIGURE 3.1: TEM image of Al_2O_3 nanoparticles after converting to 8-bit and removing excessive space.

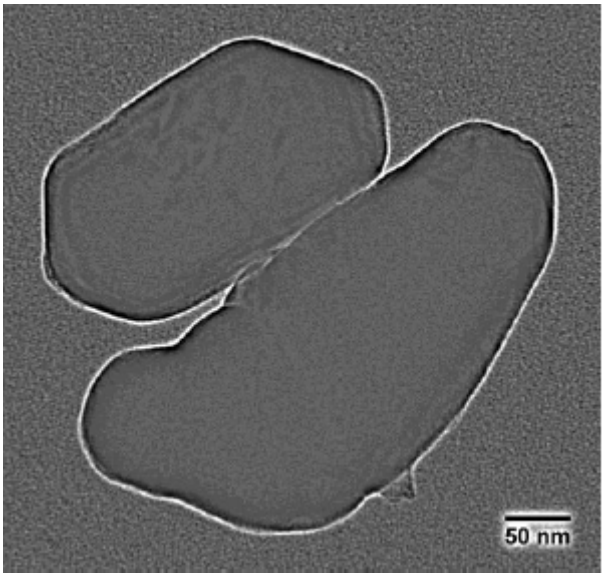

FIGURE 3.2: TEM image of Al_2O_3 nanoparticles after noise reduction and filtering through band pass filter.

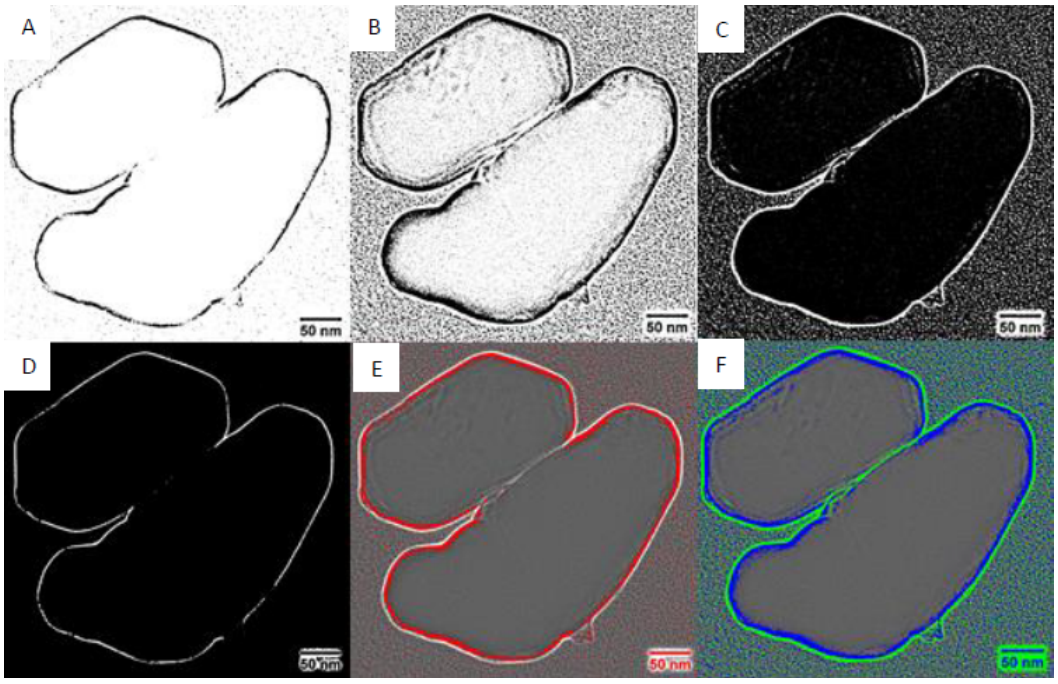

FIGURE 3.3: Levels of setting the threshold for the best boundary conditions of the nanoparticles. **A:** Defining initial boundary of the nanoparticles. **B:** Adjusting the conditions to highlight area of nanoparticles. **C:** Improving the boundary conditions to define the overlapping boundary. **D:** Clearly shown area with overlapping boundaries. **E:** Defining the non-overlapping area and **F:** Using above and under threshold to define the overlapped area (**Blue-Green boundary:** Non-overlapping area and **Green boundary:** Overlapping area).

FIGURE 3.4: Final well defined boundaries of the nanoparticles.

3.2.3 Sample Fabrication

One of the primary focus of the study is to investigate the surface characteristics of the nanoparticle, understand their influence on molecular dynamics of the polymer matrix and

investigate the role of particle interphase. The entire volume of the nanoparticle does not interact with the polymer matrix. Filling by maintaining similar volume percentages allows for a conventional well understood method to be utilised. Nevertheless, does not present a effective way of comparing different nanoparticles. Therefore, it is crucial to maintain same surface area for all the different type of nanoparticles for a given percentage to enable effective comparison. The surface area in case of core-shell nanoparticles refers to the surface area of the outer shell (SiO_2). The specific surface area of all the nanoparticles was calculated using ImageJ based on transmission electron microscopy (TEM) graphs and dynamic light scattering measurements for size distribution. Initially, the three weight percentages for TiO_2/SiO_2 nanoparticle were selected i.e. 1%, 5% and 10%. Based on the weight required for these percentages, the surface areas were calculated. Finally, knowing the surface area of different types of nanoparticle i.e. TiO_2, SiO_2, Al_2O_3, Al_2O_3/SiO_2, SiO_2/SiO_2 and h-SiO_2 from their size and density measurements, to obtain the filler loading ratio for all the other nanoparticle types the weight was calculated based on these surface areas relative to TiO_2/SiO_2.

The above mentioned approach for loading epoxy nanocomposites was used rather then the more conventional weight or volume percentage loading to avoid large discrepancies in the surface area. However, it does not take agglomerate formation into account and surface area based weight calculations are purely theoretical. Depending upon the shape, size and zeta potential characteristics of the different nanoparticle the degree of agglomeration will also vary. Nevertheless, since the shape of all the nanoparticle type is spherical and having the same shell material i.e. SiO_2 for all nanoparticle type could potentially suppress any extreme variation in the degree of agglomeration.

Table 3.1 presents the amount of nanoparticle required for each nanoparticle type based on their density and size to maintain comparable surface area for each percentage relative to TiO_2/SiO_2. It can also be observed that the respective volume percentage do not correlate to the surface area or follow a specific pattern. Therefore, instead of surface area if the volume percentage was maintained constant across different samples the interfacial area between the nanoparticle and polymer would be significantly different. Table 3.2 presents the density and size of each nanoparticle type.

Prior to the sample making process, the resin was heated at 50 °C for at least 1 h to reduce its viscosity and to ensure that the epoxy resin was not solidified thus, appearing completely transparent. Two different preparation method were used: a solvent method and a shear force mixer method.

For the solvent method, the organic solvent used was acetone. 5.2 g of epoxy was dispersed in 100 ml of acetone using a magnetic stirrer for 1 h. Separately, the nanoparticles were dispersed in acetone with the ratio of 5 mg per ml followed by stirring for 2 h. The nanoparticle suspension was then probe sonicated with at amplitude of $0.8 \times S_{max}$ (125 watts) and 0.5 cycle sec^{-1} for 60 min. The two solutions were then mixed and stirred for 2 h,

Nano-Powder	wt. (%)	wt (mg)	vol. (%)	Surface Area (m^2)	Density ($g\,cm^{-3}$)
TiO_2 - 1	0.23	16.00	0.07	1.16	1.10
TiO_2 - 5	1.15	80	0.36	5.82	1.10
TiO_2 - 10	2.30	160.00	0.71	11.60	1.11
TiO_2/SiO_2 - 1	1	70	0.26	1.16	1.10
TiO_2/SiO_2 - 5	5	350	1.29	5.82	1.13
TiO_2/SiO_2 - 10	10	700	2.54	11.6	1.17
SiO_2 - 1	0.03	2.98	0.02	1.16	1.09
SiO_2 - 5	0.15	14.9	0.12	5.82	1.10
SiO_2 - 10	0.30	29.8	0.24	11.6	1.10
SiO_2/SiO_2 - 1	0.20	14.21	0.11	1.16	1.10
SiO_2/SiO_2 - 5	1	71.05	0.53	5.82	1.10
SiO_2/SiO_2 - 10	10	142.1	1.05	11.6	1.10
Al_2O_3 - 1	0.55	38.5	0.15	1.16	1.10
Al_2O_3 - 5	2.75	195.5	0.76	5.82	1.12
Al_2O_3 - 10	5.5	391	1.50	11.6	1.14
Al_2O_3/SiO_2 - 1	0.81	57	0.22	1.16	1.10
Al_2O_3/SiO_2 - 5	4.00	280	1.05	5.82	1.13
Al_2O_3/SiO_2 - 10	8.10	570	2.11	11.6	1.16
h-SiO_2 - 1	0.21	15.31	0.18	1.16	1.09
h-SiO_2 - 5	1.05	76.5	0.90	5.82	1.10
h-SiO_2 - 10	2.1	153.1	1.78	11.6	1.10

TABLE 3.1: Amount of nanoparticles filled per sample to maintain same surface area for different percentages

Nano-Powder	Density (g/cm^3)	Average Size (nm)
TiO_2	3.5	25
TiO_2/SiO_2	4.2	85
SiO_2	1.92	15
SiO_2/SiO_2	2.1	35
Al_2O_3	4	50
Al_2O_3/SiO_2	4.13	75
h-SiO_2	1.32	60

TABLE 3.2: Density and size of different nanoparticles

before the solvent was removed using a rotary evaporator. The resulting system was then placed in a vacuum oven for 12 h at 20 °C. The polymer nanocomposite was weighed, based on the traces of solvent after evaporation in vacuum the nanocomposite were stirred at 50 °C and weight reduction was monitored to ensure complete evaporation of solvent, followed by probe sonication for 10 min. Further, 1.8 g of hardener was then added to the epoxy-nanoparticle mixture and stirred for 20 min. The procedure continued with degassing under vacuum for 20 min. Finally, the mixture was casted into appropriately prepared moulds.

For the shear force mixer method, the nanoparticles filled epoxy resin samples were prepared by first weighing the nanoparticle, resin and hardener. Nanoparticles were then dispersed in 10 ml of acetone and probe sonicated for 30 min with similar settings as in case of solvent method. To this dispersion 5.2 g of resin was added and stirred for 20 min via. a magnetic stirrer. The acetone was removed from the mixture with the help of a hot plate magnetic stirrer operating at 50 °C, weight reduction was monitored to ensure complete evaporation of the solvent. When no further weight reduction was observed, 1.8 g of hardener was added to the system and mixed, using a Speedmixer™ DAC 150.1 FV, at 3,500 rpm for 5 min. The mixture was then degassed for 20 min and cast into moulds.

During the preparation of unfilled epoxy reference sample, the same method was used regardless of absence of filler nanoparticles. This was done to check for any contribution to weight reduction potentially due to evaporation of polymer which could offset the stoichiometric ratio. However, no reduction in the mass was observed. Hence, it was evident that the resin does not evaporate at 50 °C and the weight reduction is only observed due to the evaporation (removal) of the solvent. Also, no significant visible differences or differences in the measured data were observed between the similar samples prepared with these two different methods.

The moulds are made up of steel metallic plates with a Melinex™ spacer of thickness ≃ 200 μm sandwiched between the two plates to determine the thickness of the sample. Prior to assembling the moulds a release agent, Easy-Lease™, was applied to the moulds. In both the methods after casting, the samples were cured at 80 °C for 2 h and then post-cured at 125 °C for 3 h and subsequently left in the oven to cool down in order to have minimalistic thermal history following the manufactures recommendation and in accordance to a study done by Istebreq et al. on effect of curing conditions on epoxy-amine composites (46). The produced samples had a thickness of 200 μm ± 2 μm. The samples were then stored under vacuum inside a desiccator until further use.

Chapter 4

Molecular Dynamics of Epoxy Nanocomposites filled with Core – Shell and Hollow Nano-Silica Architectures

In this chapter the molecular dynamics of epoxy nanocomposites filled with three different types of silica-based nanoparticles with different architectures, namely, solid core, core-shell and hollow and with varying degree of crystallinity were investigated. The samples are characterized by Fourier transform infra-red (FTIR) spectroscopy, differential scanning calorimetry (DSC), broad band dielectric spectroscopy and dynamic mechanical analysis (DMA).

As such, this chapter will aim to answer the following questions:

- Does the structure (tetrahedral or octahedral) or degree of disorder in the structure of shell surface affect the dielectric relaxation behaviour of the nanocomposite?
- How does the absence of a core particle affect the dielectric behaviour of particle-polymer interphase?
- Does the core-shell interface play a role in determining the dielectric properties of the shell-polymer?

4.1 Nanoparticle Characterization

4.1.1 Transmission Electron Microscopy (TEM):

Figure 4.1 shows TEM images obtained for the three different types of nanoparticles, i.e. SiO_2 (Figure 4.1a) and SiO_2-SiO_2 core-shell nanoparticles (Figure 4.1b) and h-SiO_2 hollow nanoparticles (Figure 4.1c). In the case of the SiO_2-SiO_2 core-shell nanoparticles, no clear contrast is evident between the core and the shell, since material is equivalent in both regions. Conversely, in Figure 4.1c, a distinct contrast between the core and the shell can be observed, due to the hollow core, leading to structures composed of a darker circular region surrounding a lighter central core (example arrowed). An example of such a structure but where the formation of the SiO_2 shell appears incomplete, as shown in Figure 4.2. This may be a result of shell collapse due to mechanical weakness (153) or inadequate deposition of SiO_2 on the PAA-Na template. Nevertheless, in this image, three different grey levels are evident corresponding to: the carbon support film (lightest region); the h-SiO_2 shell (darkest, approximately annular region); intermediate grey level, corresponding to transmission via the hollow nanoparticle core and periphery. While the precise details of the contrast will depend the nanoparticle geometry, the general appearance evident in Figures 4.1c and 4.2 is consistent with thickness contrast arising from a hollow structure deposited on a support film.

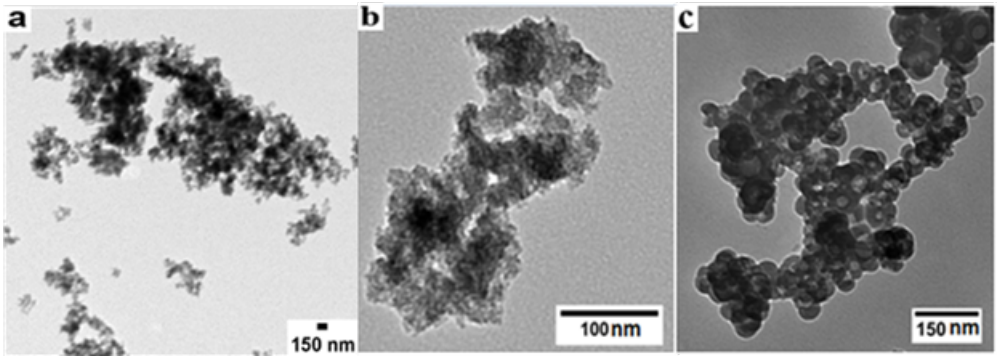

FIGURE 4.1: TEM images of different nanoparticle architecture types a) SiO_2 b) SiO_2-SiO_2 (core-shell) c) h-SiO_2 (hollow)

The median nanoparticle size and their size distribution are presented in Figure 4.3. For SiO_2-SiO_2, the average nanoparticle size is ~35 nm, but with a sizeable fraction of the distribution falling within broader size range of ~25-45 nm, as illustrated in Figure 4.3a. This size variation has been accounted for when calculating the nanoparticle loading level required to maintain a comparable similar interfacial area in all the systems studied. The size of the SiO_2 nanoparticles quoted by the manufacturer is ~5-20 nm, with an average size of ~10 nm, implying that the chemical treatment used to produce the SiO_2-SiO_2 resulted in a shell 20-25 nm in thickness. For h-SiO_2, the average nanoparticle size is ~60 nm, the average pore size is ~30 nm, leading to the conclusion that, in this case, the shell is ~15 nm thick.

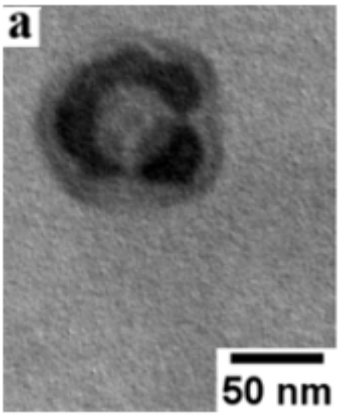

FIGURE 4.2: TEM micrograph showing an isolated h-SiO_2 nanoparticle with an incomplete shell

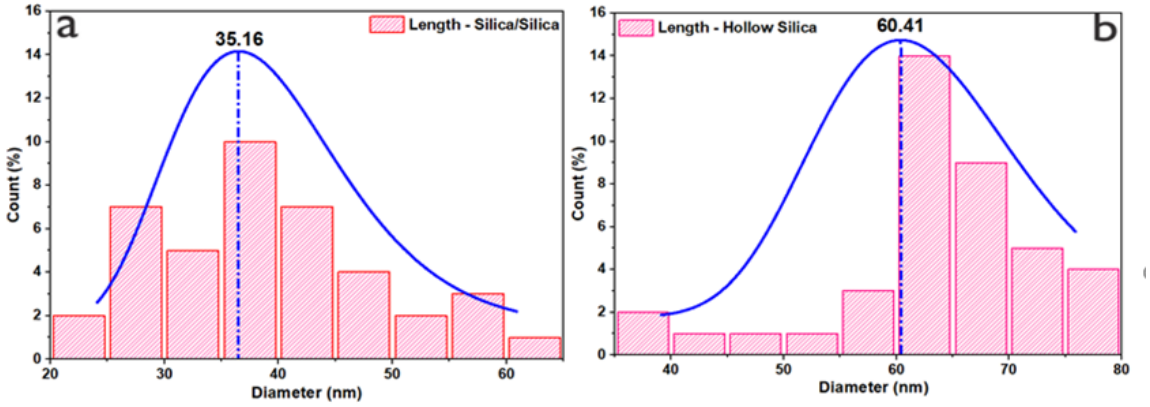

FIGURE 4.3: Illustration of the nanoparticle size distribution number count percentage, distribution curve and the average nanoparticle size, obtained after image analysis of TEM graphs of the two synthesised nanoparticle architecture types i.e. a) SiO_2-SiO_2 (core-shell) b) h-SiO_2 (hollow). Length here represents the diameter of the nanoparticles.

4.1.2 Fourier Transform Infra-red Spectroscopy (FTIR):

In their idealised crystalline form, silica (SiO_2) nanoparticles contain, in terms of mass percentage, 46.63% silicon and 53.33% oxygen (154), arranged with tetrahedral coordination (155). Deviations from this coordination increase the ionic character of the constituent Si-O bonds and lead to micro-structural differences and an amorphous structure (156). Since there are no peaks which can be used as reference; where the concentration of the involved groups is constant across all systems, normalising the FTIR data of the nanoparticles would be complex and inaccurate. Therefore, the data was only baseline corrected. However, acknowledging this, to achieve certain level of comparability between these samples, the amount of nanoparticle by weight homogeneously spread onto the crystal was kept the same at 4 mg. Measured FTIR spectra of the three nanoparticle types measured in their powder form are presented in Figure 4.4; consider, first, the four absorption peaks at 1170 cm^{-1}, 1100-1068 cm^{-1}, 950 cm^{-1} and 800 cm^{-1}, all of which are related to the vibrations of Si-O-Si. The dominant peak spanning 1100 – 1068 cm^{-1} is attributed to the asymmetric stretching (ν_{as}) of the Si-O-Si bonds in the SiO_4 tetrahedron structure in transversal optical

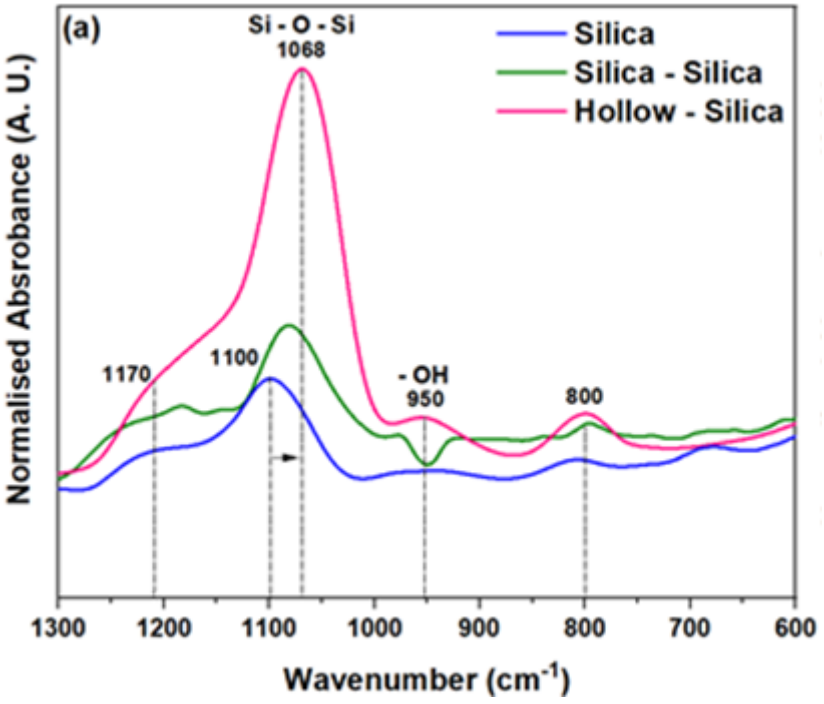

FIGURE 4.4: FTIR spectra of the nanoparticle powders presented for the three different nanoparticle types, namely SiO_2 (core), SiO_2-SiO_2 (core-shell) and h-SiO_2 (hollow) in the 1300 – 600 cm^{-1} wavenumber range

(ν_{as} - TO) mode, while the shoulder at 1170 cm^{-1} arises from asymmetric Si-O-Si bond stretching (Si-O-Si ν_{as} – LO) in the longitudinal optic mode (157). For the same weight of these nanoparticles significant variation in the concentration of the Si - O - Si bonds is observed. From Figure 4.4, it is evident that the position of the TO absorbance peak varies from system-to-system, being located at 1100 cm^{-1} in the core SiO_2 nanoparticles, at 1084 cm^{-1} in the SiO_2-SiO_2 core/shell system and at 1068 cm^{-1} in the h-SiO_2 nanoparticles. Such variations in the position of this spectral peak are a consequence of changes in local ordering and variations in bonding character (158) (159) (160) (161) (162) (163) (164). Specifically, the data presented in Figure 4.4 indicate increased degrees of disorder in the core-shell and hollow nanoparticles compared with core SiO_2 system.

Consider, now, the absorbance around 950 cm^{-1}, which stem from the silanol (Si-OH) groups present in each nanoparticle system (165). From Figure 4.4a, it is observed that absorbance in this spectral region is lowest for SiO_2 and highest for h-SiO_2. However, the concentration of - OH group for SiO_2 - SiO_2 is inconclusive due to the inverted absorbance peak. This inverted peak is still visible after several reruns and is assumed to be the consequence of an equipment error. However, other peaks' reported trends or behaviours are not significantly influenced when similar percentages of error are taken into account. Nevertheless, certain inferences can be drawn by analysing the knows simultaneously to establish a trend. Firstly, SiO_2 has the highest density followed by SiO_2 - SiO_2 and h-SiO_2. Therefore, SiO_2 should ideal have the highest concentration of ordered Si - O - Si bonds. This is further evidenced by the fact that SiO_2 is calcined at 800 °C (as received from the manufacturer) whereas the synthesised nanoparticles were only vacuum dried at 60 °C.

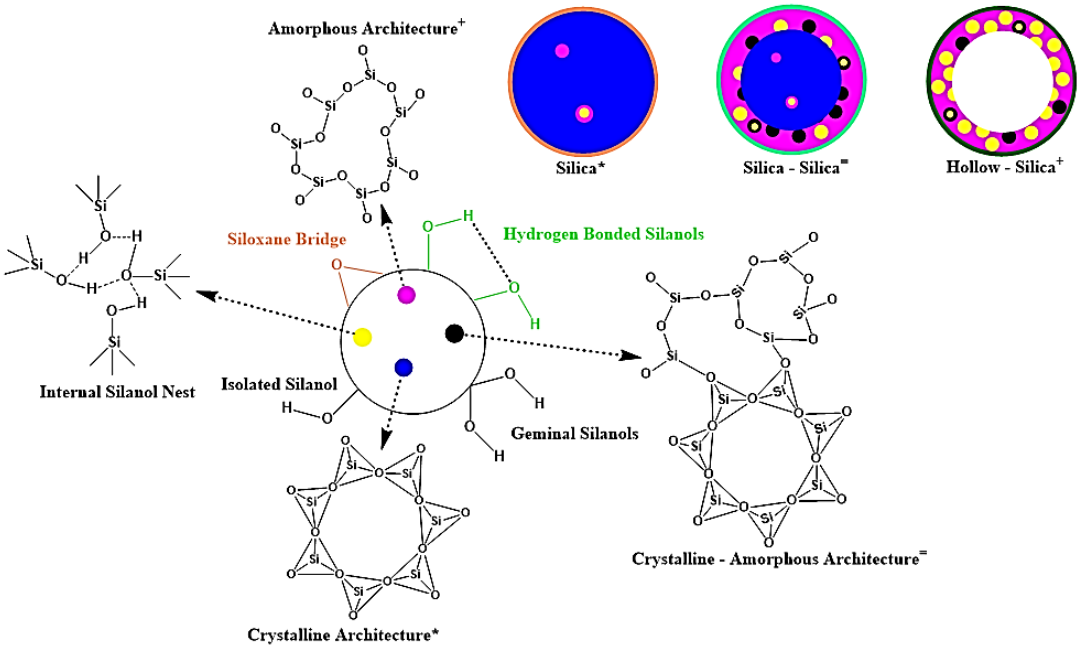

FIGURE 4.5: Illustration of different silanol groups that could be present on the nanoparticle surface i.e. a) Isolated b) Geminal and c) Hydrogen bonded. Due to condensation during calcination these groups form siloxane bridges on the surface of the nanoparticle. Internally, the nanoparticle could be either a) amorphous b) crystalline or c) a combination of both amorphous and crystalline depending upon the heat treatment. Without condensation at high enough temperature not all silicic acid molecules dehydrate and form the networked crystalline structure which introduces defects in form of silanol nests. The diagram of nanoparticle architecture in the top right hand corner approximately represent the concentration and combination of defects along with the varying level of crystallinity of the nanoparticles

Higher temperature treatment leads to further condensation and formation of silanol bridges. Secondly, even though the surface area of the nanoparticles is theoretically the same, the volume is significantly different. Volume of SiO_2 shell in SiO_2-SiO_2 is ~30 mm^3 and for h-SiO_2 is ~49 mm^3. The temperature treatment in both the case is the same. A similar condensation rate would lead to higher concentration of Si – OH bonds remaining in h-SiO_2 as compared to SiO_2-SiO_2 due to this difference in shell volume. It is expected that some of these Si - OH would be present on the internal surface of the h-SiO_2; however, due to a small pore size (30 nm) leading to steric hindrance majority are likely to be either in the volume or on the external surface. Therefore, as compared to SiO_2-SiO_2 is likely that the concentration of Si - OH on the surface of h-SiO_2 is higher. That is, the concentration of silanol groups increases with increasing structural disorder. This suggests that silanol groups are not only present at surfaces, but also within the bulk of the nanoparticles and are related to structural defects, albeit that in the case of the hollow nanoparticles, the additional internal surface are is a further contributory factor. For example, if one Si atom in a tetrahedral SiO_4 unit were missing, then four silanol groups would be required to maintain the stoichiometry, being hydrogen-bonded to form a so-called silanol nest (166). Furthermore, disordered SiO_2 networks may also contain SiO_x-Si-$(OH)_y$ groups, where the sum of x and y is equal to 4 and $x \geq 1$. Such defects have been ascribed to improper

dehydration or the lack of an available adjacent Si bonding site (167),(166). Nevertheless, the previous assertion of increased disorder in the core/shell and hollow nanoparticles is supported by the increased silanol absorption seen in these systems.

The absorbance band intensity is directly proportional to the respective functional group concentration (168). However, h-SiO_2 nanoparticles with the lowest density and the least concentration of Si-O-Si bonds have the strongest absorbance peak; this is attributed to the presence of the mentioned hydrogen bonds. The higher the concentration of these hydroxyl groups (Si-OH), the greater the possibility of forming hydrogen-bonded bridges, leading to noticeable shifts and an increase in the intensity of Si-O-Si absorbance bands. SiO_2-SiO_2 and h-SiO_2 underwent a similar drying procedure, yet h-SiO_2 has a higher hydroxyl group concentration; this is likely due to either lack of higher drying temperature or the additional internal surface area where the surface Si-OH could exist. Hence, h-SiO_2 with the lowest density, highest OH and Si-O-Si (ν_{as} - LO) peak intensities, lowest wave-number peak location for Si-O-Si (ν_{as} - TO) represents a highly amorphous structure and the strongest influence of hydrogen bonding followed by SiO_2-SiO_2. Finally, the absorbance band at 800 cm^{-1} is attributed to the symmetric stretching vibration (ν_s) of Si-O bonds (169). Figure 4.5 gives an approximate visual perception of the different architecture of the nanoparticles, concentration of the silanol nests and the varying crystallinity of the nanoparticles.

4.2 Nanocomposite Characterization

4.2.1 Fourier Transform Infra-red Spectroscopy (FTIR):

FTIR data obtained from the reference unfilled epoxy and related nanocomposites filled with 10 rel. wt.% (11.6 m^2) are presented in Figure 4.6. In these spectra, the absorbance band at 1509 cm^{-1} is attributed to the stretching vibration of aromatic carbons, the concentration of which is known in all samples. As such, this absorbance band was used as an internal calibrant to scale the spectra, as described elsewhere (170),(171). These spectra are consistent with published data obtained from comparable materials whereby the absorbance bands at 3408 cm^{-1} and 1033 cm^{-1} can be attributed to hydroxyl and ether groups (172),(173).

The differences in the intensity of the absorbance band for ether groups are due to the contribution from the Si-O-Si (ν_{as} – TO). Unlike the h-SiO_2-filled epoxy, the Si-O-Si (ν_{as} – TO) does not contribute to the ether absorbance band in the unfilled epoxy sample. Given the constant optimal stoichiometric ratio maintained across all samples, the minimum concentration of ether groups in h-SiO_2 filled sample should be similar to unfilled epoxy, which is not observed. Therefore, the noticeable difference in the intensity could also be due to a difference in ether concentration from changes in curing kinetics (which is not the case with referring to the DSC data below).

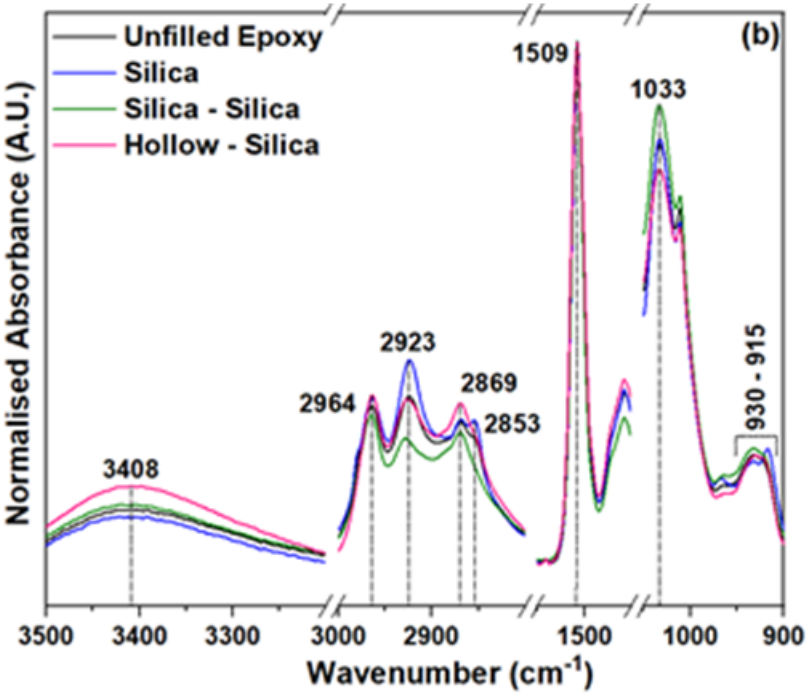

FIGURE 4.6: FTIR spectra of reference unfilled epoxy system along with the epoxy nanocomposite systems, filled with SiO_2, SiO_2-SiO_2 and h-SiO_2 nanoparticles. Illustrating the absorbance peaks in five different regions, i.e. 3500 – 3200 cm^{-1} (hydroxyl), 3000 – 2800 cm^{-1} (hydrocarbon stretching), 1550 – 1450 cm^{-1} (aromatic – calibration peak), 1050 – 1000 cm^{-1} (diethylene ether) and 1000 – 900 cm^{-1} (epoxide ring vibration) starting from high wave-number towards lower.

Noticeably higher intensity of hydroxy ether absorbance band (3408 cm^{-1}) is observed compared to other samples for h-SiO_2 filled sample. Ideally, these hydroxyl groups are produced during the curing reaction (E_{OH}). However, the increase in intensity could also be due to an overlapping band which is attributed to the stretching vibration contributions from the hydroxyl groups (Si-OH) of the silanols (νSi-OH – isolated, terminal and geminal) and their interfacial interactions with the hydroxyl groups of other functional groups (169),(174). νSi-OH was not observed in the spectra of any nano powder. Hence, the absorbance band is most likely originating from the interfacial interaction of Si-OH and E_{OH}. The two absorbance peaks of the hydroxyl groups: one from curing and the other from silanols, cannot be easily de-convoluted without knowing their specific concentration. Therefore, a hard conclusion cannot be drawn. This notion will be further analyzed in the following section in terms of glass transition temperature (T_g).

Even in stoichiometrically balanced systems, about 1 – 2% of epoxides remain unreacted due to steric hindrance (175). The 930 - 915 cm^{-1} absorbance region is attributed to their ring vibrations (176), where no significant changes are observed, which complies with the balanced stoichiometry of those samples.

Significant changes in the intensity of absorbance bands related to the stretching vibrations of CH_3 groups (2964 – ν_{as} and 2869 – ν_s) can also be observed in case of SiO_2 and SiO_2- SiO_2.

Residual TEOS or CTAB as micelles formation could affect their concentration. However, no such peaks were observed in the nano powder spectra neither for CH_2 nor CH_3 (2800 – 3000 cm^{-1}, confirming the complete removal of unreacted TEOS and adsorbed CTAB. Therefore, observed variations are potentially due to the change in the dipole moment of CH_3 of the epoxy resin due to the addition of nanofillers, this requires further investigation in the framework of a separate study.

4.2.2 Differential Scanning Calorimetry (DSC):

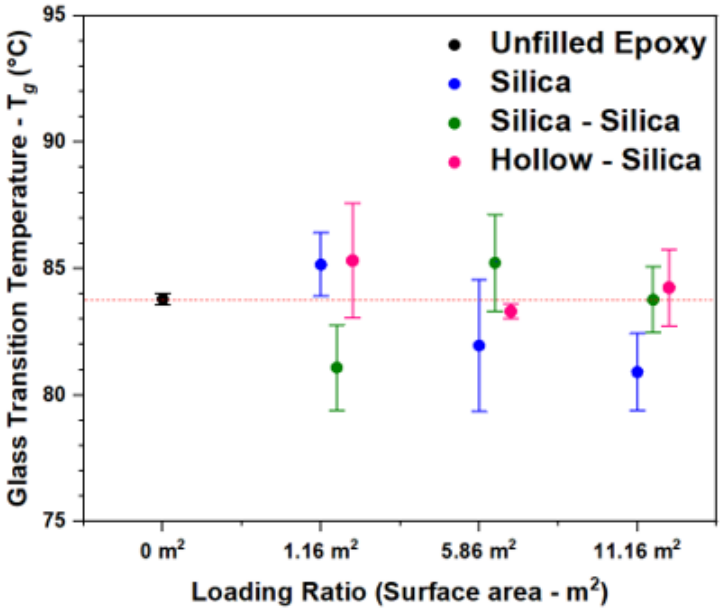

FIGURE 4.7: Glass transition temperature (T_g) of unfilled epoxy along with three different total surface area loading ratio for a) Silica (SiO_2) b) Silica-Silica (SiO_2-SiO_2) and c) Hollow-Silica (h-SiO_2) epoxy nanocomposites

The glass transition is related to long-chain motions of the polymer, a transition from a rigid glassy state to a rubbery state and is commonly related to the dielectric alpha (α) relaxation (177). Figure 4.7 presents DSC T_g values for the unfilled epoxy and epoxy nanocomposite samples filled with three different total surface area-based loading levels, i.e. 1.16 m^2, 5.80 m^2 and 11.6 m^2. The mean T_g of the reference unfilled epoxy is 84 °C, in line with published literature (178). The mean T_g for all the epoxy nanocomposite samples, irrespective of the loading level, lies in the range of 81 – 86 °C. These variations are minor and are commensurate the experimental uncertainties (±2 °C), with the implication that within the composition range considered here, neither the loading level nor the nanoparticle architecture significantly affects the measured T_g. The T_g is a function of many parameters; the degree of cross-linking is one of the parameters which correlates well, in direct proportion (179),(180). As the T_g does not vary between samples, it could be assumed that their degree of cross-linking is also similar. Referring to the FTIR spectra, the increase in hydroxy ether band intensity is therefore justifiably due to the overlapping band and not cause of increased cross-linking.

4.2.3 Broadband Dielectric Spectroscopy (BDS):

Dielectric spectroscopy is a widely used method to study polarization behaviour, molecular dynamics and the effect of the electric stimulus on/off the nanocomposite system. Complex dielectric permittivity can be written as follows: $\varepsilon^* = \varepsilon' - i\varepsilon''$, where ε' is the real part and ε'' represents the imaginary part of the complex permittivity (46). The dielectric spectra generally are a superposition of different relaxation and dispersion phenomena. Under an applied AC field, changes in the polarization behaviour of the system and the composing polar groups alter the ε' and ε'' spectra. These alterations could be associated with different relaxations such as the alpha (α), beta (β), gamma (γ) and interfacial polarization phenomena.

To quantify the relaxation characteristics and study the effect of nanoparticle architecture and concentration on the molecular dynamics of epoxy nanocomposite systems, an empirical Havriliak-Negami (HN) formalism is applied to describe the relaxation processes in the frequency domain; where the complex permittivity is defined as follows (181):

$$\varepsilon^*(f) = \varepsilon_\infty + \frac{\triangle\varepsilon}{[1 + (i\frac{f}{f_{HN}})^{\beta_{HN}}]^{\gamma_{HN}}} \tag{4.1}$$

Havriliak-Negami fitting was selected over other empirical fitting techniques such as Debye, Cole-Cole, and Cole-Davidson as it is considered to be more accurate since it takes into account the fact that the dielectric response of a material is not always a simple power law. Additionally, Havriliak-Negami model can account for the broadening and asymmetry of the dielectric loss spectrum, which is particularly useful for characterizing the properties of materials with a wide range of relaxation times or multiple relaxations which could be either overlapping or segregated. Furthermore, Havriliak-Negami fitting combines the other three methods into one equation (Eq 4.1) for $\beta = 1$ it reduces to the Cole–Cole equation similarly for $\alpha = 1$ reduces to the Cole–Davidson equation; therefore, if an observed relaxation follows specifically any of the three relaxations besides Havriliak-Negami they can still be fitted the same since the β or α parameter would automatically/accordingly be adjusted to 1.

Figure 4.8 shows the variation of ε' and ε'' with respect to temperature at 1 Hz and 10 Hz. These frequencies show all the observed phenomena and relaxations for the reference unfilled epoxy and all the filled samples. These plots give an overview of the following sections where all the phenomena are discussed in detail. As expected, with an increase in the frequency the respective relaxations shift towards higher temperature. The alpha (α), beta (β) and gamma (γ) are common across all the plots in both ε' and ε'', visible distinctly. Similarly, the normal mode (n-mode) relaxation and interfacial polarization phenomena are also observed in all the plots; except in Figure 4.8d where the interfacial polarization peaks has moved out of the measured frequency range (towards higher frequency). The gamma (γ) relaxation can be observed in the ε'' plots towards the lower temperatures (-160 to -130 °C).

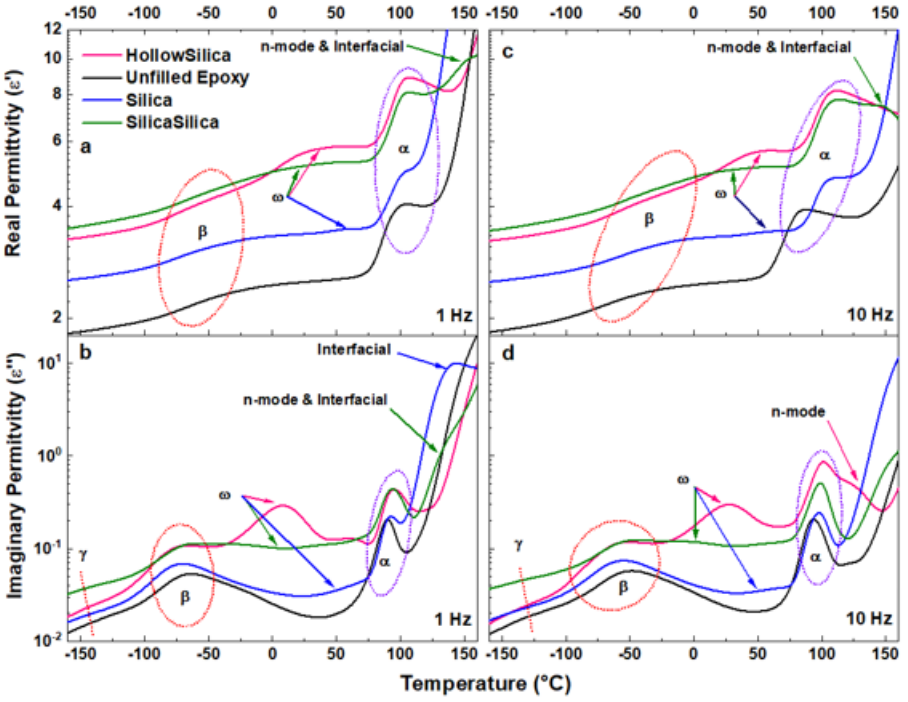

FIGURE 4.8: a) ε' for all epoxy nanocomposite samples at 1 Hz b) ε" for all epoxy nanocomposite samples at 1 Hz c) ε' for all epoxy nanocomposite samples at 10 Hz and d) ε" for all epoxy nanocomposite samples at 10 Hz. The shift of the relaxation peaks to higher temperature can be observed with the increase in frequency

4.2.3.1 Normal mode (n-mode), Interfacial, Alpha (α) and Gamma (γ) Relaxations:

Figure 4.9a illustrates the measured frequency (x-axis) dependence of ε" (y-axis) at 100 °C for the unfilled epoxy system. The measured ε" appears to have considerable contributions from charge transport, where the slope on logarithmic axes is -1 (182). Similar behaviour can be observed for all other systems; the plots are skipped for brevity. In order to separate the dielectric phenomena from the ionic conduction or low-frequency dispersion, a first-order approximation of the Kramers-Kronig relation was used, described as follows (182):

$$\varepsilon''_{derived} = -\frac{\pi}{2}\frac{\partial \varepsilon'(\omega)}{\partial log\omega} \approx \varepsilon'' \tag{4.2}$$

This formula approximately converts the real part of the permittivity ε' into the imaginary part ε", eliminating the direct current conduction contributions. Figures 4.9a and 4.9b depict the $\varepsilon''_{derived}$ for all the epoxy systems at 100 °C and 160 °C, respectively. These dielectric spectra reveal three relaxation processes: α, n-mode relaxations and interfacial polarization. All these relaxation processes move towards higher frequencies with an increase in temperature.

The α relaxation is associated with the cooperative motions of the polymer backbone (183) and is distinctly observed at 100 °C in all the samples at similar frequencies. As expected, no significant changes are observed in terms of α; as mentioned earlier, no T_g variations were observed.

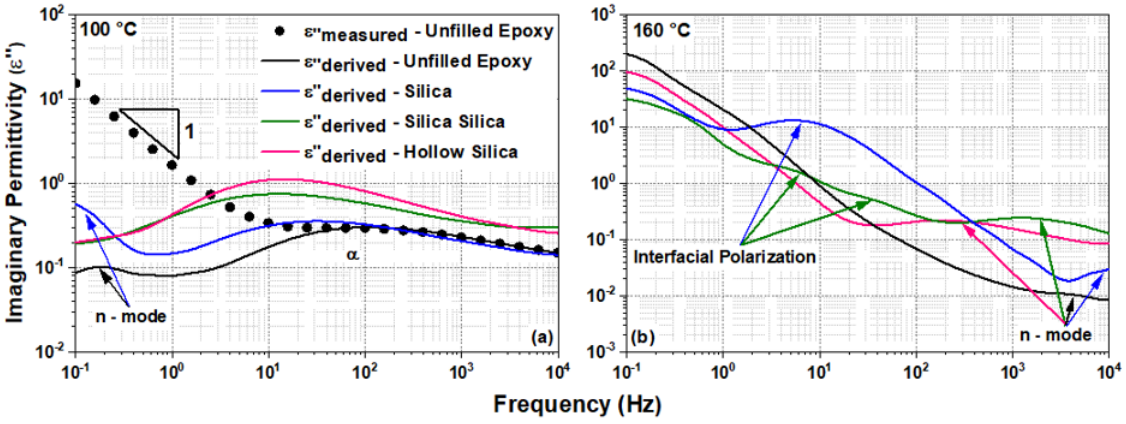

FIGURE 4.9: ε" (measured – unfilled epoxy) and ε" (derived) dielectric spectra for all the epoxy nanocomposite systems at a) 100 °C presenting the α relaxation and b) 160 °C presenting the n- mode relaxation and interfacial polarization phenomena

An additional low-frequency process is observed at lower frequencies (unfilled epoxy and SiO_2); this process is associated with the normal mode relaxation process and is attributed to the long-range end-to-end dipole vector along the polymer chain (182) 1982. The n-mode is observed in all samples at 160 °C. Finally, another low-frequency relaxation process enters the observed window at 160 °C and is likely attributed to interfacial polarization phenomena [12,52]. A distinct additional interfacial relaxation peak is observed in the SiO_2 filled system which is not observed in the sample filled with h-SiO_2. Two additional interfacial polarization peaks are observed in the case of SiO_2-SiO_2 filled systems, potentially originating from the polymer-shell interface at higher frequency and core (crystalline) - shell (amorphous) interface at low-frequency. At temperatures above 120 °C additional features are observed, which may be due to the electrode polarization (182).

The HN deconvolution of the n-mode and interfacial peaks could not be accurately performed to attain any meaningful data as the permittivity of the fillers (3.8 – 4.2) and that of the host (3.8 – 4.0) are similar, resulting in closely overlapping peaks. In order to investigate these features, different nano-fillers with significant permittivity difference with respect to unfilled epoxy will be studied.

Figure 4.10a shows the ε" data acquired at -130 °C, presenting the γ relaxation (54). Deconvolution of the spectra at -150 °C reveals two γ peaks in all samples, namely γ_1 at lower frequencies and γ_2 at higher frequencies, illustrated only for h-SiO_2 in Figure 4.10b for brevity. In a recent study by Orestis et al. , these two γ peaks are extensively characterised for epoxy resin composites prepared with different stoichiometric ratios of octa-glycidyl POSS co-monomer. γ_1 is attributed to the terminal methylene sequences (184) and γ_2 is assigned to the unreacted terminal epoxide groups (73),(185). Under optimal stoichiometry, the study reported similar behaviour as in the present study for the unfilled epoxy sample.

The dielectric strength ($\triangle\varepsilon$) of the unreacted epoxides in all the filled epoxy nanocomposite systems is approximately the same as examined from the dielectric spectra (0.006±0.002)

with the least in unfilled epoxy (0.0004±0.0001) indicating the highest degree of cross-linking. Therefore, along with the T_g and FTIR results, it is conclusive that the degree of cross-linking in all the nanocomposite systems is the same.

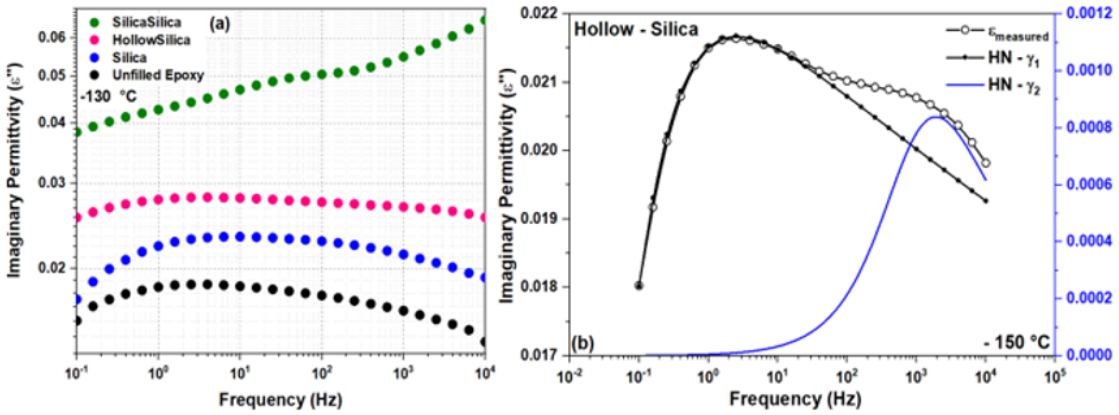

FIGURE 4.10: a) ε" dielectric spectra presenting the γ relaxation for unfilled epoxy, SiO_2 epoxy nanocomposite, SiO_2-SiO_2 epoxy nanocomposite and h-SiO_2 epoxy nanocomposite at a temperature of -130 °C b) De-convoluted HN gamma peaks for h-SiO_2 at -150 °C : γ_1 (at lower frequency) and γ_2 (at higher frequency)

4.2.3.2 Beta (β) and Omega (ω) Relaxations:

Figure 4.11 shows ε" data obtained for all samples between -70 to -30 °C, where β relaxation peak can be observed along with the respective HN fitting. The peak progressively moves to high frequencies with increasing temperature. The β relaxation has been extensively studied after being first reported in 1965 by D. H. Kaelble (186), initially proposed to be originating from transitions of diglycidyl segments (187). Depending upon the structure of theystes, it has also been characterized by features claimed to be attributed to: the rotation of phenyl rings (188); diphenyl propane segments (189); absorbed moisture (190); phase transition of fillers (191),(151); secondary or tertiary amines or increasing molecular lengths (192). Such features are not universally observed owing to the different possible structural configurations. The widely accepted interpretation of its physical mechanism comes from a study by Dammont et al. in 1967 (193), attributing the relaxation to the motion of flexible hydroxyl-ether segments formed during the curing. Since then, this relaxation is commonly associated with the degree of cross-linking. In our previous study we showed that, in anhydride-cured systems, both hydroxyl-ether and ester groups contribute to this relaxation (181).

Figure 4.12 shows the ε" data obtained at 30 °C, where the deconvolution reveals three relaxations, namely β, β' and ω relaxation. In the unfilled epoxy sample, two overlapping relaxation processes are observed, i.e. the onset of β and the β'. Pangrle et al. attributed the β' relaxation to the cross-link junctions (72), such as the diethylene ether polar groups in nodular domains with higher cross-link density. The diethylene ether groups are produced during the curing reaction as part of the etherification reaction (61). Alternatively, a recent

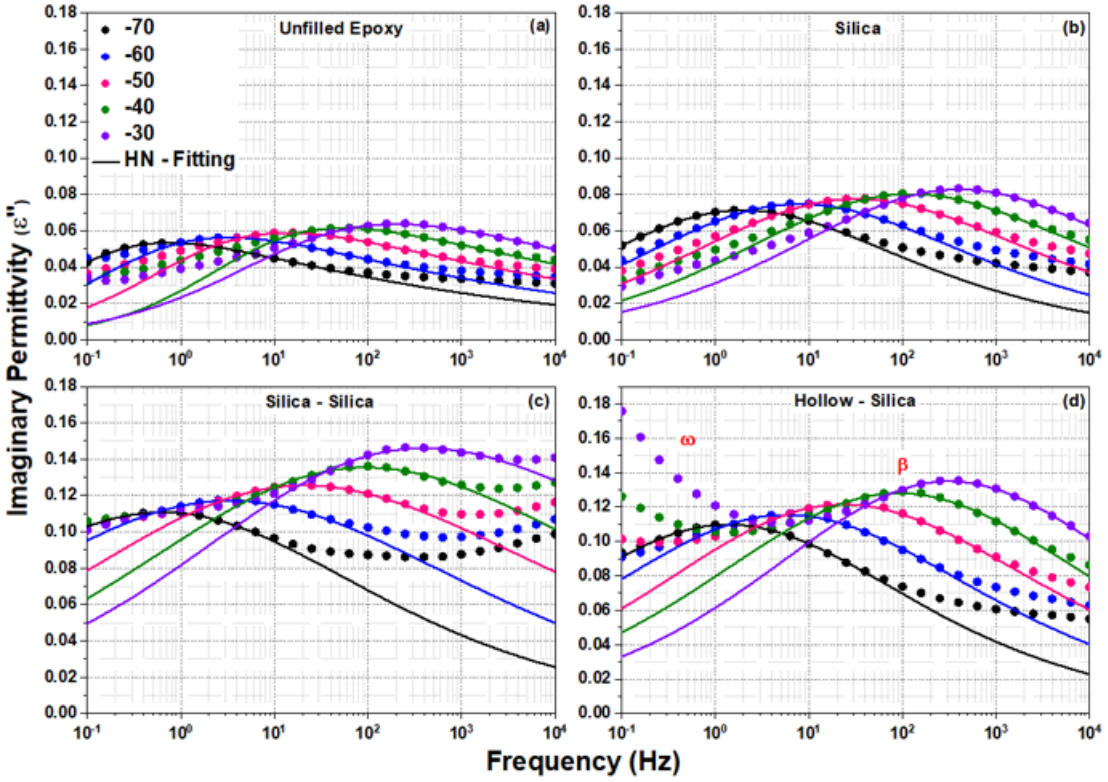

FIGURE 4.11: ε" dielectric spectra presenting the beta (β) relaxation for a) unfilled epoxy b) SiO_2 epoxy nanocomposite c) SiO_2-SiO_2 epoxy nanocomposite and d) h-SiO_2 epoxy nanocomposite for a temperature range of -70 °C to -30 °C along with their corresponding Havriliak-Negami fitting curves

interpretation related such effects to structural alterations caused by the dehydration reaction (during post-curing at elevated temperatures) leading to the formation of C=C backbone bonds (194). Figure 4.13a presents the temperature variation of $\triangle\varepsilon$ for the three relaxations and Figure 4.13b illustrates their corresponding Arrhenius plot and activation energy. The latter could be calculated from the Arrhenius equation as follows:

$$f_{max} = f_0 e^{\frac{E_A}{k_B T}} \tag{4.3}$$

where f_{max} is the peak location, f_0 is the pre-exponential factor, k_B is the Boltzmann constant and E_A is the activation energy of the relaxation.

A similar β' relaxation is observed in SiO_2 filled sample. However, the peak is broader and stronger in $\triangle\varepsilon$. The $\triangle\varepsilon$ describes the temperature-dependent intensity of the relaxation and can be determined by:

$$\triangle\varepsilon = \sum_{i=1}^{k} \frac{1}{\varepsilon_0} g \frac{\mu^2}{k_B T} \frac{N}{V} \tag{4.4}$$

where ε_0 is the permittivity in the vacuum, T is the temperature, μ is the dipole moment, N/V is the number density of the dipoles involved and g is the Kirkwood-Fröhlich factor. The summation is used to determine the total dielectric strength if a number of different types of dipoles contribute to a relaxation process (195). In the SiO_2-SiO_2 filled sample, an

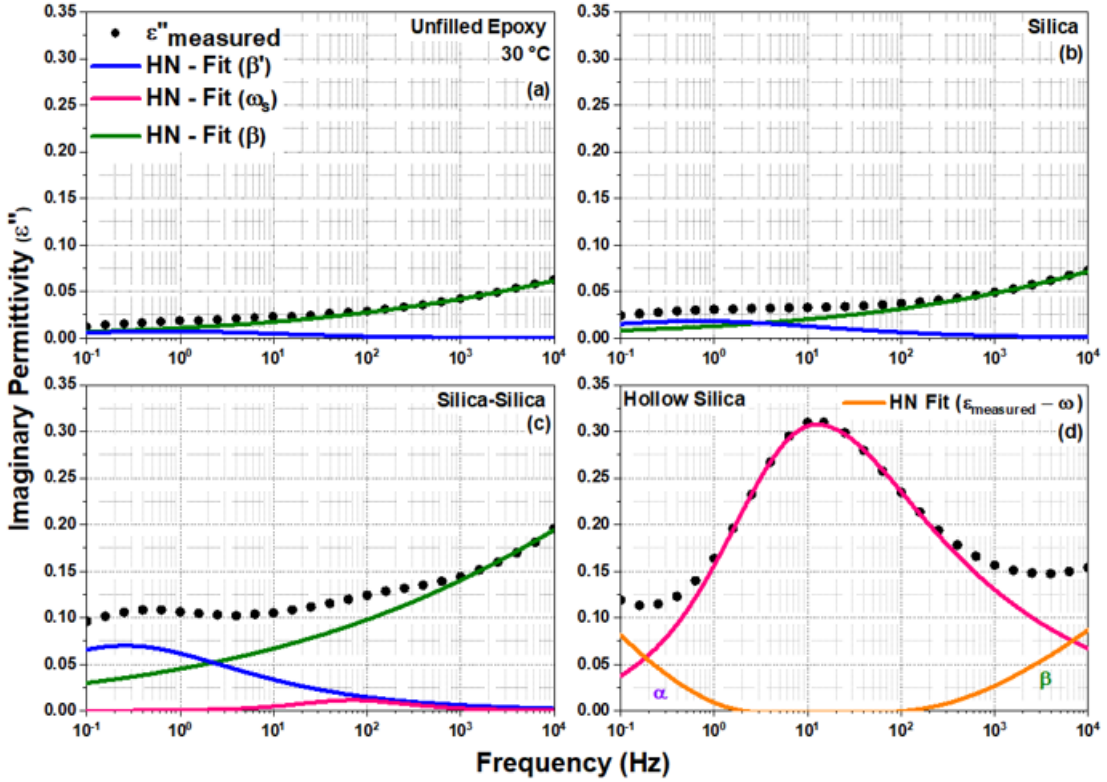

FIGURE 4.12: ε" dielectric spectra presenting the de-convoluted beta (β), beta prime (β'), omega (ω) and alpha (α - if present) relaxation for a) unfilled epoxy b) SiO_2 epoxy nanocomposite c) SiO_2-SiO_2 epoxy nanocomposite and d) h-SiO_2 epoxy nanocomposite for a temperature range of 30 °C along with their corresponding Havriliak-Negami fitting curves

additional peak (ω) is observed at ~10^2 Hz. The strength of the β' relaxation in this system is significantly stronger than SiO_2 filled system. Keenan et al. in 1979 reported a transition dominantly affected by moisture, called ω relaxation (190). Pangrle et al. (72) attributed the origins of a process named β" similar to ω. In contrast to β relaxation, ω relaxation involves the distribution of molecular chain segments and preferential absorption of moisture in low-density cross-link regions as its underlying mechanism. The ω relaxation in the study by Keenan was observed as a relaxation in DMA results, illustrating a bound nature of water molecules with the host polymer. However, such is not the case in our nanocomposite systems and is observed as a polarization phenomenon. This is highlighted by the fact that the ω relaxation peak is observed only in dielectric spectra and not in the DMA results (Figure 4.14b).

In h-SiO_2 filled system, the strength of ω is the strongest, whereas β' is not observed. Here ω is observed to be overlapping with α instead of β' at 10^{-1} Hz. β' shows no correlation with any particular group in this study and appears to be an arbitrary relaxation which might arising as consequence of post curing, as mentioned earlier.

The ω relaxation in this study is observed due to interactions between the nano-fillers and the polymer host in the form of hydrogen bonding between Si_{OH} - E_{OH}, which well with the FTIR results. The degree of cross-linking is the same in all the samples; therefore, the

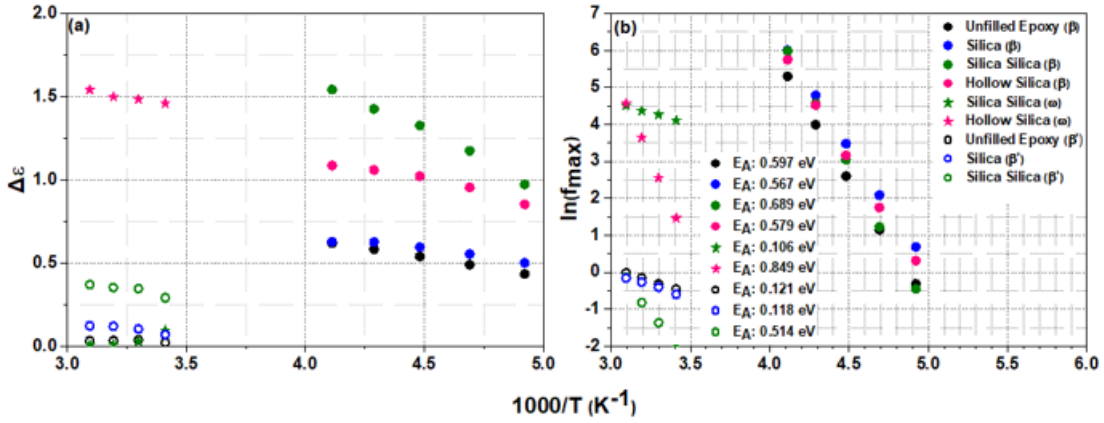

FIGURE 4.13: Dielectric data pertaining to the β, β' and ω relaxations for all the systems: a) temperature variation of $\Delta\varepsilon$ and b) loss peak position as a function of frequency and temperature (Arrhenius plot)

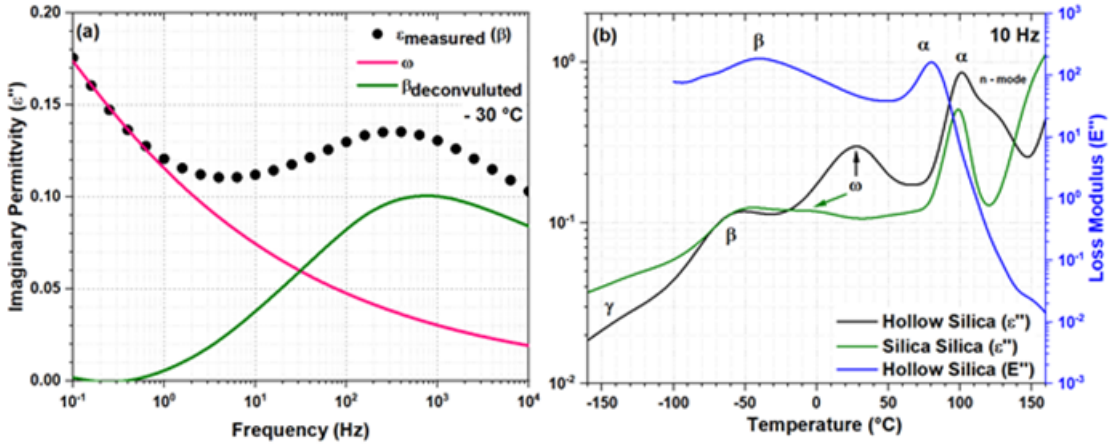

FIGURE 4.14: a) De-convoluted β and ω relaxation peaks illustrating that the strength of the β relaxation is heavily affected by the ω peak in h-SiO_2 and b) Plot for temperature variation of ε" at 10 Hz for h-SiO_2 and SiO_2-SiO_2 illustrating the overlapping and segregated nature of ω relaxation in case of SiO_2-SiO_2 and h-SiO_2 respectively along with a plot of variation of loss modulus with respect to temperature from DMA for h-SiO_2 filled epoxy nanocomposite

concentration of E_{OH} is also the same. Now the $\Delta\varepsilon$ of ω increases with increasing concentration of Si_{OH}. SiO_2 with the lowest concentration has the weakest ω relaxation, which overlaps with β' relaxation. As Si_{OH} concentration increases in the SiO_2-SiO_2 sample, the $\Delta\varepsilon$ of ω relaxation increases and a related peak can be observed distinctly after deconvolution. h-SiO_2 nanoparticles with a completely amorphous structure and the highest concentration of Si_{OH} have the strongest ω relaxation peak. The offset of α and an intense ω relaxation dominate over the substantially weaker β' relaxation in the h-SiO_2 sample. The ω relaxation is segregated from the β relaxation, unlike in the case of SiO_2-SiO_2 where the β, β' and ω are overlapping, presented in Figure 4.12b.

The observed overlapping significantly affects the dielectric strength of the β relaxation. Separation of the ω peak from β in h-SiO_2 also does not necessarily imply that the strength of the β peak is unaffected by it at lower temperatures. Figure 4.14a shows the

deconvolution of the dielectric spectra into β and ω relaxation; this deconvolution is carried out by estimating the HN parameters of ω at -30 °C from the parameters obtained at 10 °C - 50 °C. Such analysis could only be performed at -30 °C, where the β peak is evident and a substantial part of ω onset is observed in the measured frequency range. The true β that emerges is noticeably weaker and has shifted towards higher frequencies. Therefore, the $\triangle\varepsilon$ presented in Figure 4.13a includes the effect of the ω relaxation on β (-90 °C to -30 °C). A shift in the peak position also leads to a significant change in the activation energy, as observed for SiO_2- SiO_2 sample. The ω relaxation in h-SiO_2 is segregated; therefore, its effect on β has reduced. Moreover, the Arrhenius behaviour of β relaxation in the h-SiO_2 sample is parallel to its ω relaxation, which suggests these mechanisms involve a similar dipole type (hydroxyl group).

4.3 Summary

Three types of nanocomposites with different silica architectures, i.e. nano-scale SiO_2, SiO_2-SiO_2 (core shell-structures) and h-SiO_2 (hollow structure) were investigated in this study. Significant changes are observed in the temperature range of -90 °C to 50 °C, where the deconvolution reveals three relaxations β, β' and ω. The β relaxation is attributed to the hydroxy ether groups formed during curing, β' is assigned to the structural alterations caused by the dehydration reaction at elevated temperatures leading to the formation of C=C bonds and ω is attributed to the hydrogen bond interaction between the Si-OH groups of the nanoparticles and the hydroxy ether groups of the polymeric chain. The overlapping of the ω with β and β' increases their $\triangle\varepsilon$ and activation energy (-70 to -30 °C), as observed in the SiO_2-SiO_2 sample where the activation energy of β relaxation increases to ~0.68 eV from ~0.58 eV. In the physical sense, the formation of hydrogen bonds increases the amount of energy required to overcome the motion energy barrier. The strength of ω relaxation increases with an increase in Si-OH concentration and also gradually segregates from β. The h-SiO_2 sample with the highest concentration has completely segregated β and ω peaks. As the Si-OH concentration increases with increasing amorphous content, the FTIR absorbance band intensity of Si-O-Si also increases; this is due to the formation of hydrogen bonds resulting in a dipole change. The ω relaxation is not observed in DMA results and only appears in the dielectric spectra, confirming it as a polarization phenomenon. Two interfacial polarization peaks are reported for SiO_2-SiO_2 attributed to be originating from the two interfaces, core-shell and shell polymer.

Chapter 5

Interphasial Dynamics in Epoxy Nanocomposites Filled With Metalloid Oxide and Metal Oxide Based Core-Shell and Hollow Nano-fillers

In this chapter the interphasial dynamics of epoxy nanocomposites filled with metalliod oxide and metal oxide based conventional core-type, core-shell and hollow nano-fillers is investigated. The samples are characterized by Fourier transform infra-red (FTIR) spectroscopy, differential scanning calorimetry (DSC), broad band dielectric spectroscopy and dynamic mechanical analysis (DMA). As such, this chapter will aim to answer the following questions:

- What are the characteristics and origins of the interactions between the polymer and nanoparticles?
- Which out of the core or the shell or both has a significant effect on the dielectric behaviour of the nanocomposite?
- Could the interphase within the nanoparticle have significant contribution towards shell-polymer interphase?

5.1 Fourier Transform Infra Red Spectroscopy

5.1.1 Nanoparticle Powder

Figure 5.1 presents the FTIR spectra for Al_2O_3, Al_2O_3 – SiO_2, TiO_2 and TiO_2 – SiO_2. Since there are no peaks which can be used as reference; where the concentration of the involved groups is constant across all systems, normalising the FTIR data of the nanoparticles would be complex and inaccurate. Therefore, the data was only baseline corrected and the analysis is only used to confirm the successful synthesis of core-shell nanoparticles alongside the TEM analysis.

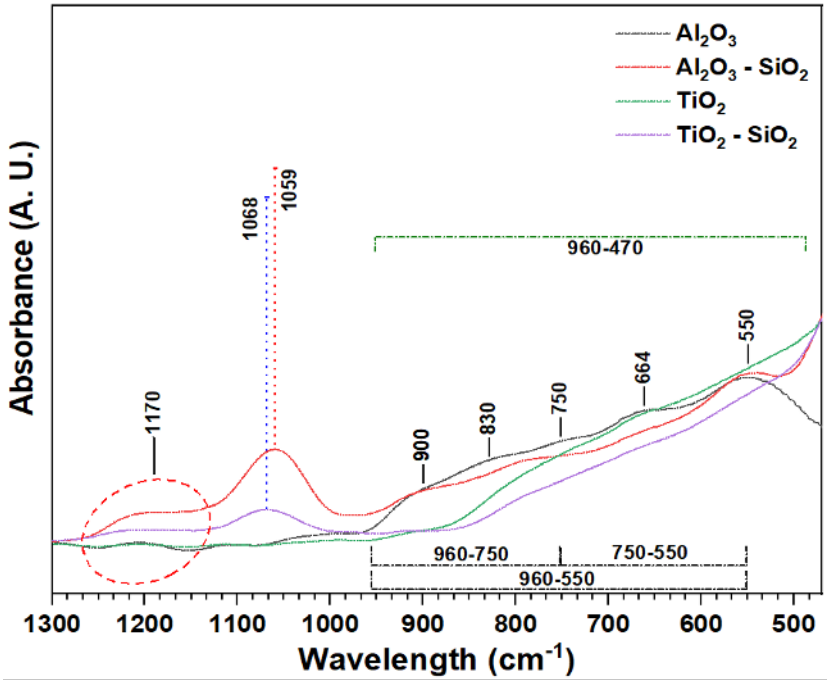

FIGURE 5.1: Fourier Transform Infra-Red Spectroscopy plots of the nanoparticle powder for a)~Al_2O_3 b) Al_2O_3 – SiO_2 c) TiO_2 and d) TiO_2 – SiO_2

Al_2O_3 and Al_2O_3 – SiO_2: One of the key differences between the core type and core-shell type nanoparticles is the absorbance band at ~1170 cm^{-1} which is visible only in case of Al_2O_3 - SiO_2 but is absent for Al_2O_3. The dominant peak spanning 1100 – 1068 cm^{-1} is attributed to the asymmetric stretching (ν_{as}) of the Si–O–Si bonds in the SiO_4 tetrahedron structure in transversal optical (ν_{as} - TO) mode, while the shoulder at ~1170 cm^{-1} arises from asymmetric Si–O–Si bond stretching (Si-O-Si ν_{as} – LO) in the longitudinal optic mode (160). The peak at ~1170 cm^{-1} emphasises the presence of ortho-silicate anions in the SiO_2 shell as a result of synthesis process. A broad characteristic absorbance band of γ-alumina at ~550 - 960 cm^{-1} is observed in both cases. It consists of both tetrahedral and octahedral coordination (196). Peaks in region of ~550 - 750 cm^{-1} are assigned to γ-AlO_6 whereas those in ~750 - 960 cm^{-1} region are assigned to γ-AlO4 consisting of both stretching and bending vibration modes. These regions comprise of various overlapping peaks, the peaks at ~ 664

and 900 cm^{-1} correspond to bending vibration of Al-O-Al and Al-O bonds, respectively. The strong peak at ~ 550 cm^{-1} is attributed to bending vibration of O-Al-O bonds. The absorbance band at ~ 750 cm^{-1} is attributed to the Al-O bonds in a single octahedral layer of γ-Al_2O_3. These layers have considerably higher intercalated hydroxyl groups between them, the absorbance band for these Al-OH bonds is visible at ~ 830 cm^{-1} which appears as a result of δ_s bending vibration of the -OH bond. The absorbance band at ~ 1059 cm^{-1} is attributed to Si-O-Si and Si-O-Al bonds in the γ-Al_2O_3 – SiO_2 nanoparticles.

TiO_2 and TiO_2 – SiO_2: TiO_2 shows a characteristic broad absorbance band between ~ 450 - 960~cm^{-1} with a sharp peak usually occurring between ~ 470 - 450 cm^{-1} which is assigned to the bending vibration of Ti – O bonds (197). Due to the absence of SiO_2 no asymmetric stretching absorbance peak of Si-O-Si and Ti-O-Si bonds between the frequency range of ~ 1200 cm^{-1} and ~ 1000 cm^{-1} is observed in case of TiO_2. Like γ-Al_2O_3 – SiO_2, similar arguments be provided for TiO_2 – SiO_2 and the observed absorbance peak at ~1170 cm^{-1} and ~1059 cm^{-1}.

In both the core-shell nanoparticle types the absorbance peaks for Al – O – Si or Ti – O – Si bonds are observed. Simultaneously, the absorbance peak corresponding to the respective core and shell are also observed. Thus, the formation of core-shell interphase and synthesis of core-shell nanoparticles is evident.

5.1.2 Unfilled and Filled Epoxy Nanocomposites:

Figure 5.2 presents the baseline corrected and normalized FTIR spectra of metal oxide based core-shell nanoparticles filled epoxy nanocomposites, namely, Al_2O_3, Al_2O_3 – SiO_2, TiO_2 and TiO_2 – SiO_2 in three different regions i.e. 3600 – 3100 cm^{-1}: hydroxyl groups, 960 – 900 cm^{-1}: unreacted epoxides and 3000 – 2800 cm^{-1}: symmetric and asymmetric stretching vibrations of hydrocarbon groups, ν_s and ν_{as} of both CH_2 and CH_3. Considering first the 3600 – 3100 cm^{-1} for hydroxyl group region with peak maxima at ~ 3400 cm^{-1}, it can be observed that there is visibly no significant difference in the peak intensity and therefore, the concentration of the hydroxyl groups for unfilled epoxy, Al_2O_3, Al_2O_3 – SiO_2 and TiO_2. The area under the curve (AUC) for all the respective curves was calculated, the values are presented in Table 5.1 Accordingly, the AUC for core-shell samples is noticeably higher as compared to core type or unfilled epoxy sample, implying a higher concentration of – OH groups. In case of TiO_2, the peak appears broader and less intense comparatively. The area under the curve is similar to Al_2O_3 – SiO_2.filled epoxy nanocomposite sample. It is plausible that the concentration of the hydroxyl groups increases for core-shell nanoparticles filled samples due to the additional contribution from the silanols on the surface of the SiO_2 shell. Secondly, in case of TiO_2 – SiO_2 filled sample the surface interaction between the nanoparticles and the polymer has potentially changed significantly leading to a wider range of constrains for the hydroxy-ether and hydroxyl groups. Therefore, the groups activate in a wider range of temperature leading to an increase in the width of the peak.

Sample Name	Area Under Curve (AUC ~A.U.)
Unfilled Epoxy	186
Al_2O_3	186
Al_2O_3 - SiO_2	196
TiO_2	182
TiO_2 - SiO_2	193

TABLE 5.1: Calculated values for the area under the curve in the region of 3600 – 3100 cm^{-1} related to the stretching vibration of the hydroxyl groups for all the samples

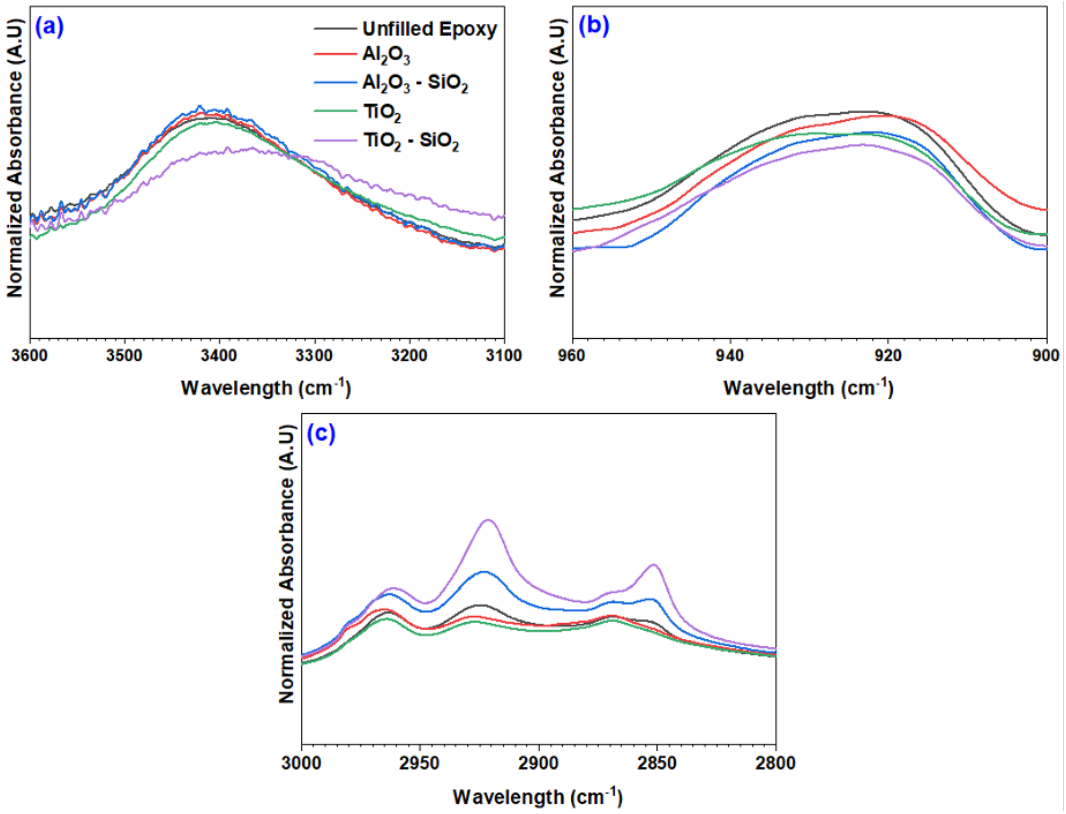

FIGURE 5.2: Fourier Transform Infra-Red Spectroscopy plots of Al_2O_3, Al_2O_3 - SiO_2, TiO_2 and TiO_2 - SiO_2 filled epoxy nanocomposite along with reference unfilled epoxy illustrating absorbance bands for a) hydroxyl groups b) unreacted epoxides and c) hydrocarbon fingerprint region

In the 960 – 900 cm^{-1}, the absorbance peak observed at 932 cm^{-1} is attributed to residual epoxide groups after curing and post curing. There is no significant change observed in the concentration of the unreacted epoxide groups across all samples. The maximum variation is between TiO_2 - SiO_2 and unfilled epoxy which is ~ 2%; the variation is similar to the amount of epoxides which remain unreacted under ideal curing conditions. Finally, considering the 3000 – 2800 cm^{-1} region, unfilled epoxy, Al_2O_3, and TiO_2 do not show a significant change in the intensity of the absorbance band. However, the core-shell structures show a noticeably higher absorbance intensity. No hydrocarbon absorbance peak is observed in case of nanoparticle powder spectra and the stoichiometry is maintained between the resin and hardener across all samples. Therefore, instead of the concentration

of CH_2 and CH_3 affecting the absorbance intensity of the hydrocarbon peaks, the interaction between the shell surface and polymer chains which could lead to a change in charge distribution might potentially be the primary reason for such behaviour.

The SiO_2 shell has Silanols on its surface; similarly, in Figure 5.1 the absorbance band at 830 cm^{-1} demonstrate the presence of Al - OH bonds on the surface of Al_2O_3 nanoparticles. The hydroxyl group of the epoxy resin model as a result of the charge distribution acts as a hydrogen bond donor - acceptor and could potentially interact with the surface silanol groups. In a study by Nakamura et. al. (198) the surface characteristics for SiO_2 and Al_2O_3 filled epoxy nanocomposites were simulated and studied. Between both, Si – OH showed stronger interaction with the epoxy hydroxyl group as compared to Al - OH. Additionally, OH - π interaction between the benzene ring and the surface X - OH (X: Al or Si) were also observed where Si – OH – π interaction were stronger. The benzene rings of the epoxy on the alumina surface appeared to be unable to interact effectively with the protons of the hydroxyl groups on the surface. This was reported to be partly because of the lack of recessed areas of the surface, which are necessary for the benzene rings to take a conformation essential for the OH - π interaction. The absence of dangling protons on the alumina surface was also considered a major factor, where the dangling proton mean a proton that can move flexibly in response to changes in the electrostatic potential and the structure of hydrogen bonds on the surface. Due the octahedral architecture of Al_2O_3 nanoparticles, the surface after cleavage leads to a higher concentration of unsaturated sites resulting in higher concentration of Al – OH bonds. Hence, the distance between the convex oxygen atoms on the surface is majorly either similar to or shorter than typical hydrogen bond distance. Therefore, many of the hydroxyl groups prefer to form hydrogen bonds with the nearby convex oxygen atoms rather than the hydroxy ether group of the epoxy. Unlike Al_2O_3, the tetrahedral geometry of SiO_2 leads both concave and convex silicon sites on silica surface; where the former are hydroxylated and the latter are not. This leads to a reduced concentration of Si – OH. Thus, a higher recessed area is obtained resulting in stronger Si –OH – π and Si – OH – OH interactions. Conclusively, it was reported that the epoxy adheres to the hydrophilic surfaces through the hydrogen bonding interaction due to the hydroxyl group and the dispersion interaction due to the benzene rings. Therefore, in the present study, stronger hydrogen bonding interaction and OH – π interactions of epoxy benzene ring with the silanol groups which results in stabilization of the ring could lead to charge redistribution; in turn affecting the absorbance band intensity of hydrocarbons in the core-shell nanocomposites. Since these interactions are much weaker in core type nanoparticles, no significant changes are observed.

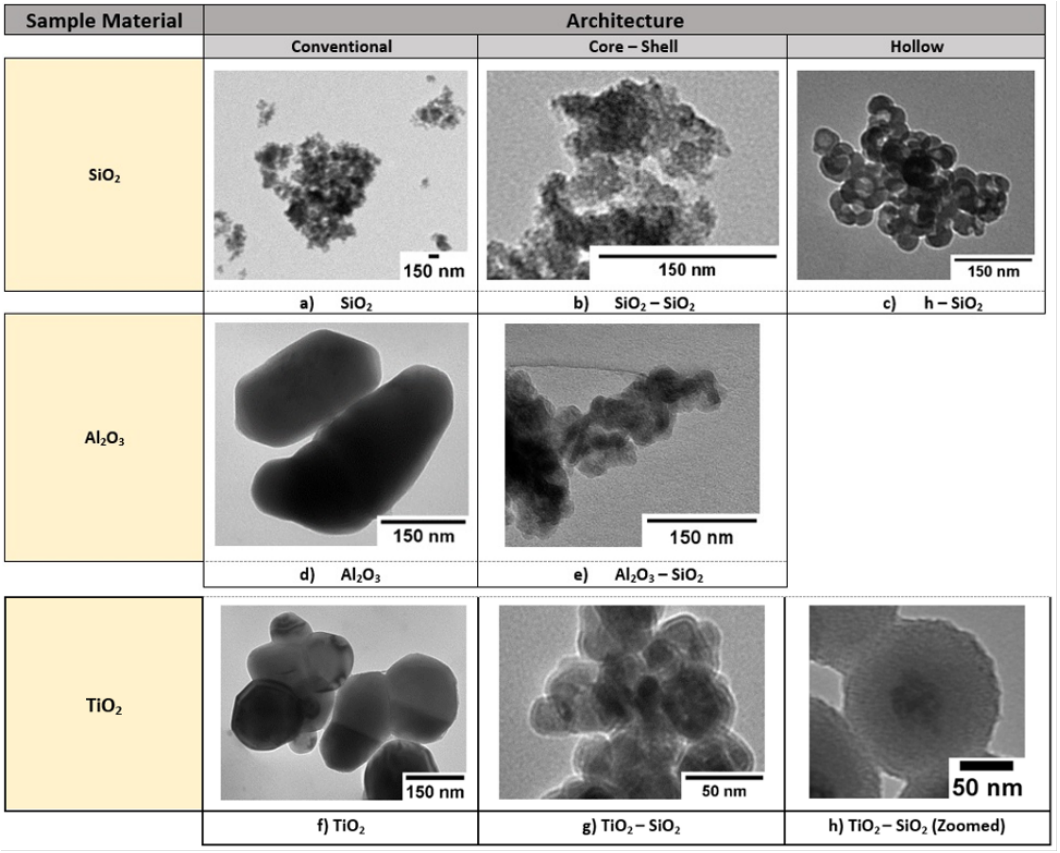

FIGURE 5.3: TEM images of the commercially obtained and laboratory synthesised nanoparticles, segregated based on their architecture and material type a) SiO_2 b) SiO_2-SiO_2 (Core – Shell) c) h-SiO_2 (Hollow Core) d) Al_2O_3 e) Al_2O_3 – SiO_2 (Core – Shell) f) TiO_2 at a scale of 150 nm and g) TiO_2-SiO_2 (Core-Shell) h) TiO_2-SiO_2 – Zoomed at 50 nm.

5.2 Result and Discussion

5.2.1 Transmission Electron Microscopy

The TEM images obtained for the seven different types of nanoparticles, namely SiO_2, SiO_2-SiO_2, h-SiO_2, Al_2O_3, Al_2O_3-SiO_2, TiO_2 and TiO_2-SiO_2 and are shown in Figure 5.3 These illustrations do not represent the median size of the nanoparticles and are simply demonstrative of their successful synthesis. When an electron beam is focused on a sample, areas with higher crystallinity/density look darker in TEM. The concentration of electrons absorbed is directly related to the density of the sample. As a result, as the density increases, fewer and fewer electrons pass through, resulting in a darker shadow.

In the case of SiO_2-SiO_2, the core and shell are made of the same material. The SiO_2 for the core is acquired from a commercial manufacturer whereas the shell is synthesised in the laboratory. Therefore, the differences in their density are not significant. However, noticeable changes in the grey scale around darker regions (white arrow) representing comparatively higher density areas can be observed on closer inspection where the lower density areas (black arrow) represent the amorphous shell formation. Similar features can

be seen in the case of Al_2O_3-SiO_2 and TiO_2-SiO_2 distinctively, demonstrating successful core-shell nanoparticle synthesis. Zoomed in TiO_2-SiO_2 is presented in Figure 5.3h, where a higher density core with darker characteristics and a SiO_2 shell with lighter characteristics is observed and demonstrates successful synthesis of core shell nanoparticles. Since the core in h-SiO_2 is absent, the grey scale of the pore is comparable to that of the grid and is only slightly darker due to the contribution from the shell as it is a 2D depiction of a 3D architecture. The shell, on the other hand, is substantially denser than the carbon-coated grid, and hence appears as a dark band around the central pore.

5.2.2 Dynamic Mechanical Analysis and Differential Scanning Calorimetry

Figure 5.4a presents the DMA – tan δ and E" spectra and BDS – ε'' spectra for reference - unfilled epoxy and SiO_2, SiO_2-SiO_2, h-SiO_2 filled epoxy nanocomposites between the temperature range of -100 °C – 160 °C and -160 °C – 160 °C, respectively at a frequency of 10 Hz. The frequency of 10 Hz was chosen from the five tested frequencies of 10^{-2}, 10^{-1}, 10^{0}, 10^{1} and 10^{2} Hz because it shows all the relaxation processes with the least amount of error from equipment. Two distinct relaxation processes are discernible for all the samples in DMA, one being the primary relaxation phenomenon, denoted as α, and the other being the sub-glassy relaxation process, known as β relaxation. Additionally, another weak relaxation process is observed near the rubbery plateau region which is being attributed to the normal mode relaxation process. Furthermore, besides these relaxations, two additional relaxations are observed in the BDS spectra, namely γ in all the samples and the so-called ω relaxation. Similarly, Figure 5.4b and 5.4c presents the DMA – tan δ and E" spectra and BDS – ε'' spectra for reference - unfilled epoxy and Al_2O_3, Al_2O_3 – SiO_2, TiO_2, TiO_2-SiO_2 filled epoxy nanocomposites. Only conventionally known relaxation are observed.

The origins of the ω relaxation have been linked to the distribution of molecular chain segments and the preferential absorption of moisture in low-density cross-link locations in earlier studies that explored the phenomenon, such as those by Pangrle et al. (194) and Keenan et al. (192). These research noticed the relaxation in DMA thermographs and attributed it to the fact that the water molecules were connected to the host polymer via hydrogen bonds. Furthermore, in our prior study, the dielectric behaviour of relaxation was thoroughly explored and ω relaxation was attributed to hydrogen bonding interactions between the nano-fillers and the polymer host, as opposed to hydrogen bonding with water molecules, which aligns well with our results and measurements from different techniques. However, a similar relaxation peak is not observed in DMA thermographs. Therefore, further analysis was performed to characterize the observed peaks. A Gaussian fit function was used to obtained four different parameters for the two observed relaxations i.e. α and β, namely, glass transition temperature (T_g), peak intensity, peak width (full width at half maxima – FWHM) and the storage modulus (E') at 30 K above T_g.

5.2.3 α relaxation

The α relaxation originates from the macromolecular chain motions, which are frequently linked to the T_g. Except Al_2O_3-SiO_2 filled sample, all other samples have single well-defined α relaxation peak indicating that their respective cross-linked networks have no phase separation. The results obtained for the different features of the peak are presented in Table 5.2 It can be observed from Table 5.2 that besides TiO_2 filled nanocomposite all the other epoxy nanocomposite samples have lower T_g than the reference unfilled epoxy sample. Two key observations from Table 5.2 are:

1. There are no significant changes between the reference unfilled epoxy sample and the core type nanoparticle in terms of the tan δ intensity and width.
2. All the four parameters for SiO_2-SiO_2, Al_2O_3-SiO_2 (II) and TiO_2-SiO_2 nanocomposite samples are noticeably the same.

Sample ID	Peak Number	T_g	Intensity	Width(K)	Storage Modulus (E')
Unfilled Epoxy	I	93.88	0.80	21.16	15.57
SiO_2	I	92.70	0.79	21.64	15.57
SiO_2 - SiO_2	I	91.14	0.73	22.52	15.68
h - SiO_2	I	90.33	1.02	14.67	18.67
Al_2O_3	I	86.17	0.76	21.74	15.44
Al_2O_3 - SiO_2	I	71.48	0.16	15.07	15.47
Al_2O_3 - SiO_2	II	91.32	0.71	22.36	15.47
TiO_2	I	95.34	0.80	21.31	17.27
TiO_2 - SiO_2	I	91.10	0.72	22.24	15.67

TABLE 5.2: Values of different parameters for α relaxation obtained from DMA – tan δ vs. temperature and E' vs. temperature plots. T_g: tan δ peak position, Intensity: tan δ peak maxima, Width: full width at half maxima (FWHM) of tan δ, storage modulus and crosslink density from value of E' at T_g + 30 °C.

There are several factors such as molecular weight, cross-linking density and tactility whose alteration could lead to changes in the T_g. However, the processing method used here to prepare the epoxy nanocomposites filled with different fillers is the same. Hence, it is plausible that the observed changes in the T_g originate from the interaction between the filler and the epoxy matrix. It has been reported that the interfacial layer created between the nano-filler and the polymer due to their interaction plays an important role in determining the T_g of the nanocomposite (199). Depending upon the nature of these interactions the T_g is either reduced, increased, or remains constant resulting from either an attractive, repulsive, or neutral behaviour, respectively. The extend of this behaviour further depends on the type of filler. Here, SiO_2 shows a neutral behaviour, TiO_2 demonstrates an attractive behaviour whereas Al_2O_3 along with all the other nanoparticles shows a repulsive behaviour. The SiO_2 shell deposited on the SiO_2, Al_2O_3 and TiO_2 core nanoparticle template was done using exactly the same sol-gel process and has similar thickness. When a SiO_2

shell is deposited on Al_2O_3 compared to Al_2O_3 the T_g of the nanocomposite increases by ~ 4 K. Similarly, when a SiO_2 shell is deposited on TiO_2 compared to TiO_2 the T_g of the nanocomposite reduces by ~ 4 K Furthermore, both the SiO_2-SiO_2, Al_2O_3-SiO_2 and TiO_2-SiO_2 filled systems have approximately the same T_g; this potentially implies that the interactions between the SiO_2 shell and the polymer might be similar.

Covalent bonds between the filler and the polymer matrix have been reported to noticeably increase the T_g of the sample (200). However, weak attractive bonds such as the hydrogen bond do not significantly affect the T_g of the sample but do add constrains to motion of polymer chains. In a study by Lin et al. (201) two types of SiO_2 nanoparticles i.e. hydrophobic and hydrophilic filled in poly (vinyl acetate) were investigated. In case of hydrophilic-SiO_2, with Si – OH bonds on its surface, hydrogen bond interactions with the carbonyl group of the matrix were observed. Nevertheless, even at a loading ratio of 30 wt%, the T_g remained more or less constant, with a maximum variation of ~ 1 K. Furthermore, Czogala et al. (202) highlighted the significance and role of hydrogen bond formation in plasticizer based polymer composites. These hydrogen bond interactions lead to a change the three-dimensional molecular architecture of polymers with less polymer chain entanglements; thus, improving their mobility as a consequence of reduced initial dipole-induced dipole attractions. Additionally, in accordance to the free volume theory, ability to form hydrogen bonds also translates to good plasticizing efficiency by increasing the free volume of the system providing more space for polymer chains to move. Therefore, the hydrogen bonds themselves do not influence the T_g significantly but the plasticizing effect introduced due to them leads to a reduction in the T_g.

SiO_2 is calcined at 800 °C ideally there are no silanol groups on its surface. As such, there are no hydrogen bond interactions between the polymer and the nanoparticles illustrating no noticeable changes in the measurements when compared to unfilled epoxy. However, SiO_2-SiO_2, Al_2O_3-SiO_2, h-SiO_2 and TiO_2-SiO_2 are vacuum dried at 60 °C; therefore, their respective shells are amorphous. Besides h-SiO_2, regardless of the size of the particles and volume of the shell, the tan δ characteristics are the same for these nanoparticles; where the total surface area, the thickness of the shell and the shell material is the same.

A second peak in tan δ is observed in dynamic mechanical measurements of a wide variety of polymers, including poly (dimethyl siloxane), filled with silica nanoparticles, 50–100 °C above the glass transition, which is attributed to the glass transition of an interfacial polymer layer with restricted mobility by Tsagaropoulos and Eisenberg (203). The findings are explained in terms of a model with three different types of polymer: a bulk polymer unaffected by the particle; a second, loosely bound interfacial layer; and a strongly bound, immobile layer immediately surrounding the particle. The second interfacial layer is reported to be responsible for the second glass transition. The observed decrease in second glass transition intensity with increased silica concentration was reported and explained by this hypothesis. However, in the present study, whilst comparing Al_2O_3-SiO_2 and SiO_2-SiO_2 their concentration has changed but the T_g peak (91.00 °C) intensity remains noticeably the same. Secondly, the tan δ intensity is in comparable ranges to other nanoparticles. Once a

group is activated it ideally would not contribute to the intensity of a relaxation at higher temperatures. Considering these and in accordance to the measurements, the overlapping peak at ~ 71.00 °C could not originate from the mobilization of certain groups on the main chain.

As the size of the nanoparticle increases, the likelihood of two adjacent silanol groups present on the surface increases. With an increase in the size of nanoparticle the recessed area also increases which leads to reduced steric hindrance from the benzene rings for the epoxy hydroxy ether groups to interact with the surface silanols (198). Therefore, Al_2O_3-SiO_2 would have the highest concentration of adjacent double hydrogen bond interactions as illustrated in Figure 5.5 (II) due to its biggest size amongst all nanoparticle types. This could potentially lead to the formation of small regions around the nanoparticle with highly restricted mobility resulting in micro-phase separation (204). As the temperature increases these hydrogen bonds disassociate; hereafter, there is no phase separation within the polymer and the nanocomposite has a single T_g. This behaviour can be observed in case of Al_2O_3-SiO_2, initially, as the temperature increases to ~ 70 °C hydrogen bonds between the polymer chains and the nanoparticles break. A corresponding micro-phase separation peak overlapping with the T_g peak is observed where the disassociation of the hydrogen bonds leads to a higher degree of freedom for the C – H groups; only a tiny proportion of these main chain groups are involved thus resulting in a small peak intensity. The width of this peak is narrow, implying the groups involved are similar, are activated at similar temperatures and therefore, also potentially exist in similar local constrains. Upon further increase in temperature, T_g is reached.

The intensity of the tan δ peak represents the internal friction of the system; it depends on the freedom of movement of the involved groups. With increased crosslinking the intensity of the peak reduces due to the reduction in the avaliable rotational and translational modes of molecular motion (205). It has been experimentally evidenced that the T_g increases with an increase in the crosslink density (ϑ) and the tan δ peak shifts towards higher temperatures. Implying, T_g increases as the intensity of the tan δ peak reduces. The intensity for core-shell type nanoparticle is approximately the same. However, compared to unfilled epoxy sample the intensity has reduced. As expected, FT-IR shows no significant changes in the amount of residual epoxides groups after post curing due to stoichiometric addition of resin and hardener. Therefore, the additional constrains on the molecular motion of the polymer chains should potentially be originating from the polymer-nanoparticle interfacial interaction.

The formation of hydrogen bonds would affect the internal friction of the nanocomposite but only until a certain temperature. At temperatures closer to the T_g majority of the hydrogen bonds between the polymer chains and the nanoparticles would disassociate. However, the silanol groups present on the surface of nanoparticles would still present steric hindrance to the polymer chains in the immediate vicinity of these particles. Thus, the additional steric hindrance could potentially reduce the internal friction leading to a reduced intensity of tan δ. Furthermore, multiple models have been developed and

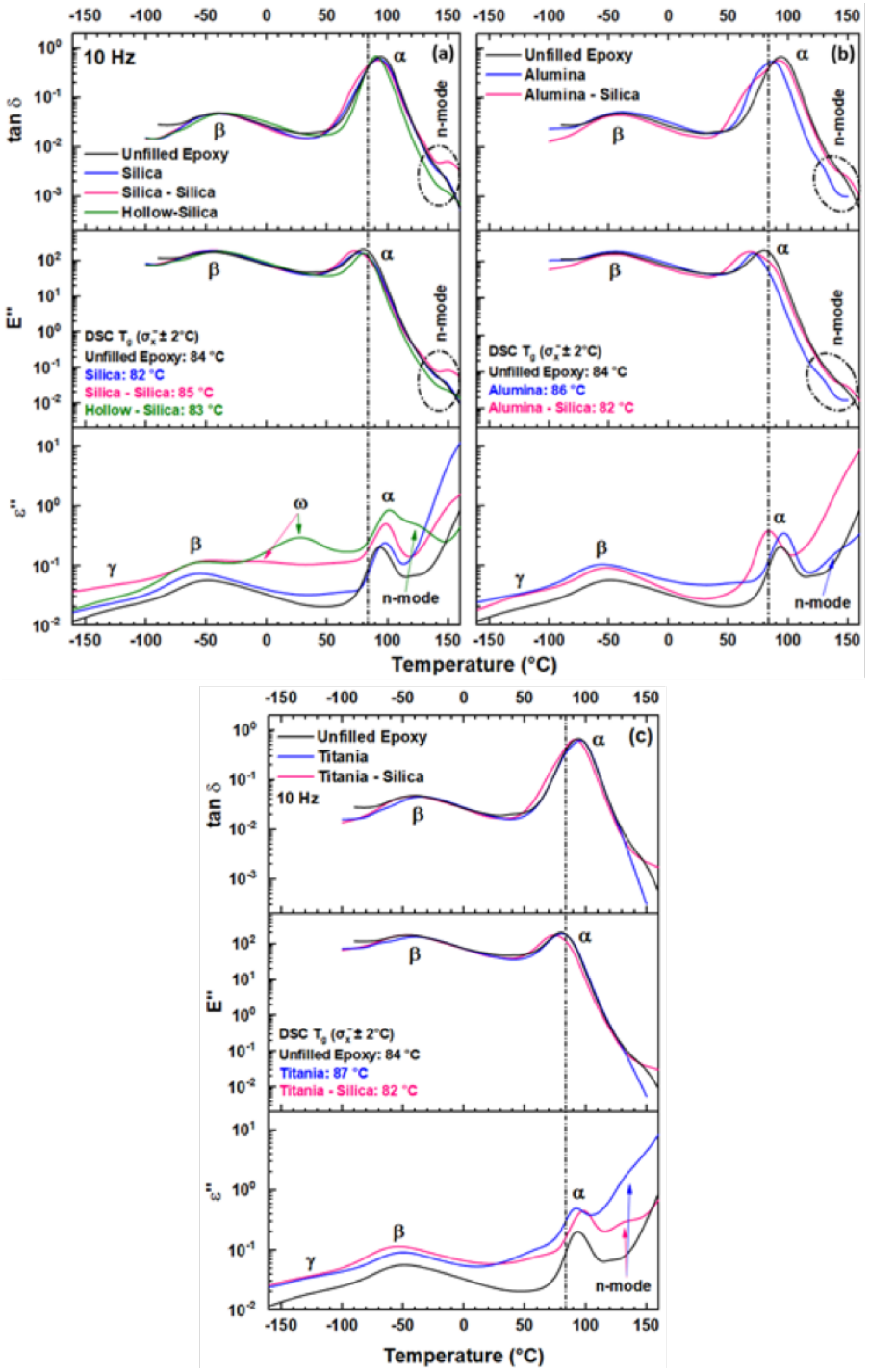

FIGURE 5.4: DMA - tan δ and loss modulus (E") spectra for a temperature range of -100 °C – 160 °C along with derived imaginary permittivity (ε") spectra from BDS for a temperature range of -160 °C – 160 °C at a frequency of 10 Hz illustrating different relaxation phenomena and the T_g values from DSC for (a) reference - unfilled epoxy sample and epoxy nanocomposite samples filled with SiO_2, SiO_2-SiO_2 and h-SiO_2 (b) reference - unfilled epoxy sample and epoxy nanocomposite samples filled with Al_2O_3 and Al_2O_3-SiO_2 and (c) reference - unfilled epoxy sample and epoxy nanocomposite samples filled with TiO_2 and TiO_2 – SiO_2. The dot-dash-dot line at 84 °C in all plots represents the T_g for unfilled epoxy sample from DSC measurements.

hypothesised based on the interphase volume calculations or the interphase volume fraction in the bulk nanocomposite; out of these, most widely accepted hypothesises are from the studies by Tsagaropoulos (203) and Tanaka (80). Both these model assume multiple layers of polymer chain with varying mobility due to their interaction with the nanoparticles and their cumulative thickness to be ~ 90 Å. As such, for a simplistic approach in the present study the interphase volume has been calculated based on this value. The volume of the interphase is in similar ranges i.e. 2.60 ± 0.08, except for TiO_2-SiO_2 where it is approximately one and half times higher. As expected, besides TiO_2-SiO_2, similar interaction characteristics of core-shell nanoparticles correlate with similar volume of the interphase. Similar arguments could be presented for the variation in the width of the tan δ peak; where similar interaction leads to similar width.

All the core type nanoparticles are calcinated resulting in an ordered structure; hence, the concentration of hydroxyl group on their surface would be significantly less. As a result, interaction between the hydroxyl group and hydroxy ether segment of the epoxy would be less likely. Therefore, the intensity and the width of the tan δ for core type nanoparticle filled nanocomposites shows no significant changes when compared to unfilled epoxy. In comparison to core type filled epoxy nanocomposites core-shell nanoparticle filled samples show a noticeable increase in the width of the tan δ and a reduction in its intensity. This highlights that the constrains on motion of polymer chains are higher in core-shell nanoparticle filled samples.

The concentration of the filler significantly influences the storage modulus (E') of the nanocomposite samples. Polymer chains in samples filled with higher concentration of fillers experience higher steric hindrance. Consequently, it has been reported in the literature that the E' of filled polymer samples in the rubbery region is usually higher than unfilled samples (199). However, the presented values of E' illustrate contrary results. As the concentration of the nanoparticles decreases, the value of E' remains approximately the same (15.60 ± 0.10), except for h-SiO_2 and TiO_2 filled nanocomposites. At T_g + 30 °C, all the polymer chains are activated and mobile; therefore, with reduced concentration, for the E' to remain constant there should be additional constrains on the movement of the polymer main chains. It is plausible that the increase in stiffness originate from the steric hindrance in the interphase.

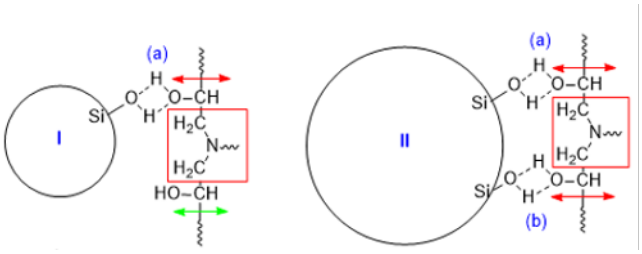

FIGURE 5.5: Illustration depicting the formation of single (I) and double hydrogen (II) bonds with the change in size of the nanoparticle. The arrows indicate the freedom of movement for the C – H group of the main chain; where red arrow shows a constrained motion and green arrow shows a motion with higher degree of freedom.

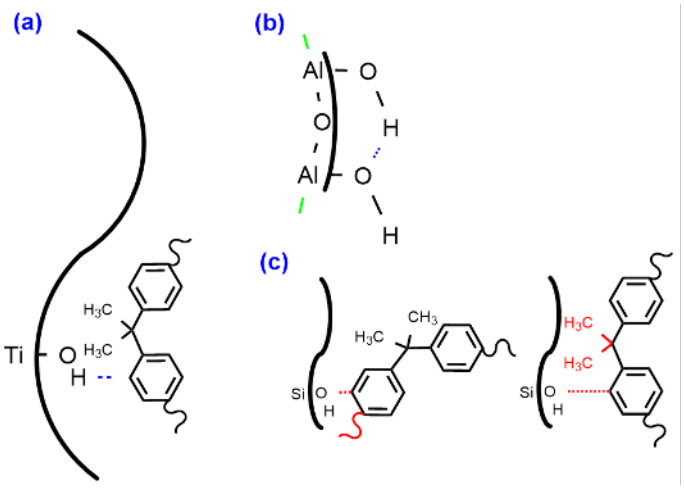

FIGURE 5.6: Illustration depicting the recesses on surface of (a) TiO_2 (Tetrahedral) – 55 nm (b) Al_2O_3 (Octahedral) – 50 nm and (c) SiO_2 (Tetrahedral) – 15 nm due to the different structure of the nanoparticles. For the interaction of the benzene ring with a hydroxyl proton on the surface, the plane of the benzene ring needs to be slightly perpendicular to the OH direction of the hydroxyl group on the surface. Due to the bigger size of the nanoparticle OH – π (blue dotted line) interactions are possible as benzene rings experience less steric hindrance and can conform to the required angle. However, this might not be possible in case of (c) SiO_2 (red dotted and red curly line). (b) also illustrates the formation of hydrogen bonds between Al – OH groups due to the convex geometry.

The coordination structure of the cationic element in the bulk could have a significant effect on interphasial interactions (198). Orthogonal structure of Al_2O_3 leads to only convex recesses on its surface. SiO_2 and TiO_2 due to their tetrahedral structure have both convex and concave recesses on their surfaces; where only the former are hydroxylated. The bond length of Al – OH and Ti – OH are similar, approximately 1.94 Å. However, due to the difference in the surface structure, X – OH (X: Si or Ti) comparatively interacts less with other X – OH groups on the particle surface as a result of large gap between the oxygen atoms, illustrated in Figure 5.6. Therefore, due to the availability of X – OH, OH – π interactions will be more prominent in XO_2. OH – π is a weak diffused interaction; thus, it does not affect the internal friction significantly but does improve the compatibility between the particle and polymer. Due to the significant difference in the size of the nanoparticles between TiO_2 and SiO_2 the respective size of the recesses would also vary significantly. Thus, the epoxy benzene rings would experience less steric hindrance accessing the hydroxylated concave recesses in case of TiO_2 as compared to SiO_2. Hence, OH – π interactions are more likely in case of TiO_2 filled system, resulting in a higher compatibility and an increased E'.

h-SiO_2 has significantly different behaviour than both core-shell and core-type nanoparticles. It has the lowest T_g, highest intensity and the smallest width, implying a highly plasticised system. This behaviour could potentially be a result of significant increase in the concentration of silanols on the surface of the shell leading to formation of hydrogen bonds which act as plasticizers. Firstly, increase in silanol concentration on the shell surface is unlikely since all SiO_2 shells were synthesised in the same way and none of the other sample shows such behaviour. However, if the epoxy chains penetrate the inner surface of

the h-SiO_2 which also has silanols, it is possible that this leads to a higher plasticizing effect. Secondly, it is possible that even after similar preparation procedure the synthesised shell is highly disordered resulting in a higher concentration of silanols on the surface.

Finally, it is important to consider the volumetric effect of the shell on the interphasial properties as well; therefore, the volume of shell for all the nanoparticles was calculated and is presented in Table 5.3 The condensation of silicic acid takes place at a constant rate per mole. The during of vacuum drying was the same for all the core-shell and hollow nanoparticles. The volume of the shell increases as the size of the nanoparticle increases even though the shell thickness is approximately the same across all the samples 25 – 30 nm. Hence, at constant rate of heat, less amount silicic acid would condense as the volume increases, introducing higher degree of disorder. This was reported in the Chapter 4, where h-SiO_2 with a higher shell volume as compared to SiO_2-SiO_2 had a higher degree of disorder. The degree of disorder directly corresponds to the concentration of the silanols on the surface. Across all the core-shell nanoparticles the intensity of the ν_{as}-LO band which is observed at 1170 cm^{-1} is highest in SiO_2-SiO_2 followed by Al_2O_3-TiO_2 and TiO_2-SiO_2, which implies the degree of disorder across these samples is also in same order; although it only varies noticeably. Even though the shell-volume of Al_2O_3-SiO_2 is similar to h-SiO_2 the degree of disorder in Al_2O_3-SiO_2 is significantly less. Furthermore, considering TiO_2-SiO_2 where the volume of the shell is significantly higher than h-SiO_2, it still has a low intensity ν_{as}-LO absorbance band. It is plausible that the core nanoparticle acts as a template which reduces the degree of disorder in the silica shell when X – O – Si bonds are formed, where X is either Si, Al or Ti. Therefore, since the degree of disorder is not significantly different in the core-shell nanoparticles they have similar interaction characteristics whereas h-SiO_2 which comparatively has higher degree of disorder results in an increased concentration of silanols on the surface. This leads to higher hydrogen bond interaction resulting in a highly plasticized system. Furthermore, this chemical variation in the structure of the nanoparticle would also ideally change the net charge distribution within the system which would affect the dipoles; this could potentially be the reason for the ω relaxation not being observed in the any metal oxide filled nanocomposite. Highly disordered system should result in a system with multiple Si – OH dipoles. Hence, the strongest ω relaxation peak is observed in h-SiO_2.

Sample ID	**Shell Volume (mm^3)**
SiO_2-SiO_2	30.40
h-SiO_2	48.70
Al_2O_3-SiO_2	47.60
TiO_2-SiO_2	75.20

TABLE 5.3: Calculated value of SiO_2 shell volume for all the core-shell nanoparticles.

5.2.4 β relaxation and n-mode

The β relaxation is often attributed to the crankshaft motion of the glyceryl segments in epoxy-amine networks. The relaxation features obtained from the E' vs. temperature profile such as the height, width and the intensity are presented in Table 5.4.

Considering the β maxima, it can be observed that besides h – SiO_2 it is approximately the same for all the samples (-45.20 ± 0.50 °C). In comparison, h – SiO_2 has a β maxima at -38.35 °C, implying faster segmental dynamics of the side chains. Furthermore, the intensity of β relaxation for core-type filled nanocomposites also corresponds to the trend of T_g. TiO_2 nanocomposite with the highest T_g also has the least internal friction, followed by unfilled epoxy, SiO_2 filled nanocomposite and finally, Al_2O_3 filled nanocomposite with the lowest T_g also has the highest β relaxation intensity. The constrains on the hydroxyl group further emphasis the impact of OH – π interactions. Although similar constrains were not observed on the main chain. This potentially suggests that the nature of constrains on the side chain groups also impact the T_g of the bulk system. All the core-shell nanoparticle filled epoxy nanocomposites also show similar intensity, it is higher than unfilled epoxy indicating a lower T_g. This again corresponds well with their respective T_g which are all lower than unfilled epoxy and are also approximately the same. Finally, as the constrains on the side chain increases the width of the tan δ would also increase since due to the additional constrains the range of activation temperature for the groups would increase. The values for the width correlate with the intensity values. Table 5.5 presents the T_g values obtained from DSC measurements. No significant changes are observed, the noticeable variations are within the experimental error limit of ±2 °C. Between DMA and DSC, DMA comparably provides much accurate and insightful values of T_g and other parameters, the experimental error in DMA values is only 1% or ~ ° 0.90 °C.

Sample ID	**β Maxima(K)**	**Intensity (T_g)**	**Width (K)**
Unfilled Epoxy	-46.25	128.69 (93.88)	63.26
SiO_2	-44.68	131.10 (92.70)	61.38
SiO_2 -SiO_2	-45.63	136.90 (91.14)	58.60
h-SiO_2	-38.35	144.90 (90.33)	59.80
Al_2O_3	-44.32	148.14 (86.17)	54.71
Al_2O_3 -SiO_2	-45.64	134.72 (91.32)	56.73
TiO_2	-44.35	121.56 (95.34)	63.10
TiO_2 - SiO_2	-45.60	138.42 (91.10)	58.80

TABLE 5.4: Values of different parameters for βrelaxation obtained from DMA – E" vs. temperature plots. β maxima: position of E" maxima, Intensity: E" peak maxima and Width: FWHM of E"

Finally, at higher temperature above 140 °C, large scale cooperative macromolecular motion in the elastic and rubbery region could give rise to additional friction losses, increasing the value of the loss modulus. These relaxation peaks are analogous to the normal mode relaxation in the BDS. Normal mode relaxation in BDS is attributed to the long range

Sample ID	Tg
Unfilled Epoxy	84.00
SiO_2	82.00
SiO_2 -SiO_2	85.00
h-SiO_2	83.00
Al_2O_3	86.00
Al_2O_3 -SiO_2	82.00
TiO_2	87.00
TiO_2 -SiO_2	82.00

TABLE 5.5: T_g values obtained from DSC.

end-to-end dipole vector along the polymer chain and is related to the changes in the conformation of the polymer chains and their molecular weight (155). For example, unlike BDS, in DMA normal mode relaxation is clearly observed in case of SiO_2-SiO_2 filled sample. The presence of normal mode relaxation in DMA implies its presence in BDS. It is likely that both the interfacial polarization peak and the normal mode relaxation are overlapping each other. Therefore, the BDS spectra at lower frequencies can be treated accordingly by deconvolution of these peaks, leading to a better understating of the molecular dynamics.

5.3 Broadband Dielectric Spectroscopy

5.3.1 β relaxation

Figure 5.7 presents the broadband dielectric spectroscopy data for Al_2O_3, Al_2O_3-SiO_2, TiO_2 and TiO_2-SiO_2 nanoparticle filled epoxy nanocomposites at temperatures of -70, -60 and -50 °C in the frequency range of 10^{-1} – 10^3 Hz along with their respective Havriliak – Negami fitting curves. As expected, the β relaxation peak is observed whose frequency of peak maxima (f_{max}) shifts towards higher frequency with an increase in temperature. To maintain consistency between the fitting curves the α and β parameters of Havriliak – Negami fitting were maintained in similar ranges. Visually, no significant changes are observed. To analysis the characteristics of the relaxation and changes in behaviour the relaxation, peak different samples were compared at -50 °C, presented in Figure 5.8. Table 5.6 complies the location of the f_{max} and dielectric strength ($\Delta\varepsilon$) of the respective peaks. Considering first f_{max}, both the core type nanoparticle have a similar frequency at which the peak maxima occurs. This suggests that the environmental constrains of the hydroxyl groups and side chain groups are similar in both the nanocomposites. In this frequency range, majority of the contribution to the relaxation behaviour originates from change in the orientation of the dipoles. A reduction in the frequency generally implies slower segmental dynamics of the dipoles or the crankshaft motion of the hydroxyl groups. Thus, the addition of nanoparticles has led to constrained motion of the dipoles when an electric field is applied. TiO_2 demonstrates the highest constrain amongst unfilled epoxy and core-type nanoparticles. Secondly, the $\Delta\varepsilon$ describes the temperature-dependent intensity of

the relaxation; dependent also upon the dipole moment of the groups involved and number density of dipoles. Since the measurement temperature and preparation method is same for these nanoparticles where stoichiometry was maintained the increase in $\Delta\varepsilon$ could only possibly result from the change in the dipole moment of the hydroxy ether groups. In accordance to the discussion earlier, OH – π interaction which lead to stabilization of the benzene ring of the main chain could result in a charge distribution resulting in stronger hydroxyl dipoles. The dielectric strength is approximately the same between the two core-type nanoparticles, which implies that both nanoparticle interaction with the polymer are the same. However, this is not in line with the DMA analysis where TiO_2 showed stronger OH – π interactions. It is plausible that there are other forms of weaker interactions which affect the dipole moment but do not lead to steric hindrance.

For core-shell filled nanocomposites, the f_{max} reduces even further which implies even more constrained environment for the hydroxyl groups. However, the $\Delta\varepsilon$ does not vary significantly. These additional constrains could either come from physically from steric hindrance or chemically from additional bonding. However, formation of bonds would lead to a change in the dipole moment of the hydroxy ether groups which in turn will change the $\Delta\varepsilon$. Therefore, the constrains are possibly more physical in nature than chemical.

Sample ID	$\mathbf{f}_{max}$	$\Delta\varepsilon$
Unfilled Epoxy	34.35	0.80
Al_2O_3	28.66	1.03
Al_2O_3-SiO_2	18.96	0.83
TiO_2	27.03	1.10
TiO_2-SiO_2	11.40	0.78

TABLE 5.6: Dielectric strength ($\Delta\varepsilon$) and f_{max} of the β relaxation for all the nanocomposite and unfilled epoxy sample obtained from Havriliak – Negami fitting at -50 °C.

Figure 5.9 illustrates the Arrehinus plots of the observed β relaxation from which the respective activation energy of the relaxation for each sample was calculated. Firstly, as expected, all the plots are parallel to each other indicating the type of groups involved in the similar in nature. Secondly, the activation energy does not vary significantly across the samples. Nevertheless, between core-type and core-shell filled nanocomposites the activation energy for former is slightly higher. Although inconclusive, this could potentially imply that constrains as a result of dipole interactions are slightly higher as compared to those due to physical steric hindrance.

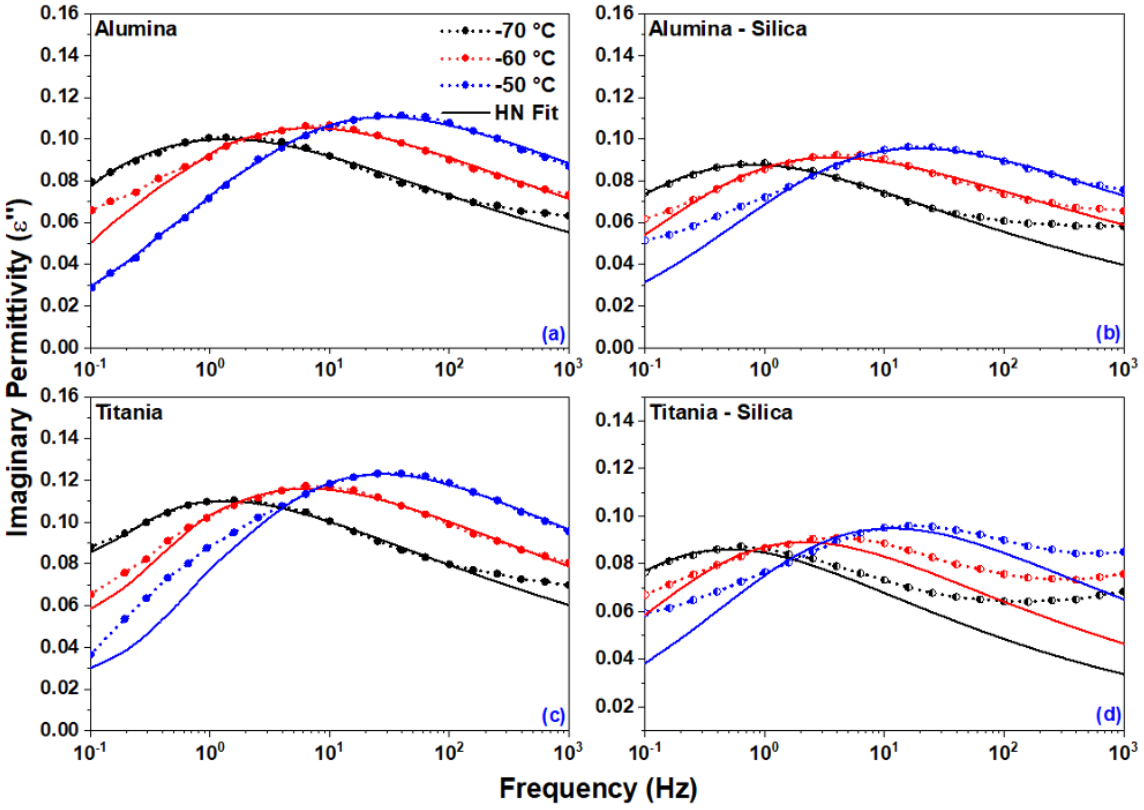

FIGURE 5.7: Broadband dielectric spectroscopy plots of β relaxation in (a) Alumina: Al_2O_3, (b) Alumina – Silica: Al_2O_3 – SiO_2, (c) Titania: TiO_2 and (d) Titania – Silica: TiO_2 – SiO_2 filled epoxy nanocomposites in the frequency range of 10-^1 – 10^3 Hz at -70, -60 and -50 °C with their respective Havriliak – Negami fitting.

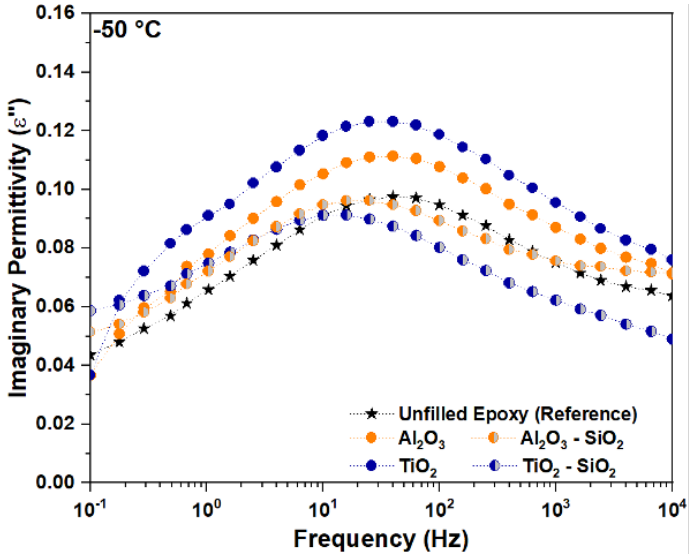

FIGURE 5.8: Broadband dielectric spectroscopy plots of β relaxation in Alumina: Al_2O_3, Alumina – Silica: Al_2O_3 – SiO_2, Titania: TiO_2 and Titania – Silica: TiO_2 – SiO_2 filled epoxy nanocomposites and unfilled epoxy in the frequency range of 10-^1 – 10^4 Hz at -50 °C.

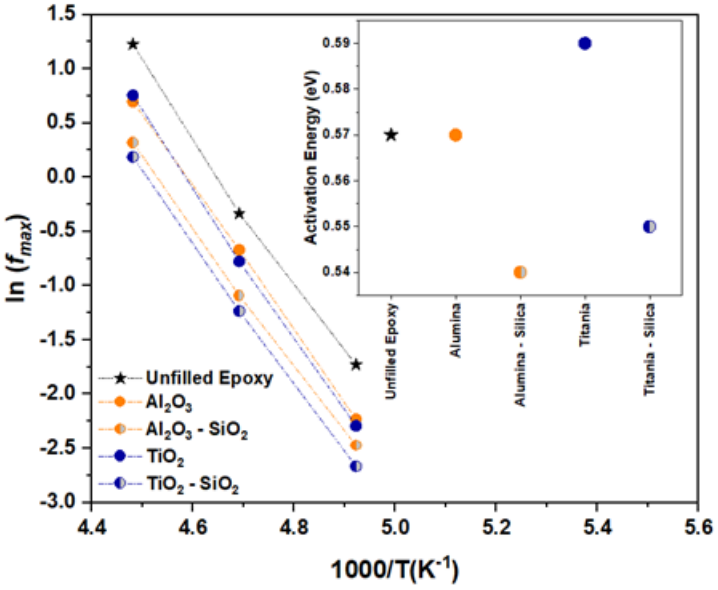

FIGURE 5.9: Arrehinus plot of β relaxation for Alumina: Al_2O_3, Alumina – Silica: Al_2O_3 – SiO_2, Titania: TiO_2 and Titania – Silica: TiO_2 – SiO_2 epoxy nanocomposites and unfilled epoxy sample along with their respective activation energy plot in the inset.

5.3.2 α relaxation

Figure 5.10 presents the measured broadband dielectric spectroscopy data for Al_2O_3, Al_2O_3 - SiO_2, TiO_2 and TiO_2 - SiO_2 nanoparticle filled epoxy nanocomposites illustration the α relaxation at temperatures of 100 and 140 °C in the frequency range of 10^{-1} – 10^5 Hz. However, additionally conductivity features are clearly observed in the spectra. To remove these features in order to analyse the α relaxation Kramer-Kronig formulation were used to obtained derived spectra. Figure 5.11 presents these derived spectra at a temperature of 90, 100, 110 and 120 °C and in the frequency range of 10^{-1} – 10^4 Hz along with their respective Havriliak – Negami fitting (HN-fitting). The temperature in these plots are chosen such that either a significant part of α relaxation or the f_{max} of the respective temperature curve is visible in the selected frequency window; HN-fitting was not possible at all temperatures. Therefore, not all plots present the curves between the 90 – 120 °C temperature range. Table 5.7 complies the location of the f_{max} and dielectric strength ($\Delta\varepsilon$) of the respective peaks at 100 °C which is a common temperature across all samples where α relaxation is distinctly visible.

Sample ID	**f$_{max}$**	$\Delta\varepsilon$
Unfilled Epoxy	23.64	2.54
Al_2O_3	43.12	2.73
Al_2O_3-SiO_2	3149.87	3.06
TiO_2	19.20	3.19
TiO_2-SiO_2	176.22	3.91

TABLE 5.7: Dielectric strength ($\Delta\varepsilon$) and f$_{max}$ of the α relaxation for all the nanocomposite and unfilled epoxy sample obtained from Havriliak – Negami fitting at 100 °C.

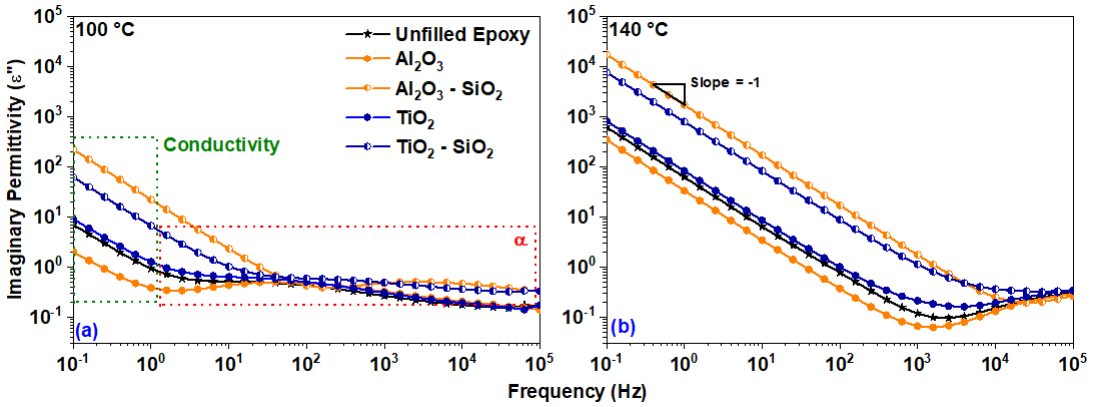

FIGURE 5.10: Measured broadband dielectric spectroscopy plots of α relaxation in Alumina: Al_2O_3, Alumina – Silica: Al_2O_3 – SiO_2, Titania: TiO_2 and Titania – Silica: TiO_2 – SiO_2epoxy nanocomposites and unfilled epoxy in the frequency range of 10^{-1} – 10^5 Hz at a) 100 °C and b) 140 °C. A slope of -1 is observed demonstrating the effect of conductivity in the spectra.

As expected, it can be observed from the dielectric spectra that as the temperature increase the $\Delta\varepsilon$ reduces. In epoxy, the $\Delta\varepsilon$ reduces from 2.54 to 2.50 with an increase from 100 to 110 °C. Similar to the β relaxation, the α relaxation segmental dynamics of TiO_2 nanocomposite are slower as compared to unfilled epoxy; this is also in line with the DMA analysis where the Tg of the TiO_2 nanocomposite is the highest. Similarly, for Al_2O_3 filled composites they are faster in comparison to unfilled epoxy which is again in line with DMA analysis. The core-shell nanocomposites on the other hand have significantly faster segmental dynamics; further, amongst the two segmental dynamics of Al_2O_3-SiO_2 are significantly faster than TiO_2-SiO_2. Considering now the $\Delta\varepsilon$, in core-shell nanoparticles the dielectric strength is significantly higher than unfilled epoxy and noticeably higher than core type filled nanocomposites.$\Delta\varepsilon$ of α relaxation is affected by the number density of dipoles, dipole moment and the different types of groups participating in the relaxation. The number density of dipoles is constant across all samples as the stoichiometry is maintained across all samples. Therefore, the difference in the $\Delta\varepsilon$ is potentially due to a combination of changes in the dipole moment and due to the different types of groups of the main chain participating in the relaxation process. Finally, after the removal of conductivity effects an additional relaxation is observed.

5.3.3 Interfacial Polarization and Normal Mode

Figure 5.12 presents the derived and measured broadband dielectric spectra for all the samples in the frequency range of 10^{-1} – 10^5 Hz at 130 °C where along with α relaxation multiple other peaks below the frequency of 10^3 Hz are observed. These peaks could not be deconvoluted consistently where the α and β parameters of the HN-fitting were in similar ranges over a span of different temperatures. Therefore, to analyse these peaks further and gain insight into the interfacial dynamics their respective Cole - Cole plots were made with the effect of conductivity removed; presented in Figure 5.13.

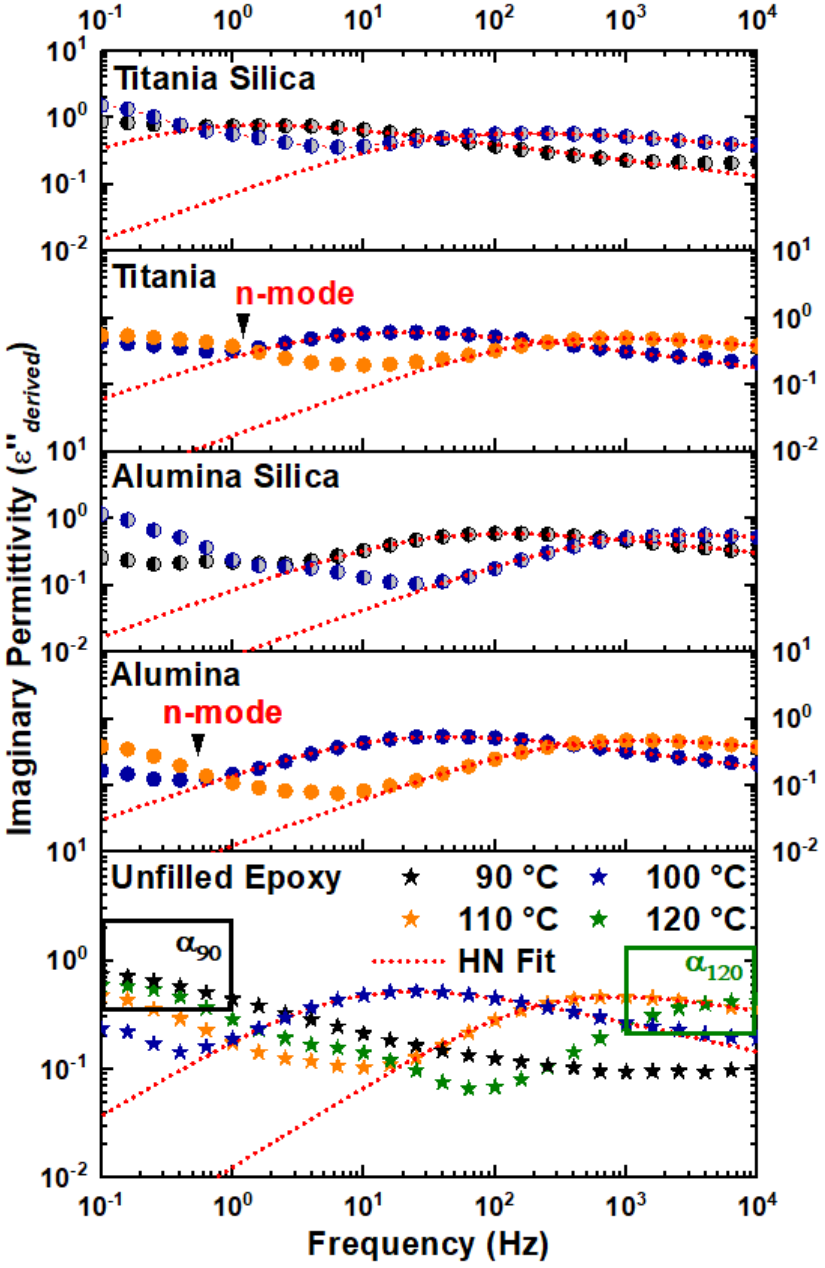

FIGURE 5.11: Derived broadband dielectric spectroscopy plots of α relaxation in (a) Alumina: Al_2O_3, (b) Alumina – Silica: Al_2O_3 – SiO_2, (c) Titania: TiO_2 and (d) Titania – Silica: TiO_2 – SiO_2 epoxy nanocomposites and unfilled epoxy in the frequency range of 10^{-1} – 10^4 Hz at 90, 100, 110 and 120 °C with their respective Havriliak – Negami fitting

Considering first the normal mode, unfilled epoxy as a reference sample does not have any filler content and there is no phase separation it in since it has a single well-defined α relaxation peak. At 130 °C, in accordance to the DMA measurements, the epoxy is in a rubbery state where the polymer chains are free to move and the only restriction originates from chain entanglements and crosslinking. Therefore, the peak observed in case of unfilled epoxy is the normal mode relaxation peak which depends on the end to end dipole moment of the entire polymer chain. Similar, the normal mode is observed in all other samples. However, it is moving towards lower frequency which implies that due to the addition of

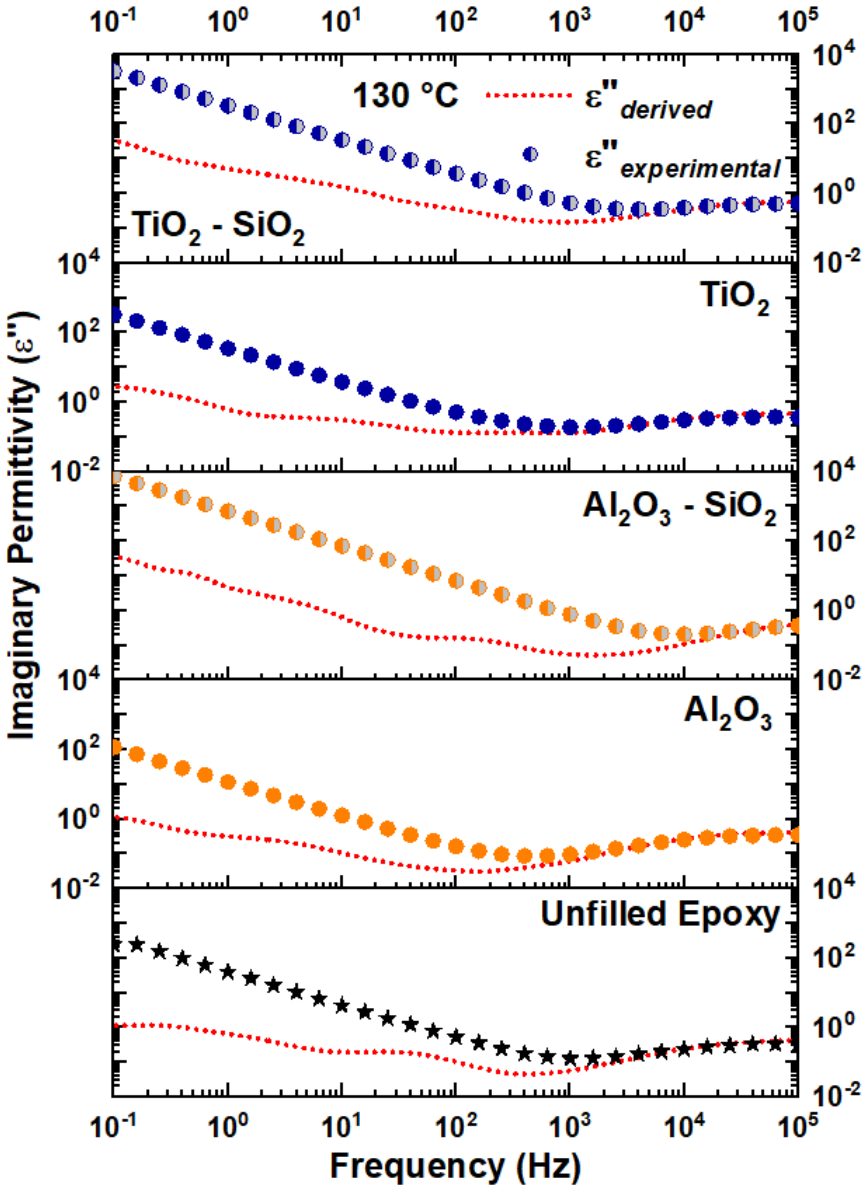

FIGURE 5.12: Derived and experimentally measured broadband dielectric spectroscopy plot α relaxation in Alumina: Al_2O_3, Alumina – Silica: Al_2O_3 – SiO_2, Titania: TiO_2 and Titania – Silica: TiO_2 – SiO_2 epoxy nanocomposites and unfilled epoxy in the frequency range of 10^{-1} – 10^5 Hz at 130 °C.

nanoparticles besides the conventional restrictions there additional constrains in the free movement of the polymer chains. TiO_2 nanocomposite has the slowest normal mode relaxation which in line with its Tg which is the highest amongst all nanoparticles. The core-shell nanocomposites are next and do not vary significantly. Although Al_2O_3 has the lowest Tg, unfilled epoxy has the fastest normal mode segmental dynamics since it only has entanglement restrictions and no additional constrains from the nanoparticles.

In case of core-type nanocomposites an additional peak apart from normal node relaxation is also observed, present in the inset of Figure 5.13. This peak appears after the normal mode relaxation towards even lower frequencies and is attributed to the interfacial

polarization as a result of the particle-polymer interface. Further, in case of core-shell nanoparticles, two interfacial polarization peaks are observed instead of one. This is potentially due to the presence of an additional interface within the particles i.e. the core-shell interface. In case of Al_2O_3-SiO_2 the first peak between 10 – 15 ε' is wide and has high $\Delta\varepsilon$ whereas the second peak observed at even lower frequencies is similar in its width but has reduced $\Delta\varepsilon$. The dipoles at the shell-polymer interface would be relatively less constrained as compared to core-shell interface. Therefore, it would be at a comparatively higher frequency. Hence, the peak between observed between ε': 10 - 15 is ideally due to the polymer-shell interface and the second at lower frequencies is potentially due to the core-shell interface. Similarly, in case of TiO_2-SiO_2, both the peaks are observed in similar ε' ranges. However, the second peak is higher in intensity or $\Delta\varepsilon$ as compared to Al_2O_3-SiO_2. The difference in the real permittivity of TiO_2 and SiO_2 is higher than between Al_2O_3 and SiO_2. Therefore, it is expected that the peak related to the core-shell interface of TiO_2-SiO_2 will have higher $\Delta\varepsilon$.

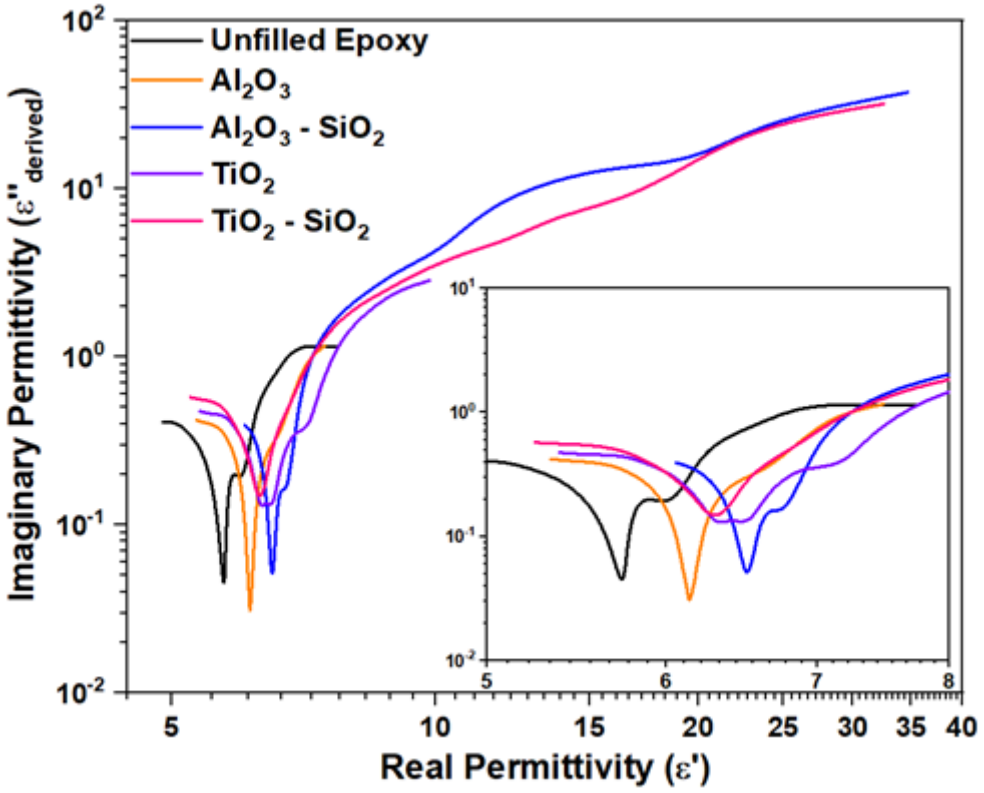

FIGURE 5.13: Cole-Cole plots of Alumina: Al_2O_3, Alumina – Silica: Al_2O_3 – SiO_2, Titania: TiO_2 and Titania – Silica: TiO_2 – SiO_2 epoxy nanocomposites and unfilled epoxy at 130 °C.

Figure 5.14 illustrates the derived broadband dielectric spectra for all the nanocomposites and unfilled epoxy in the frequency range of 10^{-1} – 10^5 Hz at 140 °C. Similar to the Cole-Cole plots, besides the α relaxation one additional relaxation is observed in core-type nanocomposites i.e. normal mode and two in case of core-shell nanocomposites i.e. normal mode and interfacial polarization. The real permittivity difference between the core-type nanoparticles and epoxy is significantly high still an interfacial peak is not observed at this temperature. However, in case of core-shell nanocomposites even though the real

permittivity of SiO_2 is similar to that of epoxy a distinct interfacial polarization peak is observed. This suggests that the core nanoparticle does play an important role in determining the interfacial polarization characteristics. Furthermore, the normal mode and interfacial polarization both overlap in case of TiO_2-SiO_2 filled nanocomposite due to the increase in the width of the interfacial polarization. It is plausible that as the permittivity difference between the core and the shell increases the core-shell interface polarization increases and increases the width of the interfacial polarization peak leading it to overlap with the normal mode relaxation.

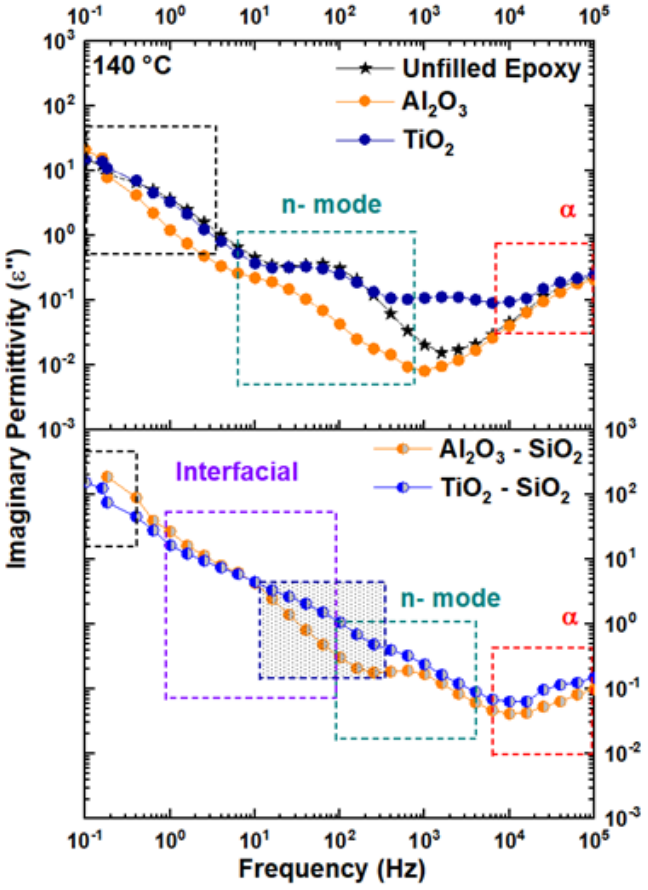

FIGURE 5.14: Derived broadband dielectric spectroscopy plots of Alumina: Al_2O_3, Alumina – Silica: Al_2O_3 – SiO_2, Titania: TiO_2 and Titania – Silica: TiO_2 – SiO_2 epoxy nanocomposites and unfilled epoxy in the frequency range of 10^{-1} – 10^5 Hz at 140 °C. The red dotted box represents the α relaxation, green box the normal mode relaxation, blue box and overlap of normal mode and interfacial polarization in Al_2O_3 – SiO_2, purple box the interfacial polarization and the black box the indiscernible peaks or features.

5.4 Summary

Eight different type of nanocomposites, namely, unfilled epoxy (reference), SiO_2, Al_2O_3, TiO_2, Al_2O_3-SiO_2, TiO_2-SiO_2 and h-SiO_2 were investigated via DMA at a frequency of 10 Hz and in a temperature range of -100 – 160 °C. Secondly, Al_2O_3, TiO_2, Al_2O_3-SiO_2, TiO_2-SiO_2

nanocomposites were further analysed via FTIR and BDS. To confirm the successful synthesis of the nanoparticle in conjunction to the FTIR, TEM graphs were also investigated. The nanocomposites were prepared by maintaining similar total surface area of nanoparticle based on their density and size. The stoichiometric ratio between the resin and hardener were marinated across all samples. FTIR analysis was done on three different regions on the nanocomposites, namely, hydroxyl group (3600 – 3100 cm^{-1}), hydrocarbon fingerprint region (3000 – 2800 cm^{-1}) and unreacted epoxide absorbance band (960 – 900 cm^{-1}). Core-shell nanoparticle showed a noticeable increase in the concentration of the hydroxyl group attributed to be originating from the silanols on the surface of the shell. A noticeable increase in the absorbance of the symmetric and asymmetric vibration of the CH_2 and CH_3 group was also observed. This behaviour was attributed to the OH – π interaction of the silanols with the polymer main chain benzene ring where due to the stabilization of the ring a charge redistribution would lead to change in the dipole moment of the associated hydrocarbon groups. No significant changes were observed in the unreacted epoxide concentration. FTIR of the nanoparticle powder further revealed the presence of – OH groups. Additionally, formation of Ti – O – Si and Al – O – Si bonds was also observed, implying the formation of core-shell structure. Further, the TEM graphs confirmed their formation. α relaxation analysis via DMA revealed a singular well defined relaxation peak for all samples but Al_2O_3-SiO_2 where two overlapping relaxations were observed in the tan δ thermograph at a temperature lower than then the T_g of the sample. This peak was attributed to the micro-phase separation in the polymer chain in the immediate vicinity of the nanoparticle. In terms of core-type nanoparticle, SiO_2 showed neutral behaviour in the polymer showing no major changes in the intensity, width and the storage modulus of the system when compared with the reference sample. Al_2O_3 showed a repulsive behaviour leading to a reduction in the T_g whereas TiO_2 showed an attractive behaviour resulting in an increase in the T_g. However, their intensity and the width of the tan δ was similar. Additionally, the storage modulus was the same in the unfilled epoxy and SiO_2 where as it decreased in Al_2O_3 nanocomposite and increased in TiO_2 nanocomposite. These behaviours were explained on the basis of the structure of the surface of the nanoparticle. Where due to structural difference Al_2O_3 and SiO_2 do not majorly interact with the polymer whereas TiO_2 does in form of Ti – OH – π interactions. All core-shell nanoparticles showed similar behaviour where the intensity, width and storage modulus showed no significant changes irrespective of the size of the particle. The T_g reduced which was attributed to the plasticizing effect of the hydrogen bonds formed between the surface silanols and the hydroxy ether group of the epoxy main chain. Even the T_g reduced a simultaneous reduction in the intensity of tan δ was also observed, this was attributed to the reduction of the internal friction of the system due to the steric hindrance in the interphase due to the surface silanols. Similarly, the storage modulus increased which was attributed to similar reasons. This behaviour was explained based on the similar surface area of the nanoparticle and the same SiO_2 shell which forms an interphase with the polymer. h-SiO_2 showed a significantly different behaviour as compared to both core and core-shell type filled nanocomposites. This was primarily due to a volumetric effect where due to the increase in the volume of the shell the disorder in the structure increased resulting in a higher concentration of silanols on the surface which lead to a highly plasticized system. β

relaxation analysis showed comparable behaviour as α relaxation. DMA analysis conclusively demonstrated that both the core, shell and the structure of the nanoparticle plays an important role in determining the properties of the bulk nanocomposite. Finally, a relaxation behaviour at higher temperature analogous to normal mode relaxation was observed in unfilled epoxy, SiO_2, Al_2O_3, Al_2O_3-SiO_2, and h-SiO_2 samples. DSC measurements showed no significant difference in the T_g of the samples. The dielectric analysis was performed at various temperature depending upon the relaxation. The β relaxation showed similar behaviour as was observed in the DMA. Addition of nanoparticles lead to slower segmental dynamics potentially attributed to the steric hindrance. However, the segmental dynamics in core-shell nanoparticles were significantly slower. This was attributed to the formation of hydrogen bonds resulting in increased constrains on the hydroxyl groups and side chains. The β activation energy across all system was approximately the same. The α relaxation for unfilled epoxy and core type nanocomposites showed similar behaviour as DMA. However, the core-shell structure showed faster segmental dynamics. This was attributed to the overall plasticizing effect of these nanoparticles due to hydrogen bonds. Finally, the interfacial characteristics were analysed by utilising Havriliak Negami and Cole-Cole formulations. A normal mode relaxation was observed in all the investigated samples. The normal mode relaxation corresponds well with the trend of T_g for these samples. In case of Al_2O_3 nanocomposite even though its T_g is lower than the unfilled epoxy the normal mode segmental dynamics were slower. This was attributed to the additional steric hindrance from the nanoparticles as compared to unfilled epoxy where only chain entanglements are the major restrictions. Single interfacial polarization peaks were observed in case of core-type nanoparticles whereas for core-shell nanoparticles two peaks are observed. The peak at higher frequencies was attributed to the interfacial polarization between the shell and polymer. The second peak at lower frequencies was attributed to the core-shell interface. The difference in the real permittivity of the core and the shell noticeably influences the dielectric strength of these peaks. Therefore, conclusively the additional interface with in the particle also affects the interfacial properties of the bulk system.

Chapter 6

Concluding Remarks

This Chapter summarizes the main findings of the study and suggests further investigations as future work.

6.1 Conclusions

In the study presented above, seven different nanoparticles, namely, SiO_2, SiO_2-SiO_2, h-SiO_2, Al_2O_3, Al_2O_3 - SiO_2, TiO_2 and TiO_2 - SiO_2 based epoxy nanocomposites were investigated along with an unfilled reference sample. All the core-shell and hollow nanoparticles were synthesised in the laboratory via sol-gel method and the core-type were commercially obtained. These samples were investigated via. FTIR, DSC, BDS in the frequency range of 10^{-1} - 10^5 Hz and in the temperature range of -160 to 160 °C, DMA in the temperature range of -100 to 160 °C and at a frequency of 10 Hz and TEM. The successful synthesis of the nanoparticle was confirmed with the help FTIR and TEM; where from FTIR the formation of shell was evident in core-shell nanoparticles due to the observed X - O - Si (X: Si, Al or Ti) bond formation and from TEM by visual confirmation along with gray scale analysis.

The epoxy nanocomposites were prepared using the solution blending method which gave the best dispersion in comparison to other method utilised. The epoxy nanocomposites were filled based on the total surface area of the nanoparticles rather than the conventional weight or volume percentage method since the study was focused on understating the interphasial properties and molecular dynamics due to the varying architecture of the nanoparticles. Epoxy nanocomposites were filled at three different loading levels relative to the surface area of TiO_2 - SiO_2 at 1, 5 and 10 wt.%. Only the samples with rel.5% surface area were investigated as out of the three these showed the best dispersion.

FTIR analysis of the SiO_2, SiO_2-SiO_2 and h-SiO_2 revealed an increasing trend for the ν_{as}-LO absorbance band which is attributed to the asymmetric stretching vibration of the Si - O - Si

bond in the amorphous region in the following trend: SiO_2 followed by SiO_2-SiO_2 and h-SiO_2. Thus, a controlled variation of the disorderliness of the surface shell structure was established. Further, an increase in the hydroxyl concentration was also observed with increasing disorderliness. In the BDS spectra as besides the conventional relaxations an additional relaxation phenomena was observed which was termed the ω relaxation. As the disorderliness of the surface shell structure increased the ω relaxation relaxation became pro-eminent. SiO_2 nanocomposite with an ordered structure did not shows any ω relaxation. SiO_2-SiO_2 nanocomposite showed an overlapping ω and β relaxation whereas in case of h-SiO_2 completely segregated and shifted towards higher frequencies. The behaviour and the activation energy of the ω relaxation is similar to the β relaxation. The ω relaxation was attributed to the hydrogen bond formation between the surface silanols which exist due to the an amorphous structure and the hydroxy ether group of the epoxy main chain. Therefore, a change in the structure or crystallinity of the nanoparticle evidently affects the molecular dynamic of the host polymer.

DMA analysis of the tan δ α relaxation of all the nanocomposite reveled that all the core-shell nanoparticles have approximately the same internal friction, width and storage modulus in the rubbery plateau. Similarly, all the core-type nanoparticle also had similar internal friction and width but varying storage modulus. h-SiO_2 has the highest storage modulus. This behaviour was attributed to two types of interactions hydrogen bonds and OH - π interactions. OH - π interaction were observed between the surface silanols and the benzene rings of the epoxy main chain. Based on the surface structure of the nanoparticles it was observed that only tetrahedral structure of above a critical size were able to have OH - π. Hence, it was only possible in case of TiO_2. Even though SiO_2 also has a similar structure but due to its smaller size benzene rings were unable to access the surface silanols which only exist in the concave recesses.

It was also observed that the presence of a core particle provides a template for the shell to grow and the disorderliness is reduced as compared when it is absent. Thus, core nanoparticle in someways plays an important role influencing the interphasial interactions. The nature of the core particle in terms of it permittivity plays a significant role when lower frequencies are considered. In case of core shell nanoparticles two interfacial polarization peaks were observed where the one at lower frequency was attributed to be originating from core-sell interphase. As the permittivity difference between the core and the shell increase the dielectric intensity of this peak also increased. In case of TiO_2-SiO_2 nanoparticles at a temperature of 150 °C the peak width significantly increase and overlapped with the normal mode relaxation. At similar temperatures SiO_2-SiO_2 showed no such behaviour.

In conclusion, the shell plays an more dominate role on the interphasial and dielectric properties of the nanocomposite when medium and higher frequencies are considered. However, when lower frequencies are considered the core-shell interphase along with the core particle plays a more dominant role.

6.2 Future Direction - Outlook

6.2.1 Effect of shell thickness

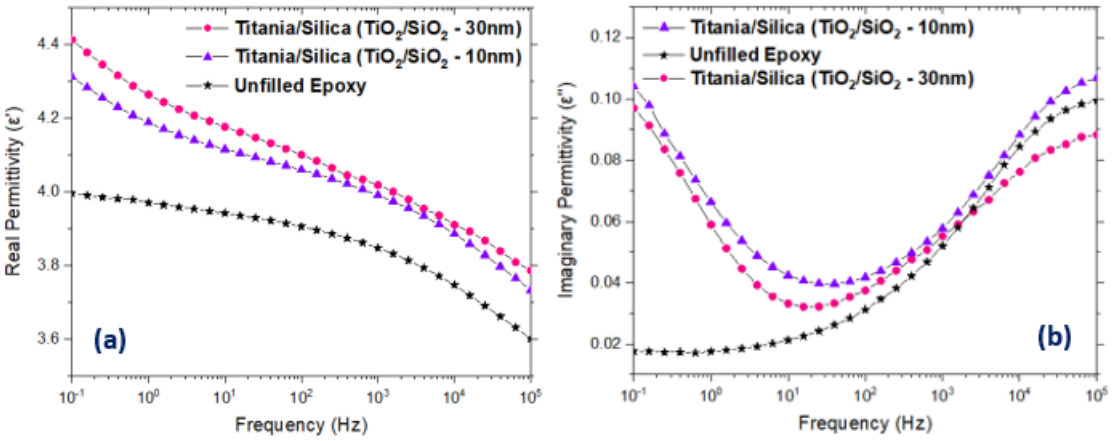

FIGURE 6.1: Broadband dielectric spectra of TiO_2 - SiO_2 core-shell nanoparticle with varying thickness of 10 nm and 30 nm filled epoxy nanocomposites a) Real permittivity b) Imaginary Permittivity

As part of a study, two different samples namely, TiO_2/SiO_2 - 10 nm filled epoxy nanocomposite and TiO_2/SiO_2 - 30 nm filled epoxy nanocomposite were evaluated based on dielectric measurements as a function of frequency (10^1 - 10^5 Hz). Both the core - shell type structures were successfully synthesised with different shell thickness which was confirmed by the TEM images presented. The samples were filled with an idea to keep their total surface area same across both the samples. In accordance to the dielectric measurements, the real permittivity of both the nanocomposite samples is higher than the unfilled epoxy sample. Where, TiO_2/SiO_2 - 30 nm filled sample has higher real permittivity between the two. The higher permittivity as compared to unfilled epoxy was explained as a result of addition of high permittivity nanoparticles into the system which dominates as the number of particles in the system increases. Hence, TiO_2/SiO_2 - 30 nm being bigger in size requires more number of particles to have the same surface area as TiO_2/SiO_2 - 10 nm. In the imaginary part, typical β relaxation is observed between the frequency of 10^4 - 10^5 Hz. As the number of particles increases due to the increase in the size of nanoparticles the intensity of hydroxyl groups reduces (β relaxation). Finally, towards the lower frequencies (10^1 - 10^0 Hz) interfacial polarization effect was observed in form of increased losses. However, between both the samples no significant difference was observed. This was explained potentially due to the surface area between the shell and core as well as between the shell and polymer being approximately equivalent for both the samples. Apart from this study, the shell thickness in the present research was maintained between 25 - 30 nm, with further insights from Chapter 5 and 6 possible future work could be to study the effect of shell thickness on the bulk dielectric properties of the nanocomposites.

6.2.2 Effect of inversion of the core and the shell

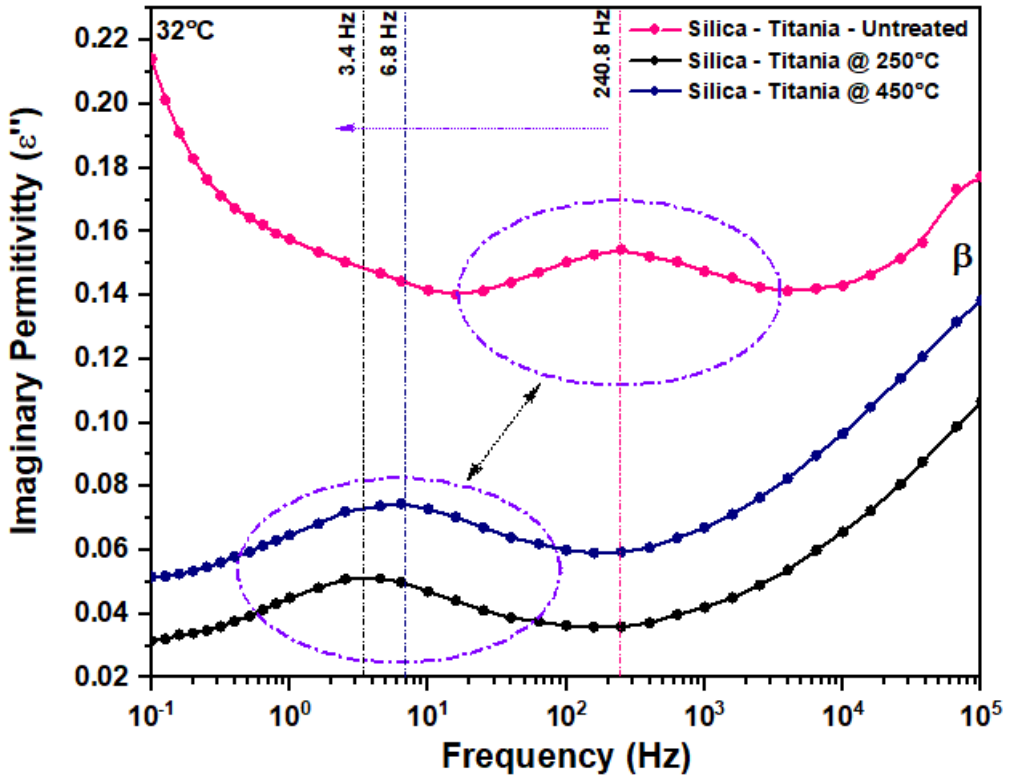

FIGURE 6.2: Imaginary broadband dielectric spectra of SiO_2 - TiO_2 core-shell nanoparticle filled epoxy nanocomposites calcined at 250 and 450 °C with reference vacuum dried (60 °C) SiO_2 - TiO_2 filled epoxy nanocomposite measured at 32 °C

Epoxy nanocomposites filled with nanoparticles where the core and the shell material are changed with each other as a continuation of the research could possibly help better understand the interphasial properties and the behaiour of some samples in the present research. Figure 6.2 shows the imaginary plot for epoxy nanocomposites filled with SiO_2 - TiO_2 core-shell nanoparticles which are treated in differently i.e. vacuum dired 60 °C, calcined at 250 °C and 450 °C leading to a different surface structure. A comparison between the temperature dependent broadband dielectric spectroscopy of SiO_2 - TiO_2 and TiO_2 - SiO_2 filled epoxy nanocomposite could further help determine the role of the core and the shell particles. Essentially, the core-shell bonds between both the nanoparticles are the same Ti - O - Si and Si - O - Ti. However, unlike TiO_2 - SiO_2 filled sample, here an additional peak is observed apart from β relaxation which initially shifts towards lower frequencies as the treatment temperature of the nanoparticle increases but as the temperature increases further moves slightly towards higher frequencies.

6.2.3 Effect of structure of the nanoparticle

In Chapter 5, the importance of the structure of the shell was highlighted where the shape and size of the recesses determined the possibility of OH - π interactions between the

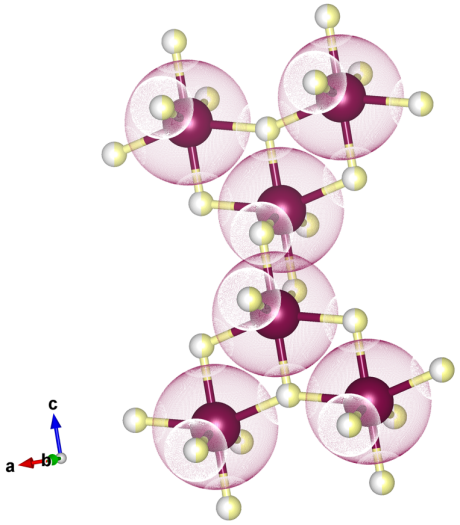

FIGURE 6.3: Structure of TiO_2 in SiO_2 - TiO_2 nanoparticle calcined at 250 °C obtained from XRD measurement and rietveld refinement

nanoparticle surface silanols and the benzene epoxy ring. Therefore, possible future work could look into the effect of the nanoparticle structure on the dielectric properties of the nanocomposite. Figure 6.3 shows the structure of TiO_2 in SiO_2 - TiO_2 nanoparticle calcined at 250 °C. The bond length and bond angle are noticeably different when compared with convectional TiO_2 nanoparticle.

Appendix A

Experimental Methods

To characterize the electrical, thermal and chemical properties of the samples three different techniques were employed, namely: broadband dielectric spectroscopy (BDS), differential scanning calorimetry (DSC) and Fourier transform infra-red spectroscopy (FT-IR) respectively. Transmission electron microscope (TEM) graphs was used to analyse the dispersion of nanoparticles and to determine their size via. image processing and analysis software i.e. ImageJ. Since, no measuring device is completely accurate and always has errors as a result of human manufacturing and surrounding environment. Table A.1 provides the error margin of different equipment used for characterisation.

Equipment Name	**Error**	**Condition**
SI 1260 Impedance/Phase gain analyser (V)	<2%	25 °C
SI 1260 Impedance/Phase gain analyser (A)	<2%	25 °C
1296 Dielectric Interface	±[5% + 1% MHz + 5mV]	25 °C
Omicron	<2%	25 °C
Lake Shore 332 (V)	± 2.5mV	-
Lake Shore 332[1] (Electronic Accuracy)	± 0.001 Ω ± 0.04 % of rdg[2]	<75 Ω
Lake Shore 332 (Temperature)	max. ± 20mK	Depends on Ω
STVP-200-XG Cryostat (TA[3] Stability)	≤50mK	-
DSC7	± 2 °C	-
ATR-FTIR iD7 Nicolet iS5 (λ)	± 0.01 cm^{-1}	at 5300 cm^{-1}
ATR-FTIR iD7 Nicolet iS5 (SNR)	10 μabS RMS	< 1 min

TABLE A.1: Error for different equipment used for characterization

[1]Current source error has negligible effect on measurement accuracy.
[2]Reading digit(s): Fixed error independent of the input.
[3]Temperature

A.1 Broadband Dielectric Spectroscopy

The dielectric response is a function of frequency and also temperature dependent. It is a measure of the interaction between the applied electric field and the dipole moment of the measured sample, expressed in form of complex permittivity. Permittivity represents the ability of a material to store energy. It consists of two parts the real permittivity (ε') and the imaginary permittivity (ε"). The real part which represents the energy storage is also usually referred to as the relative permittivity. The imaginary part which lags the electric field by 90°represents the losses occurring mainly as a result of dipole alignment with respect to the electric field. Further, the ratio between the imaginary part to the real part can be calculated which is called loss tan δ and is usually known as dissipation factor, providing an important relationship between the two parts of complex permittivity. Generally upon observing a dielectric spectroscopy graph peaks are observed. These peaks are related to different relaxation mechanisms which occur due to the alignment of the dipoles with the electric field at a given frequency. Alpha (α) – relaxation is the first one observed when moving from low frequency to high frequency and is attribute to the alignment of large dipoles such as the main polymer chain. Followed by beta (β) relaxation, which is related to the movement of smaller dipole movements such as hydroxyl groups. Finally, gamma (γ) relaxation related to the orientation of the individual smaller end chain terminal groups at high er frequencies. The permittivity is superimposition of these different types of polarization mechanisms such as ionic polarization, electronic polarization and orientation polarization. Although, for the measure frequency range 10^{-1} to 10^{6}, orientation polarization is dominant.

The dielectric response of the samples was measured via broadband dielectric spectroscopy (BDS) with the help of a Solartron 1296 dielectric interface along with a Schlumberger SI 1260 impedance/phase gain analyser and a Lake Shore 332 temperature controller. Some measurements were also separately done with the OMICRON Spectano 100 dielectric analyser. The samples were gold coated with a diameter of 20 mm and a thickness of 10μm. The measurements were done under two different temperature conditions. Initially, the measurements were performed under ambient temperature and Solartron 12962A room temperature sample holder was used. The electrodes used are made up of brass. The measuring electrode used had a diameter of 20 mm with a guard ring having an air gap of 1 mm. Square samples of size 4 cm × 4 cm were used for this setup. This same sample holder along with same sample specification was also used with the OMICRON Spectano 100 dielectric analyser. For the second setup, the sample was mounted on a Janis Research STVP 200 XG system cryostat. The cryostat can perform measurement in the temperature range of ≃ 5 K upto 600 K. This setup includes an integrated variable temperature sample chamber, a vacuum insulated cryostat body, a sample positioning assembly with a sample holder, connected with the temperature controller. Sample size used for this setup was 3 cm × 3 cm due to the restriction of narrow space available to access the electrodes. All the equipments are connected to each other with triaxial cables having Bayonet Neill–Concelman (BNC) connectors (Fig A.1).

Measurements performed on the Solartron 1296 used Solartron Materials Research and Test Software package (SMaRT). An AC voltage of 3 V was used for a frequency sweep from 10^{-1} to 10^{5} Hz and 10 points per decade. An integration time of 10 s was used for higher frequency range i.e. 1 Mhz to 1 Hz, while for low frequency measurements i.e. 1 to 0.1 Hz an average vaule of 10 cycles was used as final measurements. Temperature dependent cryostat measurements were performed for a temperature range of -160 °C to 160 °C. Liqiud nitrogen was used for the cooling process. Before the cooling process the sample chamber was vacuumed and purged with helium gas.

OMICRON Analyser Suit was used for measurements performed with OMICRON Spectano 100. An AC voltage of 12 V was used for a frequency sweep from 10^{-4} to 5×10^{3} Hz and 8 points per decade with an integration time of 10 s. The equipment uses a combination of two different methods for dielectric measurements which depend upon specified frequency range. For frequencies ≥ 100 mHz, frequency domain analysis (FDS) method is used whereas for frequencies <100 mHz polarising-depolarising current (PDC) method is used. These two methods were also tested independently for the entire frequency range of 10^{-4} to 5×10^{3} Hz to check for any differences. However, no significant differences in the data were observed.

The working principle of the dielectric spectroscopy equipment depends upon the calculation of the complex impedance. The complex impedance is calculate with the help of two know voltage measurements which are measured across the sample and an internal reference resistance connected in series with the sample and with second voltage measurement taken across only the internal reference resistance. Hence, the voltage across the sample can be calculate by voltage division rule (Fig. A.2). Further, an ammeter measures the current flowing through the circuit. From these measurements of current and voltages in accordance to ohms law resistance can be calculated. Since the voltage is frequency dependent there exists a phase angle, therefore complex impedance is now calculate from the now known resistance. Finally, by using equation A.1 the complex permittivity can then be calculate as follows,

$$Z_s^*(\omega) = \frac{V_s}{I_s} = R\,\frac{V_1(\omega) - V_2(\omega)}{V_2(\omega)} - 1 \tag{A.1}$$

$$\varepsilon^* = \frac{-i}{\omega Z^*(\omega) C_0} \tag{A.2}$$

where $\omega = 2\pi f$, Z^* is the complex impedance, R is the resistance and V is the voltage.

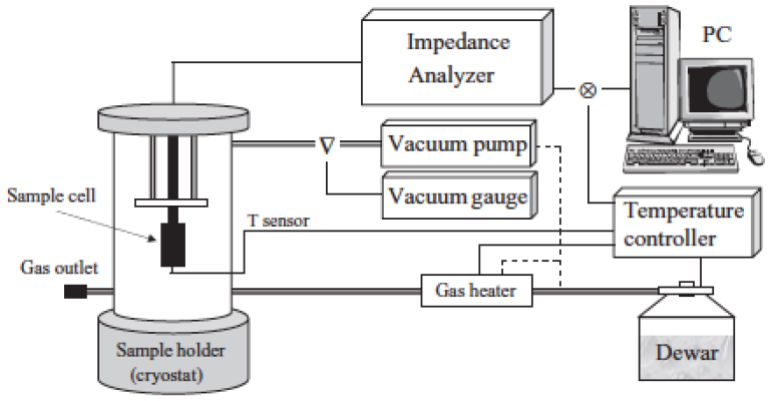

FIGURE A.1: Schematic diagram for dielectric spectroscopy measurement equipment connections.

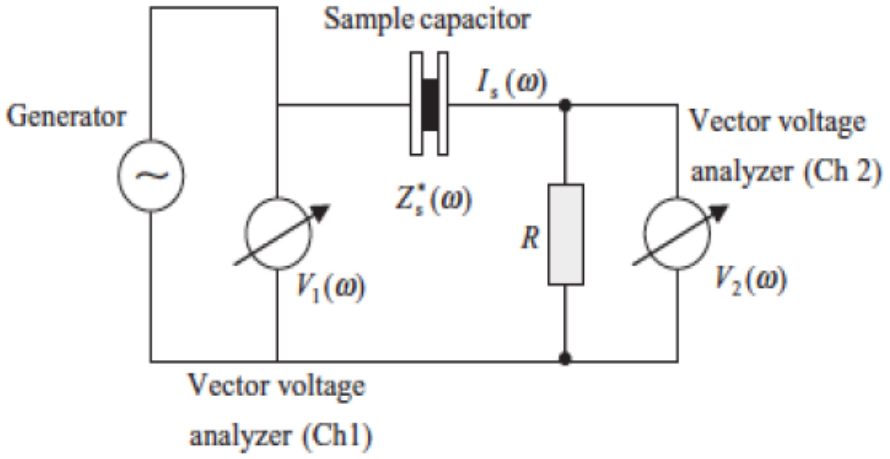

FIGURE A.2: Circuit diagram for Solartron 1296

A.2 Differential Scanning Calorimetry

Differential scanning calorimetry is used to characterise the thermal properties of the sample. It can be used to calculate the heat capacity and the glass transition temperature of the sample. A Perkin Elmer DSC7 differential scanning calorimetry (DSC) was used to evaluate the glass transition of the studied samples. The software package used for the control and calibration was Pyris. The working principle of the equipment is based on the idea where two material are subjected to same heating procedure and then the difference between the heat flows is calculated to find the heat capacity change (Fig. A.3). One of the sample which is the reference has already know thermal properties, in this case empty reference pan is used. The equipment is initially calibrated using a separate material with known thermal properties to avoid any form of deviation during the actual measurement. For calibration a 6.85 mg of high purity indium with known melting temperature of 156.6 °C was used alongside an empty reference. A mass of 12 mg - 15 mg enclosed in aluminium cans of mass $\simeq 23.5 \pm 0.2$ mg was used for the measurement of the samples. The heating

cycle used is as follows,

1. Hold for 5 min at 25 °C.
2. Heat from 25 °C to 170 °C at 10 °C min^{-1}.
3. Hold at 170 °C for 2 min.
4. Cool from 170 °C to 25 °C at 10 °C min^{-1}.
5. Hold at 25 °C for 5 min.
6. Heat from 25 °C to 170 °C at 10 °C min^{-1}.

Two step heating cycle was used where the first cycle was used to clear any thermal history of the sample. The samples are held at certain temperature to allow them to reach thermal equilibrium or steady state. The heating and cooling rate was maintained the same throughout the process to avoid any deviated segmental motions due to its difference. Inflection point method was used to evaluate the Tg from the heating curve.

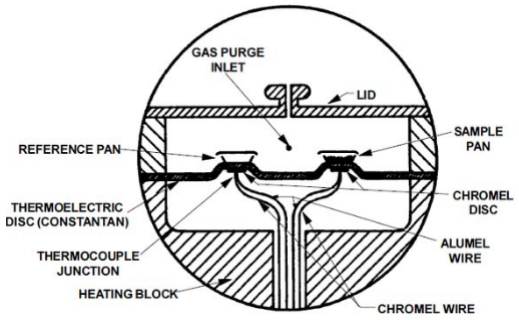

FIGURE A.3: Schematic diagram representing the cross section a DSC test cell.

A.3 Fourier Transform Infra-Red Spectroscopy

ATR-FTIR iD7 Nicolet iS5 spectrometer from ThermoFisher Scientific was used to perform the FTIR-ATR measurements. The angle of indecent of the equipment is 45°. The crystal type used was uncoated diamond having a sampling area of 1.8 mm and single bounce internal reflection. ASTM E1412 standard was followed to measure the data with the help of deuterated triglycine sulfate (DTGS) detector type. The infra-red beam was produced using a temperature controlled solid state diode laser. The data was measured for a wavelength range of 4000 cm^{-1} to 500 cm^{-1}. The measurements were performed both directly on the different type of nanoparticles and filled epoxy nanocomposites. For each sample the measurement was performed three times, on three different location in-case of epoxy nanocomposites. The sample holder was cleaned with ethanol and single beam background spectrum was recorded before every measurement. Since, a diamond crystal type was used the signal to noise ratio between 2600 cm^{-1} and 1700 cm^{-1} is reduced due to the presence of diamond phonon bands.

The working principle of FTIR relies on the interference of various frequencies of light to collect a spectrum. The spectrometer consists of a source, beamsplitter, two mirrors, a laser

and a detector; the beamsplitter and mirrors are collectively called the interferometer (Fig. A.4). The IR light from the source strikes the beamsplitter, which produces two beams of same intensity. One beam strikes a fixed mirror and returns. The second strikes a moving mirror. The moving mirror oscillates at a constant velocity which timed as a fucntion of the laser frequency. The two beams are reflected from the mirrors and are recombined at the beamsplitter. If the distance the two beams travel is the same, then they will recombine constructively. However, if the beam from the moving mirror has travelled a different distance than the beam from the fixed mirror the recombination will result in destructive interference. The beam then passes through the sample where some of the energy is absorbed and the rest is transmitted.

The detector then records the response. Since, this interferogram represents the interference pattern as a function of the source, beamsplitter, mirrors and sample, the background spectrum recorded earlier is used in a Fourier transform algorithm that removes the effect of all the different components of the equipment and a transmittance spectrum of the sample is presented. However, the data is presented in absorbance mode. Absorbance (A) is the logarithm to the base 10 of the reciprocal of the transmittance (T) (Eq. A.3)

$$A = log_{10}\frac{1}{T} = -log_{10}T = -log_{10}\frac{I}{I_0} \tag{A.3}$$

where I is the radiant power transmitted by the sample and I_0 is the power indecent on it.

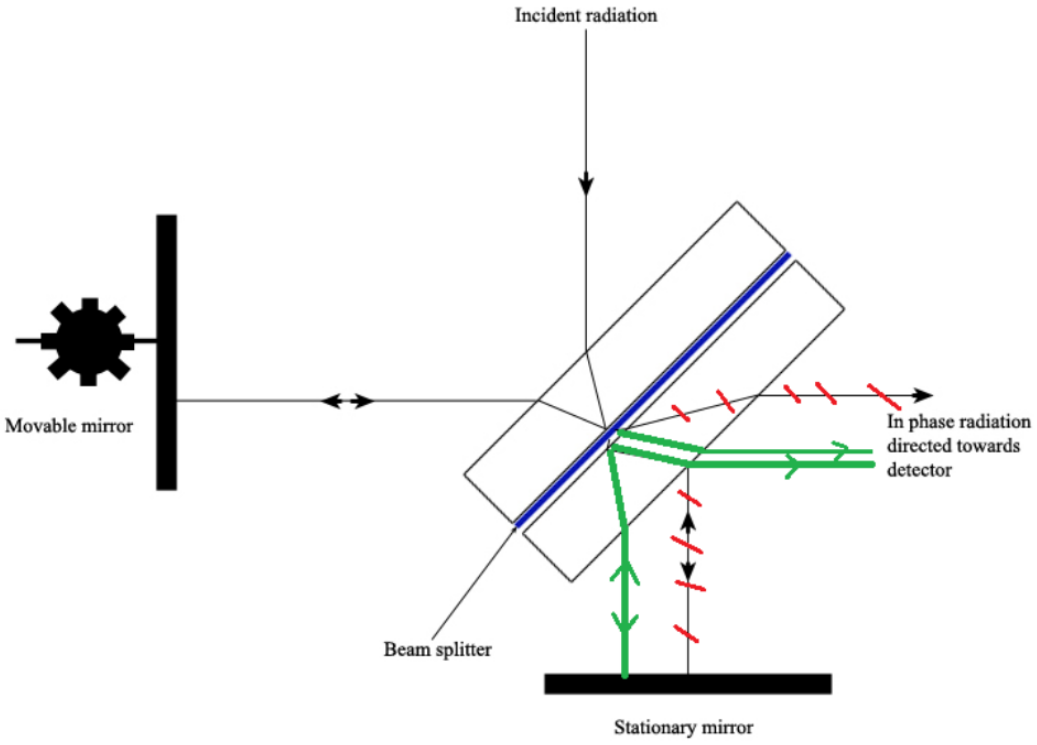

FIGURE A.4: Schematic diagram of a FTIR spectrometer

A.4 Transmission Electron Microscopy

The morphology characterization of the nanocomposite samples was done with transmission electron microscopy (TEM). The system used was Hitachi H 7000 transmission electron microscope under high resolution mode as well as high contrast mode. Fig. A.5 shows the schematic diagram of TEM and Fig A.6 shows the different components inside a TEM. The microscope operated at an applied voltage of 100 kV under -5kPa vacuum pressure. The TEM usually operates under vacuum to increases the mean free path length of the electrons by reducing the frequency of collision and to allow the voltage difference between the ground and high voltage electron without arcing. A lanthanum hexaboride crystal was used as source of electron. The samples were cut into thin slices of $\simeq$ 90 nm using an Reichert Om-U3 ultramicrotome with the help of a glass knife 45°. These thin sample slices were mounted onto a square meshed grid. The diameter of the grid was 3.05 mm with a thickness of 20 μm having 200 mesh. The grid was made up of copper and coated with palladium on one side for better grid strength, to avoid tarnishing and to visually differentiate between both sides. Prior to mounting the sample, the grids were coated with a carbon film of 5 - 6 nm thickness to have better electrical and heat conduction in the electron beam.

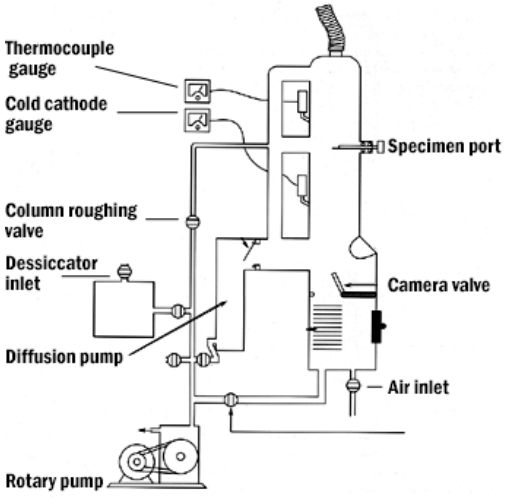

FIGURE A.5: Schematic diagram of transmission electron microscope (TEM)

A.5 Dynamic Mechanical Analysis

For DMA, a Mettler Toledo DMA/SDTA861 was employed. This equipment was used in tension mode with a maximum force of 10 N or 3 μm maximum level and a 150% auto offset. Measurements were taken in isothermal steps of 10 °C, for a temperature range of -100 °C to 160 °C and a frequency sweep of 10^{-3} Hz to 10^{2} Hz.

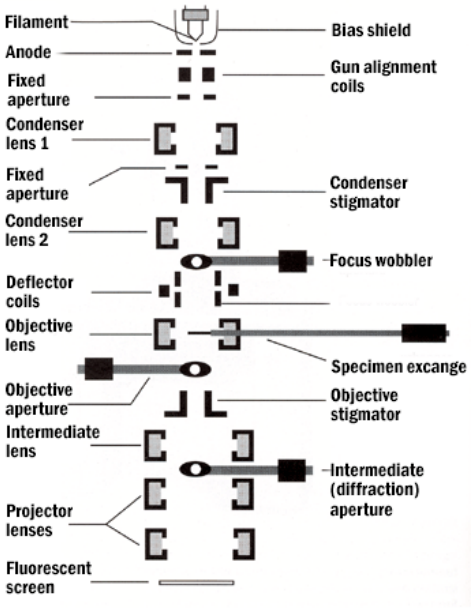

FIGURE A.6: Different components inside the transmission electron microscope (TEM)

Appendix B

MATLAB: Havriliak - Negami Analysis Plugin

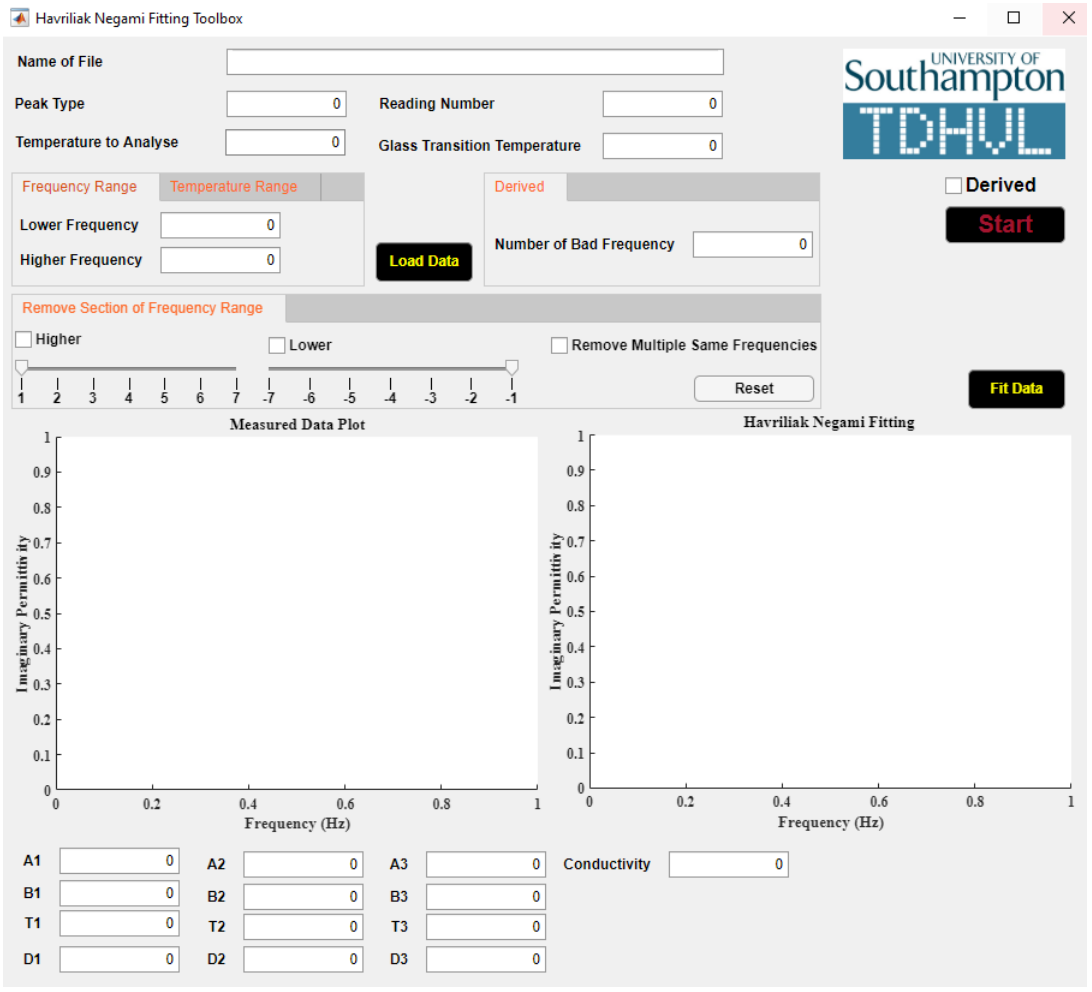

FIGURE B.1: GUI of the Havriliak - Negami analysis plugin

In order to maintain consistency between the α and β parameters of the HN fitting with varying temperature a MATLAB plugin was developed. The code uses an iterative approach

to calculate the HN - parameters. Once a curve is measured by the user and is confirmed to have the appropriate and desired fit, the fitting at all other temperature will keep track of all the previous fit to maintain the consistency across the parameters and provide the best possible fit under these conditions. Simultaneously, only there relaxation peaks can be deconvoluted at the moment. However, it can be developed further.

References

[1] T. J. Lewis, "Nanometric Dielectrics," *IEEE Transactions on Dielectrics and Electrical Insulation*, vol. 1, no. 5, pp. 812–825, 1994.

[2] M. F. Fréchette, M. L. Trudeau, H. D. Alamdari, and S. Boily, "Introductory remarks on nanodielectrics," in *IEEE Transactions on Dielectrics and Electrical Insulation*, vol. 11, no. 5, oct 2004, pp. 808–818.

[3] J. K. Nelson, J. C. Fothergill, L. A. Dissado, and W. Peasgood, "Towards an understanding of nanometric dielectrics," in *Conference on Electrical Insulation and Dielectric Phenomena (CEIDP), Annual Report*, 2002, pp. 295–298.

[4] "EUR-Lex - 32011H0696 - EN - EUR-Lex." [Online]. Available: https://eur-lex.europa.eu/legal-content/EN/TXT/?uri=CELEX:32011H0696

[5] M. F. Fréchette, A. Vijh, L. Utracki, M. L. Trudeau, A. Sami, C. Laurent, P. Morshuis, T. Andritsch, R. Kochetov, A. Vaughan, É. David, J. Castellon, D. Fabiani, S. Gubanski, J. Kindersberger, C. Reed, A. Krivda, J. Fothergill, S. Dodd, F. Guastavino, and H. Alamdari, "Nanodielectrics: A panacea for solving all electrical insulation problems?" in *Proceedings of the 2010 IEEE International Conference on Solid Dielectrics, ICSD 2010*. IEEE Computer Society, 2010.

[6] K. Y. Lau, A. S. Vaughan, and G. Chen, "Nanodielectrics: Opportunities and challenges," *IEEE Electrical Insulation Magazine*, vol. 31, no. 4, pp. 45–54, jul 2015.

[7] S. Li, G. Yin, G. Chen, J. Li, S. Bai, L. Zhong, Y. Zhang, and Q. Lei, "Short-term breakdown and long-term failure in nanodielectrics: A review," *IEEE Transactions on Dielectrics and Electrical Insulation*, vol. 17, no. 5, pp. 1523–1535, oct 2010.

[8] A. Henglein, "Small-Particle Research: Physicochemical Properties of Extremely Small Colloidal Metal and Semiconductor Particles," *Chemical Reviews*, vol. 89, no. 8, pp. 1861–1873, 1989. [Online]. Available: https://pubs.acs.org/sharingguidelines

[9] H. C. Youn, S. Baral, and J. H. Fendler, "Dihexadecyl phosphate, vesicle-stabilized and in situ generated mixed cadmium sulfide and zinc sulfide semiconductor particles: preparation and utilization for photosensitized charge separation and hydrogen generation," *The Journal of Physical Chemistry*, vol. 92, no. 22, pp. 6320–6327, nov 1988. [Online]. Available: https://pubs.acs.org/doi/abs/10.1021/j100333a029

[10] F. Scandola and M. T. Indelli, "Photoinduced Electron and Energy Transfer in Covalently Linked Supramolecular Systems," in *Photochemical Conversion and Storage of Solar Energy*. Springer Netherlands, 1991, pp. 1–14.

[11] R. Ghosh Chaudhuri and S. Paria, "Core/shell nanoparticles: Classes, properties, synthesis mechanisms, characterization, and applications," pp. 2373–2433, apr 2012.

[12] X. Chen, D. Peng, Q. Ju, and F. Wang, "Photon upconversion in core-shell nanoparticles," pp. 1318–1330, mar 2015. [Online]. Available: www.rsc.org/csr

[13] F. N. Alhabill, R. Ayoob, T. Andritsch, and A. S. Vaughan, "Introducing particle interphase model for describing the electrical behaviour of nanodielectrics," *Materials and Design*, vol. 158, pp. 62–73, nov 2018.

[14] V. Varshney, S. S. Patnaik, A. K. Roy, and B. L. Farmer, "A molecular dynamics study of epoxy-based networks: Cross-linking procedure and prediction of molecular and material properties," *Macromolecules*, vol. 41, no. 18, pp. 6837–6842, sep 2008.

[15] A. Bajpai and S. Carlotti, "The Effect of Hybridized Carbon Nanotubes, Silica Nanoparticles, and Core-Shell Rubber on Tensile, Fracture Mechanics and Electrical Properties of Epoxy Nanocomposites," *Nanomaterials*, vol. 9, no. 7, p. 1057, jul 2019. [Online]. Available: https://www.mdpi.com/2079-4991/9/7/1057

[16] "EPOXIES AT A GLANCE EPOXY RESIN COMMITTEE Who invented epoxies and why?" [Online]. Available: www.epoxy-europe.eu

[17] E. E. Woods, "Cast epoxy insulation for high voltage switchgear and power transformers," in *5th EI Electrical Insulation Conference Materials and Application, EIC 1963*. Institute of Electrical and Electronics Engineers Inc., apr 2016, pp. 265–267.

[18] G. C. Stone, R. G. Van Heeswijk, and R. Bartnikas, "Investigation of the effect of repetitive voltage surges on epoxy insulation," *IEEE Transactions on Energy Conversion*, vol. 7, no. 4, pp. 754–760, 1992.

[19] S. Singha and M. J. Thomas, "Dielectric properties of epoxy nanocomposites," *IEEE Transactions on Dielectrics and Electrical Insulation*, vol. 15, no. 1, pp. 12–23, feb 2008.

[20] Q. Wang, G. Chen, and A. S. Alghamdi, "Influence of nanofillers on electrical characteristics of epoxy resins insulation," in *Proceedings of the 2010 IEEE International Conference on Solid Dielectrics, ICSD 2010*, 2010.

[21] R. Kochetov, T. Andritsch, P. H. Morshuis, and J. J. Smit, "Dielectric response and thermal conductivity of epoxy resin filled with nanoalumina particles of different size in α, γ and δ phase," in *Annual Report - Conference on Electrical Insulation and Dielectric Phenomena, CEIDP*, 2010.

[22] V. Nguyen, A. Vaughan, P. Lewin, and A. Krivda, "The effect of resin stoichiometry and nanoparticle addition on epoxy/silica nanodielectrics," *IEEE Transactions on Dielectrics and Electrical Insulation*, vol. 22, no. 2, pp. 895–905, apr 2015.

[23] G. Iyer, R. S. Gorur, R. Richert, A. Krivda, and L. E. Schmidt, "Dielectric properties of epoxy based nanocomposites for high voltage insulation," *IEEE Transactions on Dielectrics and Electrical Insulation*, vol. 18, no. 3, pp. 659–666, jun 2011.

[24] M. Reading, Z. Xu, A. S. Vaughan, and P. L. Lewin, "On sample preparation and dielectric breakdown in nanostructured epoxy resins," in *Journal of Physics: Conference Series*, vol. 310, no. 1. Institute of Physics Publishing, aug 2011, p. 12009. [Online]. Available: https://iopscience.iop.org/article/10.1088/1742-6596/310/1/012009https://iopscience.iop.org/article/10.1088/1742-6596/310/1/012009/meta

[25] C. Zou, J. C. Fothergill, and S. W. Rowe, "The effect of water absorption on the dielectric properties of epoxy nanocomposites," *IEEE Transactions on Dielectrics and Electrical Insulation*, vol. 15, no. 1, pp. 106–117, feb 2008.

[26] C. Yeung and A. S. Vaughan, "A study of how varying degrees of functionalised nanofiller have an effect on nanodielectrics," in *Annual Report - Conference on Electrical Insulation and Dielectric Phenomena, CEIDP*, 2012, pp. 319–322.

[27] M. Fréchette, I. Preda, J. Castellon, A. Krivda, R. Veillette, M. Trudeau, and E. David, "Polymer composites with a large nanofiller content: A case study involving epoxy," *IEEE Transactions on Dielectrics and Electrical Insulation*, vol. 21, no. 2, 2014.

[28] A. S. T. M. E2456-06, *American Society for Testing and Materials International Committee E56 on Nanotechnology*, astm e2456 ed. West Conshohocken, PA: ASTM International, 2012, vol. West Consh. [Online]. Available: www.astm.org

[29] A. Ulu, I. Ozcan, S. Koytepe, and B. Ates, "Design of epoxy-functionalized Fe3O4@MCM-41 core–shell nanoparticles for enzyme immobilization," *International Journal of Biological Macromolecules*, vol. 115, pp. 1122–1130, aug 2018.

[30] S. Liu, X. Fan, and C. He, "Improving the fracture toughness of epoxy with nanosilica-rubber core-shell nanoparticles," *Composites Science and Technology*, vol. 125, pp. 132–140, mar 2016.

[31] G. Giannakopoulos, K. Masania, and A. C. Taylor, "Toughening of epoxy using core-shell particles," *Journal of Materials Science*, vol. 46, no. 2, pp. 327–338, jan 2011. [Online]. Available: https://link.springer.com/article/10.1007/s10853-010-4816-6

[32] Y. Shen, Y. Lin, and C. W. Nan, "Interfacial effect on dielectric properties of polymer nanocomposites filled with core/shell-structured particles," *Advanced Functional Materials*, vol. 17, no. 14, pp. 2405–2410, sep 2007. [Online]. Available: https://onlinelibrary.wiley.com/doi/full/10.1002/adfm.200700200https://onlinelibrary.wiley.com/doi/abs/10.1002/adfm.200700200https://onlinelibrary.wiley.com/doi/10.1002/adfm.200700200

[33] Z. Wang, M. Yang, Y. Cheng, J. Liu, B. Xiao, S. Chen, J. Huang, Q. Xie, G. Wu, and H. Wu, "Dielectric properties and thermal conductivity of epoxy composites using quantum-sized silver decorated core/shell structured alumina/polydopamine," *Composites Part A: Applied Science and Manufacturing*, vol. 118, pp. 302–311, mar 2019.

[34] I. A. Tsekmes, R. Kochetov, P. H. Morshuis, and J. J. Smit, "AC breakdown strength of epoxy-boron nitride nanocomposites: Trend & Reproducibility," in *33rd Electrical Insulation Conference, EIC 2015*. Institute of Electrical and Electronics Engineers Inc., 2014, pp. 446–449.

[35] M. Donnay, S. Tzavalas, and E. Logakis, "Boron nitride filled epoxy with improved thermal conductivity and dielectric breakdown strength," *Composites Science and Technology*, vol. 110, pp. 152–158, apr 2015.

[36] Z. Li, K. Okamoto, Y. Ohki, and T. Tanaka, "Role of nano-filler on partial discharge resistance and dielectric breakdown strength of micro-Al2O3/epoxy composites," in *Proceedings of the IEEE International Conference on Properties and Applications of Dielectric Materials*, nov 2009, pp. 753–756. [Online]. Available: https://waseda.pure.elsevier.com/en/publications/role-of-nano-filler-on-partial-discharge-resistance-and-dielectri

[37] J. Song, H. Han, B. Peng, Y. Hu, Q. Cui, Z. Lou, Y. Hou, and F. Teng, "Role of nanoparticle surface defects in the conduction mechanism of polymer-nanoparticle electrical bistable devices," *RSC Advances*, vol. 7, no. 85, pp. 54 128–54 135, nov 2017. [Online]. Available: https://pubs.rsc.org/en/content/articlehtml/2017/ra/c7ra11879ahttps://pubs.rsc.org/en/content/articlelanding/2017/ra/c7ra11879a

[38] E. Marino, T. E. Kodger, R. W. Crisp, D. Timmerman, K. E. MacArthur, M. Heggen, and P. Schall, "Repairing Nanoparticle Surface Defects," *Angewandte Chemie International Edition*, vol. 56, no. 44, pp. 13 795–13 799, oct 2017. [Online]. Available: http://doi.wiley.com/10.1002/anie.201705685

[39] J. K. Nelson and J. C. Fothergill, "Internal charge behaviour of nanocomposites," *Nanotechnology*, vol. 15, no. 5, pp. 586–595, may 2004.

[40] P. Maity, P. K. Poovamma, S. Basu, V. Parameswaran, and N. Gupta, "Dielectric spectroscopy of epoxy resin with and without nanometric alumina fillers," *IEEE Transactions on Dielectrics and Electrical Insulation*, vol. 16, no. 5, pp. 1481–1488, oct 2009.

[41] Y. Sun, Z. Zhang, and C. P. Wong, "Influence of interphase and moisture on the dielectric spectroscopy of epoxy/silica composites," *Polymer*, vol. 46, no. 7, pp. 2297–2305, mar 2005.

[42] G. Iyer, R. S. Gorur, R. Richert, A. Krivda, and L. E. Schmidt, "Dielectric properties of epoxy based nanocomposites for high voltage insulation," *IEEE Transactions on Dielectrics and Electrical Insulation*, vol. 18, no. 3, pp. 659–666, jun 2011.

[43] A. Chatterjee and M. S. Islam, "Fabrication and characterization of TiO2-epoxy nanocomposite," *Materials Science and Engineering A*, vol. 487, no. 1-2, pp. 574–585, jul 2008.

[44] T. V. Kosmidou, A. S. Vatalis, C. G. Delides, E. Logakis, P. Pissis, and G. C. Papanicolaou, "Structural, mechanical and electrical characterization of epoxy-amine/carbon black nanonocomposites," *Express Polymer Letters*, vol. 2, no. 5, pp. 364–372, may 2008.

[45] Y. Sun, Z. Zhang, K. S. Moon, and C. P. Wong, "Glass transition and relaxation behavior of epoxy nanocomposites," *Journal of Polymer Science, Part B: Polymer Physics*, vol. 42, no. 21, pp. 3849–3858, nov 2004. [Online]. Available: https://onlinelibrary.wiley.com/doi/full/10.1002/polb.20251

[46] I. A. Saeedi, A. S. Vaughan, T. Andritsch, and S. Virtanen, "The effect of curing conditions on the electrical properties of an epoxy resin," in *Annual Report - Conference on Electrical Insulation and Dielectric Phenomena, CEIDP*, vol. 2016-Decem. Institute of Electrical and Electronics Engineers Inc., dec 2016, pp. 461–464.

[47] R. Sabater I Serra, C. Torregrosa-Cabanilles, J. M. Meseguer-Dueñas, J. L. Gómez Ribelles, and J. Molina-Mateo, "Conformation and segmental mobility of a diluted single polymer chain simulated with bond fluctuation model," *Journal of Non-Crystalline Solids*, vol. 358, no. 12-13, pp. 1452–1458, jul 2012.

[48] C. K. Hall and E. Helfand, "Conformational state relaxation in polymers: Time-correlation functions," *The Journal of Chemical Physics*, vol. 77, no. 6, pp. 3275–3282, sep 1982. [Online]. Available: http://aip.scitation.org/doi/10.1063/1.444204

[49] J. Skolnick and R. Yaris, "Damped Orientational Diffusion Model of Polymer Local Main-Chain Motion. 1. General Theory," *Macromolecules*, vol. 15, no. 4, pp. 1041–1046, 1982. [Online]. Available: https://pubs.acs.org/sharingguidelines

[50] Y. Shangguan, F. Chen, E. Jia, Y. Lin, J. Hu, and Q. Zheng, "New insight into Time-Temperature correlation for polymer relaxations ranging from secondary relaxation to terminal flow: Application of a Universal and developed WLF equation," *Polymers*, vol. 9, no. 11, nov 2017. [Online]. Available: /pmc/articles/PMC6418538/?report=abstracthttps://www.ncbi.nlm.nih.gov/pmc/articles/PMC6418538/

[51] M. L. Williams, R. F. Landel, and J. D. Ferry, "The Temperature Dependence of Relaxation Mechanisms in Amorphous Polymers and Other Glass-forming Liquids," *Journal of the American Chemical Society*, vol. 77, no. 14, pp. 3701–3707, 1955. [Online]. Available: https://pubs.acs.org/sharingguidelines

[52] M. Paluch, J. Zioło, and S. J. Rzoska, "Dielectric relaxation of glass-forming epoxy resin under high pressure," *Physical Review E - Statistical Physics, Plasmas, Fluids, and Related Interdisciplinary Topics*, vol. 56, no. 5, pp. 5764–5767, nov 1997.

[53] A. Schönhals, "Molecular Dynamics in Polymer Model Systems," in *Broadband Dielectric Spectroscopy*. Springer Berlin Heidelberg, 2003, pp. 225–293.

[54] M. K. Hassan, S. J. Tucker, A. Abukmail, J. S. Wiggins, and K. A. Mauritz, "Polymer chain dynamics in epoxy based composites as investigated by broadband dielectric spectroscopy," *Arabian Journal of Chemistry*, vol. 9, no. 2, pp. 305–315, mar 2016.

[55] M. J. Pulikkathumbayil and G. Govindaraj, "Unusual combination of conduction and dielectric relaxations in nanocrystalline α – $Fe2O3$," *Materials Letters*, vol.264, p.127314, apr2020.

[56] R. D. Andrews and T. J. Hammack, "The theoretical interpretation of dynamic mechanicl loss spectra and transition temperatures," *Journal of Polymer Science Part B: Polymer Letters*, vol. 3, no. 8, pp. 655–657, aug 1965.

[57] N. Shito and M. Sato, "Electrical and mechanical properties of anhydride-cured epoxy resins," *Journal of Polymer Science Part C: Polymer Symposia*, vol. 16, no. 2, pp. 1069–1078, mar 2007.

[58] E. Hempel, M. Beiner, T. Renner, and E. Donth, "Linearity of heat capacity step near the onset of a glass transition in poly(w-alkylmethacrylate)s," *Acta Polymerica*, vol. 47, no. 1112, pp. 525–529, nov 1996.

[59] C. P. Johari and M. Goidstein, "Viscous liquids and the glass transition. II. Secondary relaxations in glasses of rigid molecules," *The Journal of Chemical Physics*, vol. 53, no. 6, pp. 2372–2388, sep 1970. [Online]. Available: http://aip.scitation.org/doi/10.1063/1.1674335

[60] A. S. Kulik, H. W. Beckham, K. Schmidt-Rohr, D. Radloff, U. Pawelzik, C. Boeffel, and H. W. Spiess, "Coupling of α and β Processes in Poly(ethyl methacrylate) Investigated by Multidimensional NMR," *Macromolecules*, vol. 27, no. 17, pp. 4746–4754, aug 1994. [Online]. Available: https://pubs.acs.org/sharingguidelines

[61] F. R. Dammont and T. K. Kwei, "Dynamic mechanical properties of aromatic, aliphatic, and partially fluorinated epoxy resins," *Journal of Polymer Science Part A-2: Polymer Physics*, vol. 5, no. 4, pp. 761–769, jul 1967.

[62] R. Ding, S. W. Torres, J. Messman, D. E. Bowen, and N. Bowler, "Dynamics of model polycyclic aromatic hydrocarbon compound-epoxy composites: A dielectric study," *Polymer*, vol. 136, pp. 6–16, jan 2018.

[63] E. CUDDIHY and J. MOACANIN, "Dynamic Mechanical Properties of Epoxies' β-Transition Mechanism," jun 1970, pp. 96–107. [Online]. Available: https://pubs.acs.org/doi/abs/10.1021/ba-1970-0092.ch009

[64] L. Heux, J. L. Halary, F. Lauprêtre, and L. Monnerie, "Dynamic mechanical and 13C n.m.r. investigations of molecular motions involved in the β relaxation of epoxy networks based on DGEBA and aliphatic amines," *Polymer*, vol. 38, no. 8, pp. 1767–1778, apr 1997.

[65] H. Van Hoorn, "A dynamic mechanical study of the effect of chemical variations on the internal mobility of linear epoxy resins (polyhydroxyethers)," *Journal of Applied Polymer Science*, vol. 12, no. 4, pp. 871–888, apr 1968. [Online]. Available: http://doi.wiley.com/10.1002/app.1968.070120422

[66] A. Soulintzis, G. Kontos, P. Karahaliou, G. C. Psarras, S. N. Georga, and C. A. Krontiras, "Dielectric relaxation processes in epoxy resin-ZnO composites," *Journal of Polymer Science Part B: Polymer Physics*, vol. 47, no. 4, pp. 445–454, feb 2009. [Online]. Available: http://doi.wiley.com/10.1002/polb.21649

[67] W. Jilani, N. Mzabi, N. Fourati, C. Zerrouki, O. Gallot-Lavallée, R. Zerrouki, and H. Guermazi, "A comparative study of structural and dielectric properties of diglycidyl ether of bisphenol A (DGEBA) cured with aromatic or aliphatic hardeners," *Journal of Materials Science*, vol. 51, no. 17, pp. 7874–7886, sep 2016. [Online]. Available: https://link.springer.com/article/10.1007/s10853-016-0043-0

[68] M. Ochi, M. Okazaki, and M. Shimbo, "Mechanical relaxation mechanism of epoxide resins cured with aliphatic diamines," *Journal of Polymer Science: Polymer Physics Edition*, vol. 20, no. 4, pp. 689–699, apr 1982. [Online]. Available: http://doi.wiley.com/10.1002/pol.1982.180200411

[69] M. Ochi, M. Shimbo, M. Saga, and N. Takashima, "Mechanical and dielectric relaxations of epoxide resins containing spiro-ring structure," *Journal of Polymer Science Part B: Polymer Physics*, vol. 24, no. 10, pp. 2185–2195, oct 1986.

[70] M. Ochi, H. Iesako, and M. Shimbo, "Relaxation mechanism of epoxide resin cured with acid anhydrides. III. Effect of alkyl side chains on mechanical and dielectric β relaxations," *Journal of Polymer Science Part B: Polymer Physics*, vol. 24, no. 6, pp. 1271–1282, jun 1986.

[71] M. Ochi, M. Yoshizumi, and M. Shimbo, "Mechanical and dielectric relaxations of epoxide resins containing the spiro-ring structure. II. Effect of the introduction of methoxy branches on low-temperature relaxations of epoxide resins," *Journal of Polymer Science Part B: Polymer Physics*, vol. 25, no. 9, pp. 1817–1827, sep 1987.

[72] M. B. Mangion and G. P. Johari, "Relaxations of thermosets. III. Sub-Tg dielectric relaxations of bisphenol-A–based epoxide cured with different cross-linking agents," *Journal of Polymer Science Part B: Polymer Physics*, vol. 28, no. 1, pp. 71–83, jan 1990.

[73] J. M. Charlesworth, "Effect of crosslink density on molecular relaxations in diepoxide-diamine network polymers. Part 2. The rubbery plateau region," *Polymer Engineering and Science*, vol. 28, no. 4, pp. 230–236, feb 1988.

[74] G. A. Pogany, "Gamma relaxation in epoxy resins and related polymers," *Polymer*, vol. 11, no. 2, pp. 66–78, feb 1970.

[75] T. Hirai and D. E. Kline, "Dynamic mechanical properties of nonstoichiometric, amine-cured epoxy resin," *Journal of Applied Polymer Science*, vol. 16, no. 12, pp. 3145–3157, dec 1972.

[76] G. Tsagaropoulos and A. Eisenberg, "Dynamic Mechanical Study of the Factors Affecting the Two Glass Transition Behavior of Filled Polymers. Similarities and Differences with Random Ionomers," *Macromolecules*, vol. 28, no. 18, pp. 6067–6077, aug 1995. [Online]. Available: https://pubs.acs.org/sharingguidelines

[77] V. Tomer, G. Polizos, C. A. Randall, and E. Manias, "Polyethylene nanocomposite dielectrics: Implications of nanofiller orientation on high field properties and energy storage," in *Journal of Applied Physics*, vol. 109, no. 7. American Institute of PhysicsAIP, apr 2011, p. 074113. [Online]. Available: http://aip.scitation.org/doi/10.1063/1.3569696

[78] H. Ribeiro, J. P. C. Trigueiro, M. C. Lopes, J. J. Pedrotti, C. F. Woellner, W. M. Silva, G. G. Silva, and P. M. Ajayan, "Enhanced thermal conductivity and mechanical properties of hybrid MoS ₂ /h-BN polyurethane nanocomposites," *Journal of Applied Polymer Science*, vol. 135, no. 30, p. 46560, aug 2018. [Online]. Available: http://doi.wiley.com/10.1002/app.46560

[79] L. S. Schadler, L. C. Brinson, and W. G. Sawyer, "Polymer nanocomposites: A small part of the story," pp. 53–60, mar 2007. [Online]. Available: https://link.springer.com/article/10.1007/s11837-007-0040-5

[80] T. Tanaka, M. Kozako, N. Fuse, and Y. Ohki, "Proposal of a multi-core model for polymer nanocomposite dielectrics," *IEEE Transactions on Dielectrics and Electrical Insulation*, vol. 12, no. 4, pp. 669–681, aug 2005.

[81] M. Roy, J. K. Nelson, R. K. MacCrone, L. S. Schadler, C. W. Reed, R. Keefe, and W. Zenger, "Polymer nanocomposite dielectrics - The role of the interface," *IEEE Transactions on Dielectrics and Electrical Insulation*, vol. 12, no. 4, pp. 629–642, aug 2005.

[82] T. Desai, P. Keblinski, and S. K. Kumar, "Molecular dynamics simulations of polymer transport in nanocomposites," *Journal of Chemical Physics*, vol. 122, no. 13, p. 134910, apr 2005.

[83] H. Lu and S. Nutt, "Restricted relaxation in polymer nanocomposites near the glass transition," *Macromolecules*, vol. 36, no. 11, pp. 4010–4016, jun 2003.

[84] T. Tanaka, G. C. Montanari, and R. Mülhaupt, "Polymer nanocomposites as dielectrics and electrical insulation- perspectives for processing technologies, material characterization and future applications," in *IEEE Transactions on Dielectrics and Electrical Insulation*, vol. 11, no. 5, oct 2004, pp. 763–784.

[85] J. K. Nelson and Y. Hu, "Nanocomposite dielectrics - Properties and implications," in *Journal of Physics D: Applied Physics*, vol. 38, no. 2. IOP Publishing, jan 2005, pp. 213–222. [Online]. Available: https://iopscience.iop.org/article/10.1088/0022-3727/38/2/005https://iopscience.iop.org/article/10.1088/0022-3727/38/2/005/meta

[86] Y. Li, D. Lu, and C. P. Wong, *Electrical conductive adhesives with nanotechnologies*. Springer US, 2010.

[87] A. Schönhals, H. Goering, F. R. Costa, U. Wagenknecht, and G. Heinrich, "Dielectric properties of nanocomposites based on polyethylene and layered double hydroxide," *Macromolecules*, vol. 42, no. 12, pp. 4165–4174, jun 2009. [Online]. Available: https://pubs.acs.org/sharingguidelines

[88] C. Kenyó, J. Hári, K. Renner, C. Kröhnke, and B. Pukánszky, "Effect of matrix characteristics on the properties of high-impact polystyrene/zeolite functional packaging materials," *Industrial and Engineering Chemistry Research*, vol. 53, no. 49, pp. 19 208–19 215, dec 2014. [Online]. Available: https://pubs.acs.org/sharingguidelines

[89] J.-P. Qu, Z.-T. Yang, X.-C. Yin, H.-Z. He, and Y.-H. Feng, "Characteristics Study of Polymer Melt Conveying Capacity in Vane Plasticization Extruder," *Polymer-Plastics Technology and Engineering*, vol. 48, no. 12, pp. 1269–1274, nov 2009. [Online]. Available: http://www.tandfonline.com/doi/abs/10.1080/03602550903204121

[90] P. Barber, S. Balasubramanian, Y. Anguchamy, S. Gong, A. Wibowo, H. Gao, H. Ploehn, and H.-C. Zur Loye, "Polymer Composite and Nanocomposite Dielectric Materials for Pulse Power Energy Storage," *Materials*, vol. 2, no. 4, pp. 1697–1733, oct 2009. [Online]. Available: http://www.mdpi.com/1996-1944/2/4/1697

[91] X. Wang, T. Andritsch, G. Chen, and S. Virtanen, "The role of the filler surface chemistry on the dielectric and thermal properties of polypropylene aluminium nitride nanocomposites," *IEEE Transactions on Dielectrics and Electrical Insulation*, vol. 26, no. 3, pp. 1009–1017, jun 2019.

[92] S. Raetzke and J. Kindersberger, "Role of interphase on the resistance to high-voltage arcing, on tracking and erosion of silicone/SiO2 nanocomposites," *IEEE Transactions on Dielectrics and Electrical Insulation*, vol. 17, no. 2, pp. 607–614, apr 2010.

[93] C.-H. Lee and J.-J. Park, "The Partial Discharge Resistances of Epoxy-Nano-and-Micro Composites," *Transactions on Electrical and Electronic Materials*, vol. 11, no. 2, pp. 89–91, apr 2010.

[94] D. Fabiani, G. C. Montanari, A. Krivda, L. E. Schmidt, and R. Hollertz, "Epoxy based materials containing micro and nano sized fillers for improved electrical characteristics," in *Proceedings of the 2010 IEEE International Conference on Solid Dielectrics, ICSD 2010*, 2010.

[95] A. Ersoy and H. R. Hiziroglu, "Electrical breakdown of polyurethane-based nanocomposites," in *Proceedings of the 2010 IEEE International Conference on Solid Dielectrics, ICSD 2010*, 2010.

[96] V. Arrighi, I. J. McEwen, H. Qian, and M. B. Serrano Prieto, "The glass transition and interfacial layer in styrene-butadiene rubber containing silica nanofiller," *Polymer*, vol. 44, no. 20, pp. 6259–6266, sep 2003.

[97] V. M. Litvinov and H. W. Spiess, "2H NMR study of molecular motions in polydimethylsiloxane and its mixtures with aerosils," *Die Makromolekulare Chemie*, vol. 192, no. 12, pp. 3005–3019, dec 1991. [Online]. Available: http://doi.wiley.com/10.1002/macp.1991.021921216

[98] N. Mnif, V. Massardier, T. Kallel, and B. Elleuch, "New (PP/EPR)/nano-CaCO ₃ based formulations in the perspective of polymer recycling. Effect of nanoparticles properties and compatibilizers," *Polymers for Advanced Technologies*, vol. 21, no. 12, pp. 896–903, dec 2010. [Online]. Available: http://doi.wiley.com/10.1002/pat.1520

[99] F. W. Starr, T. B. Schrøder, and S. C. Glotzer, "Effects of a nanoscopic filler on the structure and dynamics of a simulated polymer melt and the relationship to ultrathin films," *Physical Review E - Statistical Physics, Plasmas, Fluids, and Related Interdisciplinary Topics*, vol. 64, no. 2, p. 5, jul 2001. [Online]. Available: https://journals.aps.org/pre/abstract/10.1103/PhysRevE.64.021802

[100] D. Pitsa, G. Vardakis, M. G. Danikas, and M. Kozako, "Electrical treeing propagation in nanocomposites and the role of nanofillers: Simulation with the aid of cellular automata," *Journal of Electrical Engineering*, vol. 61, no. 2, pp. 125–128, mar 2010. [Online]. Available: https://content.sciendo.com/view/journals/jee/61/2/article-p125.xml

[101] W. Pan and H. Zou, "Characterization of PAN/ATO nanocomposites prepared by solution blending," *Bulletin of Materials Science*, vol. 31, no. 5, pp. 807–811, oct 2008. [Online]. Available: https://link.springer.com/article/10.1007/s12034-008-0128-8

[102] A. Bansal, H. Yang, C. Li, K. Cho, B. C. Benicewicz, S. K. Kumar, and L. S. Schadler, "Quantitative equivalence between polymer nanocomposites and thin polymer films," *Nature Materials*, vol. 4, no. 9, pp. 693–698, aug 2005. [Online]. Available: www.nature.com/naturematerials

[103] D. Pitsa, M. G. Danikas, G. E. Vardakis, and T. Tanaka, "Influence of homocharges and nanoparticles in electrical tree propagation under DC voltage application," *Electrical Engineering*, vol. 94, no. 2, pp. 81–88, jun 2012. [Online]. Available: https://link.springer.com/article/10.1007/s00202-011-0222-6

[104] R. C. Smith, C. Liang, M. Landry, J. K. Nelson, and L. S. Schadler, "The mechanisms leading to the useful electrical properties of polymer nanodielectrics," *IEEE Transactions on Dielectrics and Electrical Insulation*, vol. 15, no. 1, pp. 187–196, feb 2008.

[105] Y. Okazaki, M. Kozako, M. Hikita, and T. Tanaka, "Effects of addition of nano-scale alumina and silica fillers on thermal conductivity and dielectric strength of epoxy / alumina microcomposites," in *Proceedings of the 2010 IEEE International Conference on Solid Dielectrics, ICSD 2010*, 2010.

[106] T. Iizuka and T. Tanaka, "Effects of nano silica filler size on treeing breakdown lifetime of epoxy nanocomposites," in *Proceedings of the IEEE International Conference on Properties and Applications of Dielectric Materials*, 2009, pp. 733–736.

[107] A. Hajiyiannis, G. Chen, C. Zhang, and G. Stevens, "Space charge formation in epoxy resin including various nanofillers," in *Annual Report - Conference on Electrical Insulation and Dielectric Phenomena, CEIDP*, 2008, pp. 714–717.

[108] C. Zou, M. Fu, J. C. Fothergill, and S. W. Rowe, "The influence of water on dielectric behavior of silica-filled epoxy nano-composites and percolation phenomenon," in *Annual Report - Conference on Electrical Insulation and Dielectric Phenomena, CEIDP*, 2007, pp. 372–375.

[109] C. Zou, J. C. Fothergill, and S. W. Rowe, "A "water shell" model for the dielectric properties of hydrated silica-filled epoxy nano-composites," in *2007 International Conference on Solid Dielectrics, ICSD*, 2007, pp. 389–392.

[110] J. C. Fothergill, "Electrical properties," in *Dielectric Polymer Nanocomposites*. Springer US, 2010, pp. 197–228. [Online]. Available: https://link.springer.com/chapter/10.1007/978-1-4419-1591-7{_}7

[111] T. Tanaka, "Interface properties and surface erosion resistance," in *Dielectric Polymer Nanocomposites*. Springer US, 2010, pp. 229–258.

[112] J. K. Nelson, *Dielectric polymer nanocomposites*. Springer US, 2010.

[113] M. G. Danikas, A. Bairaktari, R. Sarathi, A. B. Bin, and A. Ghani, "A Review of Two Nanocomposite Insulating Materials Models: Lewis' Contribution in the Development of the Models, their Differences, their Similarities and Future Challenges," Tech. Rep. 3, jun 2014. [Online]. Available: www.etasr.com

[114] M. A. Martínez-Fuentes and J. J. E. Herrera-Velázquez, "On the accuracy of the Debye shielding," feb 2012. [Online]. Available: http://arxiv.org/abs/1202.2399

[115] T. Andritsch, R. Kochetov, P. H. Morshuis, and J. J. Smit, "Proposal of the polymer chain alignment model," in *Annual Report - Conference on Electrical Insulation and Dielectric Phenomena, CEIDP*, 2011, pp. 624–627.

[116] D. Xie, D. Min, Y. Huang, S. Li, M. T. Nazir, and B. T. Phung, "Classified effects of nanofillers on DC breakdown and partial discharge resistance of polypropylene/alumina nanocomposites," *IEEE Transactions on Dielectrics and Electrical Insulation*, vol. 26, no. 3, pp. 698–705, jun 2019.

[117] T. J. Lewis, "Interfaces are the dominant feature of dielectrics at the nanometric level," in *IEEE Transactions on Dielectrics and Electrical Insulation*, vol. 11, no. 5, oct 2004, pp. 739–753.

[118] ——, "Interfaces and nanodielectrics are synonymous," in *Proceedings of the 2004 IEEE International Conference on Solid Dielectrics ICSD 2004*, vol. 2, 2004, pp. 792–795.

[119] R. W. Siegel, "What do we really know about the atomic-scale structures of nanophase materials?" *Journal of Physics and Chemistry of Solids*, vol. 55, no. 10, pp. 1097–1106, oct 1994.

[120] A. K. Ghosh, T. Feng, J. I. Haberman, and H. P. Maruska, "Effects of interfacial charge on the electron affinity, work function, and electrical characteristics

of thinly oxidized semiconductor-insulator- semiconductor and metal-insulator-semiconductor devices," *Journal of Applied Physics*, vol. 55, no. 8, pp. 2990–2994, apr 1984. [Online]. Available: http://aip.scitation.org/doi/10.1063/1.333343

[121] A. Muththalib and B. A. Baudet, "Effect of heavy metal contamination on the plasticity of kaolin-bentonite clay mixtures and an illite-smectite rich natural clay," in *E3S Web of Conferences*, vol. 92. EDP Sciences, jun 2019, p. 10005. [Online]. Available: https://ui.adsabs.harvard.edu/abs/2019E3SWC..9210005M/abstract

[122] T. J. Lewis, "A model for nano-composite polymer dielectrics under electrical stress," in *2007 International Conference on Solid Dielectrics, ICSD*, 2007, pp. 11–14.

[123] J. K. Nelson, L. A. Utracki, R. K. MacCrone, and C. W. Reed, "Role of the Interface in determining the dielectric properties of nanocomposites," in *Annual Report - Conference on Electrical Insulation and Dielectric Phenomena, CEIDP*, 2004, pp. 314–317.

[124] S. Raetzke and J. Kindersberger, "The Effect of Interphase Structures in Nanodielectrics," *IEEJ Transactions on Fundamentals and Materials*, vol. 126, no. 11, pp. 1044–1049, 2006. [Online]. Available: http://joi.jlc.jst.go.jp/JST.JSTAGE/ieejfms/126.1044?from=CrossRef

[125] F. Ciuprina, I. Plesa, P. V. Notingher, T. Tudorache, and D. Panaitescu, "Dielectric properties of nanodielectrics with inorganic fillers," in *Annual Report - Conference on Electrical Insulation and Dielectric Phenomena, CEIDP*, 2008, pp. 682–685.

[126] S. Li, G. Yin, G. Chen, J. Li, S. Bai, L. Zhong, Y. Zhang, and Q. Lei, "Short-term breakdown and long-term failure in nanodielectrics: A review," *IEEE Transactions on Dielectrics and Electrical Insulation*, vol. 17, no. 5, pp. 1523–1535, oct 2010.

[127] S. W. Rowe, "Electrical ageing of composites: An industrial perspective," in *2007 International Conference on Solid Dielectrics, ICSD*, 2007, pp. 401–406.

[128] D. Fabiani, G. C. Montanari, and L. Testa, "Effect of aspect ratio and water contamination on the electric properties of nanostructured insulating materials," *IEEE Transactions on Dielectrics and Electrical Insulation*, vol. 17, no. 1, pp. 221–230, feb 2010.

[129] P. A. Sharad and K. S. Kumar, "Application of Surface Modified XLPE Nanocomposites for Electrical Insulation of High Voltage Cables- Partial Discharge Study," in *Energy Procedia*, vol. 117. Elsevier Ltd, jun 2017, pp. 260–267.

[130] S. H. Yoo, L. Liu, and S. Park, "Nanoparticle films as a conducting layer for anodic aluminum oxide template-assisted nanorod synthesis," *Journal of Colloid and Interface Science*, vol. 339, no. 1, pp. 183–186, nov 2009.

[131] K. Kukli, M. Ritala, M. Leskelä, T. Sajavaara, J. Keinonen, D. C. Gilmer, R. Hegde, R. Rai, and L. Prabhu, "Atomic layer deposition of HfO2 thin films and nanolayered HfO2-Al2O3-Nb2O5 dielectrics," *Journal of Materials Science: Materials in Electronics*,

vol. 14, no. 5-7, pp. 361–367, may 2003. [Online]. Available: https://link.springer.com/article/10.1023/A:1023948617372

[132] Y. Y. Wang, K. F. Cai, and X. Yao, "Facile synthesis of PbTe nanoparticles and thin films in alkaline aqueous solution at room temperature," *Journal of Solid State Chemistry*, vol. 182, no. 12, pp. 3383–3386, dec 2009.

[133] H. I. Schlesinger, H. C. Brown, B. Abraham, A. C. Bond, N. Davidson, A. E. Finholt, J. R. Gilbreath, H. Hoekstra, L. Horvitz, E. K. Hyde, J. J. Katz, J. Knight, R. A. Lad, D. L. Mayfield, L. Rapp, D. M. Ritter, A. M. Schwartz, I. Sheft, L. D. Tuck, and A. O. Walker, "New Developments in the Chemistry of Diborane and the Borohydrides. I. General Summary," *Journal of the American Chemical Society*, vol. 75, no. 1, pp. 186–190, jan 1953. [Online]. Available: https://pubs.acs.org/sharingguidelines

[134] X. Q. Li and W. X. Zhang, "Iron nanoparticles: The core-shell structure and unique properties for Ni(II) sequestration," *Langmuir*, vol. 22, no. 10, pp. 4638–4642, may 2006. [Online]. Available: http://www.sigmaaldrich.com/.

[135] J. P. Chen and L. L. Lim, "Key factors in chemical reduction by hydrazine for recovery of precious metals," *Chemosphere*, vol. 49, no. 4, pp. 363–370, oct 2002.

[136] L. Zhou, H. Zhang, H. Sun, S. Liu, M. O. Tade, S. Wang, and W. Jin, "Recent advances in non-metal modification of graphitic carbon nitride for photocatalysis: A historic review," pp. 7002–7023, sep 2016. [Online]. Available: www.rsc.org/catalysiswww.rsc.org/catalysis

[137] T. D. Ewers, A. K. Sra, B. C. Norris, R. E. Cable, C. H. Cheng, D. F. Shantz, and R. E. Schaak, "Spontaneous hierarchical assembly of rhodium nanoparticles into spherical aggregates and superlattices," *Chemistry of Materials*, vol. 17, no. 3, pp. 514–520, feb 2005. [Online]. Available: https://pubs.acs.org/sharingguidelines

[138] W. Stöber, A. Fink, and E. Bohn, "Controlled growth of monodisperse silica spheres in the micron size range," *Journal of Colloid And Interface Science*, vol. 26, no. 1, pp. 62–69, jan 1968.

[139] "CRC Handbook of Chemistry and Physics, 86th Edition Edited by David R. Lide (National Institute of Standards and Technology). CRC Press (an imprint of Taylor and Francis Group): Boca Raton, FL. 2005. 2544 pp. $125.96. ISBN 0-8493-0486-5." *Journal of the American Chemical Society*, vol. 128, no. 16, pp. 5585–5585, apr 2006. [Online]. Available: https://pubs.acs.org/sharingguidelines

[140] J. Hulliger, "The Science of Crystallization. Microscopic Interfacial Phenomena. Von W. A. Tiller. Cambridge University Press, Cambridge (England), 1991," *Angewandte Chemie*, vol. 104, no. 7, pp. 951–951, jul 1992. [Online]. Available: http://doi.wiley.com/10.1002/ange.19921040757

[141] A. K. C. C. N. R. Rao, A. Muller, "The chemistry of nanomaterials - C. N. R. Rao, A. Muller, A. K. Cheetham (eds), WILEY-VCH Verlag GmbH & Co.

KGaA, Weinheim 2004. ISBN 3-527-30686-2, 741 pages," *Colloid and Polymer Science*, vol. 283, no. 2, pp. 234–234, dec 2004. [Online]. Available: https://link.springer.com/article/10.1007/s00396-004-1140-1

[142] Z. P. Qiao, G. Xie, J. M. Huang, S. Y. Zhao, and X. M. Chen, "One-pot monomer self-assembly route to PbS/poly(methyl methacrylate) core/shell nanocomposite thin coatings," *Journal of Materials Chemistry*, vol. 12, no. 3, pp. 611–613, feb 2002. [Online]. Available: https://pubs.rsc.org/en/content/articlehtml/2002/jm/b105005mhttps://pubs.rsc.org/en/content/articlelanding/2002/jm/b105005m

[143] S. Kirsch, A. Doerk, E. Bartsch, H. Sillescu, K. Landfester, H. W. Spiess, and W. Maechtle, "Synthesis and characterization of highly cross-linked, monodisperse core-shell and inverted core-shell colloidal particles. Polystyrene/ poly(tert-butyl acrylate) core-shell and inverse core-shell particles," *Macromolecules*, vol. 32, no. 14, pp. 4508–4518, jul 1999. [Online]. Available: https://pubs.acs.org/sharingguidelines

[144] V. S. Amar, X. M. Pasala, J. A. Puszynski, and R. V. Shende, "Sonication Derived Powdered Mixtures of Ferrite and Ceramic Nanoparticles for H₂Generation," *American Journal of Energy Research, Vol. 3, 2015, Pages 25-31*, vol. 3, no. 2, pp. 25–31, 2015. [Online]. Available: http://pubs.sciepub.com/ajer/3/2/2/index.html

[145] J. J. L. Velázquez, "On the effect of stochastic fluctuations in the dynamics of the Lifshitz-Slyozov-Wagner model," *Journal of Statistical Physics*, vol. 99, no. 1-2, pp. 57–113, 2000. [Online]. Available: https://link.springer.com/article/10.1023/A:1018640505926

[146] Z. Hu, D. J. Escamilla Ramírez, B. E. Heredia Cervera, G. Oskam, and P. C. Searson, "Synthesis of ZnO nanoparticles in 2-propanol by reaction with water," *Journal of Physical Chemistry B*, vol. 109, no. 22, pp. 11 209–11 214, jun 2005. [Online]. Available: https://pubs.acs.org/sharingguidelines

[147] K. Sabyrov, N. D. Burrows, and R. L. Penn, "Size-dependent anatase to rutile phase transformation and particle growth," *Chemistry of Materials*, vol. 25, no. 8, pp. 1408–1415, apr 2013. [Online]. Available: https://pubs.acs.org/sharingguidelines

[148] J. Xu, F. Zeng, S. Wu, X. Liu, C. Hou, and Z. Tong, "Gold nanoparticles bound on microgel particles and their application as an enzyme support," *Nanotechnology*, vol. 18, no. 26, p. 265704, jul 2007.

[149] L. Wang, J. Luo, Q. Fan, M. Suzuki, I. S. Suzuki, M. H. Engelhard, Y. Lin, N. Kim, J. Q. Wang, and C. J. Zhong, "Monodispersed core-shell Fe 3O 4@Au nanoparticles," *Journal of Physical Chemistry B*, vol. 109, no. 46, pp. 21 593–21 601, nov 2005. [Online]. Available: https://pubs.acs.org/sharingguidelines

[150] J. Sun, K. Xu, C. Shi, J. Ma, W. Li, and X. Shen, "Influence of core/shell TiO2@SiO2 nanoparticles on cement hydration," *Construction and Building Materials*, vol. 156, pp. 114–122, dec 2017.

[151] C. Takai-Yamashita, H. Imabeppu, and M. Fuji, "Synthesis of hollow silica nanoparticles using poly (acrylic acid)-3,3'-diaminodipropylamine template," *Colloids and Surfaces A: Physicochemical and Engineering Aspects*, vol. 483, pp. 81–86, oct 2015.

[152] Y. Wan and S. H. Yu, "Polyelectrolyte controlled large-scale synthesis of hollow silica spheres with tunable sizes and wall thicknesses," *Journal of Physical Chemistry C*, vol. 112, no. 10, pp. 3641–3647, mar 2008. [Online]. Available: https://pubs.acs.org/sharingguidelines

[153] S. Chaudhary, T. Andritsch, and A. Vaughan, "Effect of core-shell particles on the dielectric properties of epoxy nanocomposites," in *Annual Report - Conference on Electrical Insulation and Dielectric Phenomena, CEIDP*, vol. 2019-Octob, 2019.

[154] S. Chaudhary, O. Vryonis, A. S. Vaughan, and T. Andritsch, "Dielectric Response in Epoxy Nanocomposites Incorporating Various Nano-silica Architectures," in *2021 IEEE Conference on Electrical Insulation and Dielectric Phenomena (CEIDP)*. IEEE, dec 2021, pp. 57–60.

[155] O. Vryonis, S. Riarh, T. Andritsch, and A. S. Vaughan, "Stoichiometry and molecular dynamics of anhydride-cured epoxy resin incorporating octa-glycidyl POSS Co-Monomer," *Polymer*, vol. 213, p. 123312, jan 2021.

[156] M. Koopman, G. Gouadec, K. Carlisle, K. K. Chawla, and G. Gladysz, "Compression testing of hollow microspheres (microballoons) to obtain mechanical properties," *Scripta Materialia*, vol. 50, no. 5, pp. 593–596, mar 2004.

[157] F. N. Buyuknalcaci, Y. Polat, T. A. Negawo, E. Döner, M. S. Alam, T. Hamouda, and A. Kilic, "24 - Carbon nanotube-based nanocomposites for wind turbine applications," in *Polymer-based Nanocomposites for Energy and Environmental Applications*, M. Jawaid and M. M. Khan, Eds. Woodhead Publishing, 2018, pp. 635–661.

[158] E. Wiberg, N. Wiberg, and A. F. Holleman, *Inorganic chemistry*. San Diego; Berlin; New York: Academic Press ; De Gruyter, 2001.

[159] A. Kirfel, H.-G. Krane, P. Blaha, K. Schwarz, and T. Lippmann, "Electron-density distribution in stishovite, SiO2: a new high-energy synchrotron-radiation study," *Acta Crystallographica Section A*, vol. 57, no. 6, pp. 663–677, 2001.

[160] Y. Ding, X. Chu, X. Hong, P. Zou, and Y. Liu, "The infrared fingerprint signals of silica nanoparticles and its application in immunoassay," *Applied Physics Letters*, vol. 100, no. 1, p. 13701, 2012.

[161] Munasir, Z. A. Imam Supardi, Mashadi, Z. Nisa, D. H. Kusumawati, N. P. Putri, A. Taufiq, Sunaryono, N. Hidayat, and Darminto, "Phase Transition of SiO2 Nanoparticles Prepared from Natural Sand: The Calcination Temperature Effect," *Journal of Physics: Conference Series*, vol. 1093, p. 12025, 2018. [Online]. Available: http://dx.doi.org/10.1088/1742-6596/1093/1/012025

[162] A. Rudin and P. Choi, "Chapter 4 - Mechanical Properties of Polymer Solids and Liquids," in *The Elements of Polymer Science & Engineering (Third Edition)*, A. Rudin and P. Choi, Eds. Boston: Academic Press, 2013, pp. 149–229.

[163] G. V. Gibbs, F. C. Hill, M. B. Boisen, and R. T. Downs, "Power law relationships between bond length, bond strength and electron density distributions," *Physics and Chemistry of Minerals*, vol. 25, no. 8, pp. 585–590, 1998.

[164] J. W. Linnett and B. G. Reuben, "Changes in molecular dipole moments on distortion," *Transactions of the Faraday Society*, vol. 55, no. 0, pp. 510–514, 1959.

[165] L. D. Marco, M. Thämer, M. Reppert, and A. Tokmakoff, "Direct observation of intermolecular interactions mediated by hydrogen bonding," *The Journal of Chemical Physics*, vol. 141, no. 3, p. 34502, 2014.

[166] T. Fornaro, D. Burini, M. Biczysko, and V. Barone, "Hydrogen-Bonding Effects on Infrared Spectra from Anharmonic Computations: Uracil–Water Complexes and Uracil Dimers," *The Journal of Physical Chemistry A*, vol. 119, no. 18, pp. 4224–4236, 2015.

[167] W. A. Pliskin, "Comparison of properties of dielectric films deposited by various methods," *Journal of Vacuum Science and Technology*, vol. 14, no. 5, pp. 1064–1081, 1977.

[168] S. Ponton, F. Dhainaut, H. Vergnes, D. Samelor, D. Sadowski, V. Rouessac, H. Lecoq, T. Sauvage, B. Caussat, and C. Vahlas, "Investigation of the densification mechanisms and corrosion resistance of amorphous silica films," *Journal of Non-Crystalline Solids*, vol. 515, pp. 34–41, 2019.

[169] H. Hattori, P. Arudra, A. Abdalla, A. M. Aitani, and S. S. Al-Khattaf, "Infrared Study of Silanol Groups on Dealuminated High Silica MFI Zeolite to Correlate Different Types of Silanol Groups with Activity for Conversion of 1-Butene to Propene," *Catalysis Letters*, vol. 150, no. 3, pp. 771–780, 2020.

[170] S. Wilhelm and M. Kind, "Influence of pH, Temperature and Sample Size on Natural and Enforced Syneresis of Precipitated Silica," *Polymers*, vol. 7, no. 12, pp. 2504–2521, 2015.

[171] D. M. Mackie, J. P. Jahnke, M. S. Benyamin, and J. J. Sumner, "Simple, fast, and accurate methodology for quantitative analysis using Fourier transform infrared spectroscopy, with bio-hybrid fuel cell examples," *MethodsX*, vol. 3, pp. 128–138, 2016.

[172] L. Spallino, L. Vaccaro, L. Sciortino, S. Agnello, G. Buscarino, M. Cannas, and F. M. Gelardi, "Visible-ultraviolet vibronic emission of silica nanoparticles," *Physical Chemistry Chemical Physics*, vol. 16, no. 40, pp. 22 028–22 034, 2014.

[173] S. Cholake, M. Mada, R. Singh, Y. Bai, X.-L. Zhao, S. Rizkalla, and S. Bandyopadhyay, "Quantitative Analysis of Curing Mechanisms of Epoxy Resin by Mid- and Near- Fourier Transform Infra Red Spectroscopy," *Defence science journal*, vol. 64, 2014.

[174] M. C. Finzel, J. Delong, and M. C. Hawley, "Effect of stoichiometry and diffusion on an epoxy/amine reaction mechanism," *Journal of Polymer Science Part A: Polymer Chemistry*, vol. 33, no. 4, pp. 673–689, 1995.

[175] M. Gonzalez, J. Cabanelas, and J. Baselga, "Applications of FTIR on Epoxy Resins - Identification, Monitoring the Curing Process, Phase Separation and Water Uptake," 2012.

[176] I. A. Saeedi, T. Andritsch, and A. S. Vaughan, "On the Dielectric Behavior of Amine and Anhydride Cured Epoxy Resins Modified Using Multi-Terminal Epoxy Functional Network Modifier," *Polymers*, vol. 11, no. 8, p. 1271, 2019.

[177] L. Dalstein, E. Potapova, and E. Tyrode, "The elusive silica/water interface: isolated silanols under water as revealed by vibrational sum frequency spectroscopy," *Physical Chemistry Chemical Physics*, vol. 19, no. 16, pp. 10 343–10 349, 2017.

[178] J. P. Bell, "Structure of a typical amine-cured epoxy resin," *Journal of Polymer Science Part A-2: Polymer Physics*, vol. 8, no. 3, pp. 417–436, mar 1970.

[179] O. Vryonis, S. T. H. Virtanen, T. Andritsch, A. S. Vaughan, and P. L. Lewin, "Understanding the cross-linking reactions in highly oxidized graphene/epoxy nanocomposite systems," *Journal of Materials Science*, vol. 54, no. 4, pp. 3035–3051, 2019.

[180] G. A. Pogany, "The α relaxation in epoxy resins," *European Polymer Journal*, vol. 6, no. 2, pp. 343–353, feb 1970.

[181] I. A. Saeedi, A. S. Vaughan, T. Andritsch, and S. Virtanen, "The effect of curing conditions on the electrical properties of an epoxy resin," in *2016 IEEE Conference on Electrical Insulation and Dielectric Phenomena (CEIDP)*. IEEE, oct 2016, pp. 461–464.

[182] T. D. Chang, S. H. Carr, and J. O. Brittain, "Studies of epoxy resin systems: Part B: Effect of crosslinking on the physical properties of an epoxy resin," *Polymer Engineering & Science*, vol. 22, no. 18, pp. 1213–1220, 1982.

[183] B. Arab, A. Shokuhfar, and S. Ebrahimi-Nejad, "Glass transition temperature of cross-linked epoxy polymers: a molecular dynamics study," in *Proceedings of the International Conference Nanomaterials: Applications and Properties*, no. 1, no. 1. Sumy State University Publishing, 2012, pp. 01NDLCN11–01NDLCN11.

[184] T. Hirai and D. E. Kline, "Effects of heat treatment on dynamic mechanical properties of nonstoichiometric, amine-cured epoxy resins," *Journal of Applied Polymer Science*, vol. 17, no. 1, pp. 31–44, 1973.

[185] G. A. Kontos, A. L. Soulintzis, P. K. Karahaliou, G. C. Psarras, S. N. Georga, C. A. Krontiras, and M. N. Pisanias, "Electrical relaxation dynamics in TiO2-polymer matrix composites," *Express Polym Lett*, vol. 1, no. 12, pp. 781–789, 2007.

[186] M. Beiner and K. L. Ngai, "Interrelation between Primary and Secondary Relaxations in Polymerizing Systems Based on Epoxy Resins," *Macromolecules*, vol. 38, no. 16, pp. 7033–7042, 2005.

[187] J. Mijović and H. Zhang, "Local Dynamics and Molecular Origin of Polymer NetworkWater Interactions as Studied by Broadband Dielectric Relaxation Spectroscopy, FTIR, and Molecular Simulations," *Macromolecules*, vol. 36, no. 4, pp. 1279–1288, 2003.

[188] D. H. Kaelble, "Dynamic and tensile properties of epoxy resins," *Journal of Applied Polymer Science*, vol. 9, no. 4, pp. 1213–1225, 1965.

[189] C. A. May and F. E. Weir, "Dynamic mechanical properties of epoxy resins," *Polymer Engineering & Science*, vol. 2, no. 3, pp. 207–212, 1962.

[190] T. D. Chang, S. H. Carr, and J. O. Brittain, "Studies of epoxy resin systems: Part A: A study of the origins of the secondary relaxations of epoxy resins by thermally stimulated depolarization," *Polymer Engineering & Science*, vol. 22, no. 18, pp. 1205–1212, 1982.

[191] T. Takahama and P. H. Geil, "BETA RELAXATION BEHAVIOR OF BISPHENOL-TYPE RESINS," *J POLYM SCI POLYM PHYS ED*, vol. V 20, no. N 11, pp. 1979–1986, 1982.

[192] J. D. Keenan, J. C. Seferis, and J. T. Quinlivan, "Effects of moisture and stoichiometry on the dynamic mechanical properties of a high-performance structural epoxy," *Journal of Applied Polymer Science*, vol. 24, no. 12, pp. 2375–2387, dec 1979.

[193] A. Soulintzis, G. Kontos, P. Karahaliou, G. C. Psarras, S. N. Georga, and C. A. Krontiras, "Dielectric relaxation processes in epoxy resin-ZnO composites," *Journal of Polymer Science Part B: Polymer Physics*, vol. 47, no. 4, pp. 445–454, feb 2009.

[194] S. Pangrle, C. S. Wu, and P. H. Geil, "Low temperature relaxation of DGEBA epoxy resins: A thermally stimulated discharge current (TSDC) study," *Polymer Composites*, vol. 10, no. 3, pp. 173–183, 1989.

[195] I. A. Saeedi, A. S. Vaughan, and T. Andritsch, "Change in the electrical properties due to modification of the epoxy network structure using reactive diluents," in *2016 IEEE Conference on Electrical Insulation and Dielectric Phenomena (CEIDP)*, 2016, pp. 663–666.

[196] C. Liu, K. Shih, Y. Gao, F. Li, and L. Wei, "Dechlorinating transformation of propachlor through nucleophilic substitution by dithionite on the surface of alumina," *Journal of Soils and Sediments*, vol. 12, no. 5, pp. 724–733, 2012.

[197] T. Dhandayuthapani, R. Sivakumar, and R. Ilangovan, "Growth of micro flower rutile TiO2 films by chemical bath deposition technique: Study on the properties of structural, surface morphological, vibrational, optical and compositional," *Surfaces and Interfaces*, vol. 4, pp. 59–68, oct 2016.

[198] S. Nakamura, Y. Tsuji, and K. Yoshizawa, "Role of Hydrogen-Bonding and OHπ Interactions in the Adhesion of Epoxy Resin on Hydrophilic Surfaces," 2020.

[199] M. A. Bashir, "Use of Dynamic Mechanical Analysis (DMA) for Characterizing Interfacial Interactions in Filled Polymers," *Solids 2021, Vol. 2, Pages 108-120*, vol. 2, no. 1, pp. 108–120, mar 2021. [Online]. Available: https://www.mdpi.com/2673-6497/2/1/6/htmhttps://www.mdpi.com/2673-6497/2/1/6

[200] I. M. Kalogeras, "Glass-Transition Phenomena in Polymer Blends," *Encyclopedia of Polymer Blends*, pp. 1–134, jun 2016.

[201] C. Lin, T. Lü, D. Qi, Z. Cao, Y. Sun, and Y. Wang, "Effects of Surface Groups on SiO2 Nanoparticles on in Situ Solution Polymerization: Kinetics and Mechanism," *Industrial and Engineering Chemistry Research*, vol. 57, no. 45, pp. 15 280–15 290, nov 2018. [Online]. Available: https://pubs.acs.org/doi/full/10.1021/acs.iecr.8b03149

[202] J. Czogała, E. Pankalla, and R. Turczyn, "Recent Attempts in the Design of Efficient PVC Plasticizers with Reduced Migration," *Materials*, vol. 14, no. 4, pp. 1–28, feb 2021. [Online]. Available: /pmc/articles/PMC7916570//pmc/articles/PMC7916570/?report=abstracthttps://www.ncbi.nlm.nih.gov/pmc/articles/PMC7916570/

[203] G. Tsagaropoulos and A. Eisenberg, "Dynamic Mechanical Study of the Factors Affecting the Two Glass Transition Behavior of Filled Polymers. Similarities and Differences with Random Ionomers," *Macromolecules*, vol. 28, no. 18, pp. 6067–6077, aug 1995.

[204] H. Xia, M. Song, Z. Zhang, and M. Richardson, "Microphase separation, stress relaxation, and creep behavior of polyurethane nanocomposites," *Journal of Applied Polymer Science*, vol. 103, no. 5, pp. 2992–3002, mar 2007. [Online]. Available: https://onlinelibrary.wiley.com/doi/full/10.1002/app.25462https://onlinelibrary.wiley.com/doi/abs/10.1002/app.25462https://onlinelibrary.wiley.com/doi/10.1002/app.25462

[205] M. H. Mat Yazik, M. T. H. Sultan, M. Jawaid, A. R. Abu Talib, N. Mazlan, A. U. Md Shah, and S. N. A. Safri, "Effect of Nanofiller Content on Dynamic Mechanical and Thermal Properties of Multi-Walled Carbon Nanotube and Montmorillonite Nanoclay Filler Hybrid Shape Memory Epoxy Composites," *Polymers*, vol. 13, no. 5, pp. 1–21, mar 2021. [Online]. Available: /pmc/articles/PMC7956654//pmc/articles/PMC7956654/?report=abstracthttps://www.ncbi.nlm.nih.gov/pmc/articles/PMC7956654/